Author:
Dong, Jun

Title:
Microfluidic Emulsification and Force Transmissions in Colloidal Systems

Microfluidic Emulsification and Force Transmissions in Colloidal Systems

Jun Dong

HH Wills Physics Laboratory
University of Bristol

A dissertation submitted to the University of Bristol in accordance with the requirements of the degree of DOCTOR OF PHILOSOPHY in the Faculty of Physics.

Word count: 42286

July 2020

Declaration

I declare that the work in this dissertation was carried out in accordance with the requirements of the University's Regulations and Code of Practice for Research Degree Programmes and that it has not been submitted for any other academic award. Except where indicated by specific reference in the text, the work is the candidate's own work. Work done in collaboration with, or with the assistance of others is indicated as such. Any views expressed in the dissertation are those of the author.

SIGNED: .....

Jun Dong

DATE: .....

Publications

J. Dong, M. Meissner, M. A. Faers, J. Eggers, A. M. Seddon and C. P. Royall. Opposed Flow Focusing: Evidence of A Second Order Jetting Transition. *Soft Matter*. 14, 8344 (2018)

M. Meissner, J. Dong, J. Eggers, A. M. Seddon and C. P. Royall. Oil-in-Water Microfluidics on The Colloidal Scale: New Routes to Self-Assembly and Glassy Packings. *Soft Matter*. 13, 788 (2017)

Acknowledgements

At first, I want to acknowledge Bayer AG and ERC for funding my PhD.

I would also like to acknowledge my supervisors Prof. Paddy Royall and Dr. Malcolm Faers for their absolute support and dedicated mentoring throughout my PhD.

There is no doubt about the importance of the generous help from all Royall group members not only on research but also on my life. It is my greatest pleasure to be part of this fantastic team. Especially I want to express my appreciation to Francesco, he has provided endless help with the data analysis and helped me understand the experimental data. I want to thank for James for unconditional support in the lab, giving useful suggestions when the experiment is not working. Thank Rattachai for his exceptional patience and repeatedly answear all my silly questions and also give suggestions when experiment is not going well. My deep apperciation to Yushi, who explained me the fascination about different particle tracking methods, kindly helped me improve my tracking results and share knowledge about his lovely fish. I'm very grateful for Max who introduced me into the world of microfluidics and we work together trying to produce small droplets. Last but not least, thanks to Ioatzin who has helped a lot with my experiments and being super kind all the time.

Most importantly, I could not overcome many hardtimes without the unreserved support from my beloved parents and my significant half Juntai.

Abstract

Like other properties of materials, the mechanical properties ultimately derive from the local structure assumed by the constituent particles. The force chains are the microscopic analogue of bulk mechanical properties, but have only been accessed in athermal granular materials. By combining super-resolution imaging with colloidal droplets which are labelled with a solvatochromic dye, we quantitatively obtain the force distribution within the colloidal system and explore the relationship between local structure and mechanical properties in colloidal gels and glasses.

In this thesis, first we demonstrate methods of producing monodisperse oil-in-water colloidal droplets by using microfluidic devices. One approach is to reduce the dimension of channels to a value that is comparable to the desired droplet size, and combining with Norland Optical Adhesive (NOA) as the device material which can provide stable hydrophilic surfaces for generating oil-in-water emulsions. Alternatively, we use a PDMS device with a novel opposed-flow geometry, where we observe a second order jetting transition, jet radius following power-law scaling. By tuning applied pressures continuously, we can produce droplets down to sub-micron.

With monodisperse colloidal droplets, colloidal gels are prepared by adding non-absorbing polymers. Structures of gels vary slightly upon deeper quench, with a decrease of both number of neighbours and contacts. The probability distributions of contact force decay following a Gaussian distribution at large forces. The average force $\langle f \rangle$ of the colloidal gels is approximately 5 nN. No percolated force chains are detected in the elastic gels, but only some short chains.We detect higher population of local structures in particles forming force chains than that of the bulk emulsions, implying local structure is crucial for force chain formation. In the creaming experiment of a colloidal gel, after about $320\tau_B$ droplets cream to the top of the sample cell under gravity. Surprisingly during this process there is no significant change in structural properties. The peak in the distribution of contact forces becomes less pronounced, this possibly indicates that the gel becomes more liquid-like as the waiting time increases.

We investigate three dense emulsions with ϕ up to 0.60, aiming to identify force-bearing neighbours and force networks in colloidal glasses. However due to low polydispersity, small regions of crystals are found in all dense emulsions. We notice at low ϕ about 0.54, the shape of force distribution is also Gaussian-like, however as the ϕ increases, it becomes close to exponential which is similar to experimental measurements of contact forces in jammed granular matter. Again no percolated force chains were found, indicating the emulsions are mechanically unstable, which is contrary to the fact of high contact number $Z = 9$. Unfortunately, we do have enough purely glassy states spreading the range between ϕ_g and ϕ_J, leaving the question of the existence of Gardner transition remains unclear.

Table of contents

List of figures

List of tables

Structure of the Thesis

Chapter 1 introduces the background of colloids, which is the basis for the formation and understanding of the research objects in the thesis. The introduction of microfluidics and review on small droplet generation are also presented as background for Chapter 3 and 4.

Chapter 2 describes emulsion synthesis procedure that is used for preparing colloidal gels and glasses in Chapter 5 - 7, the imaging technique of confocal microscopy and solvatochromic fluorescent dye that are employed to identify droplet contacts whose sizes are proportional to interdroplet forces. The method of particle and contact tracking, interdroplet force and particle stress calculations, and the determination of force chains are also explained in this chapter.

Chapter 3 and 4 present the design, experimental setups, and results of microfluidic emulsifications. In Chapter 3, Norland Optical Adhesive (NOA) is applied as the device material, which is more hydrophilic than conventional polydimethylsiloxane (PDMS). We show the success of producing silicone oil droplets at colloidal scale, and we also measure the scaling of droplet size with viscosity and flow rate ratios. In Chapter 4, we discover an opposed flow geometry in which the jetting transition is found to be second-order like.Using this geometry, sub-micron droplets are produced in a 50μm PDMS device channel in flow focusing regime.

In Chapter 5, we investigate contact forces in three emulsion gel samples with various non-absorbing polymer concentrations, the gel with intermediate polymer concentration is observed under gravity to study contact forces during creaming in Chapter 6. The probability distribution of contact force decays following a Gaussian distribution, it does not change significantly for different attraction strengths. The stress and local pressure are also computed for each sample and time frame. We do not find percolated force chains in any of the gel network, also during the creaming process.

The same force study method is applied in three dense emulsions with volume fractions of 0.54, 0.55 and 0.60 in Chapter 7, with the aim of exploring whether there is the Gardner transition between a glassy and jammed state. However, the force distribution in our dense emulsions is not close to the prediction of a power law scaling when approaching jamming as described in the theoretical work[7].

Chapter 8 summarises the results from Chapter 3 to 7, we also rise up some discussions on the method and findings of force measurements, and propose possible work for further research.

Chapter 1

Introduction

1.1 Colloids

Colloids are particles which can be solid, liquid or gaseous, having sizes in the range of 10 nm to 10 μm. Depending on the state of matter in the system, colloids can be divided into a number of categories. Colloidal dispersions are considered as solid colloidal particles dispersed in a liquid solvent; emulsions are liquid colloidal droplets in another immiscible liquid; and foams are gas bubbles in a liquid or solid medium[8].

One typical characteristic of colloidal particles is that when dispersed in a liquid, their motion is diffusive and Brownian, which is a random and stochastic process[9]. The Brownian time tells the timescale of particle diffusion, which is defined as the time for a colloidal particle diffusing a radius of the particle:

$$\tau_B = \frac{a^2}{6D} = \frac{\sigma^3 \pi \eta}{8 k_B T} \tag{1.1}$$

where a and σ are radius and diameter of the particle respectively, η is the solvent viscosity, k_B is the Boltzmann constant, T is the temperature and D is the diffusion coefficient of the colloid which is defined as:

$$D = \frac{k_B T}{6\pi\eta a_H} = \frac{k_B T}{3\pi\eta\sigma_H} \tag{1.2}$$

where a_H and σ are the hydrodynamic radius/diameter of the colloidal particle, they are often considered equal to the true radius/diameter of the colloids when the hydrodynamic effects from the solvent is not significant and also when they are spherical.

The upper size limit of a colloid is defined by the Peclet number. Peclet number is the ratio between the Brownian time and sedimentation time,

$$Pe = \frac{\tau_B}{\tau_{sed}} \tag{1.3}$$

if $Pe < 1$, which means the particle diffuses faster enough to slow down the sedimentation of particles, the thermal energy of the particle is higher enough to overcome other external energy, the particle is considered a colloid. Therefore, $Pe = 1$ sets the upper limit of a colloid size[9]. Particles that have $Pe \gg 1$ are often considered as granular matter, where the effect of diffusion is small.

Due to the thermal motion of colloids, they are thermodynamically equivalent to atoms and small molecules[10]. The size of colloidal particles is in the range that can be conveniently observed by various microscopy in real space. Thus we can use colloids as model system to study properties such as phase behaviours of atoms which we cannot easily characterise using current experimental techniques.

Another advantage of colloids is that the interactions between particles can be tuned by tailoring particle surface properties or modifying the combination of solvents. For instance, the van der Waals attractive forces between two particles made from the same material can be shielded by having a solvent, which has the same refractive index of the particle. This produces colloids with hard sphere interactions as will be discussed in section 1.1.1. Repulsive forces between particles can be developed by bringing charges or grafting polymers onto particle surfaces, the range and strength of repulsion can be tuned by controlling charge concentration, polymer length and concentration. Attractive interaction can also be introduced by adding non-absorbing polymers which is caused by depletion, the range and strength of attraction can also be manipulated by the size and concentration of polymers, this will be discussed in more details in section 1.3. Combinations of these attractive and repulsive interactions will lead to a wide range of intriguing phase behaviours, which represent the fundamental aspects of more complex phenomena such as biological structures and processes[11, 12].

1.1.1 Hard spheres (HS)

The simplest interaction between two particles is hard sphere (HS) interaction, it can be expressed as equation 1.4 [13]. Particles do not have interaction with each other when the distance r between the centres of two particles is larger than particle diameter σ. Particles

also cannot overlap because the interaction becomes infinity when $r \leq \sigma$.

$$u(r) = \begin{cases} \infty & \text{for } r < \sigma, \\ 0 & \text{for } r \leq \sigma. \end{cases} \tag{1.4}$$

Since there is no interaction between particles when they are not interpenetrated, configurations that are accepted have zero potential energy. The system is thus entirely governed by entropy and temperature does not play a role. The only parameter that controls the phase behaviour of the monodisperse hard sphere colloids is particle volume fraction, $\phi = NV_p/V = \rho\pi\sigma^3/6$, where N is the number of particles, V_p is the volume of a single particle, V is the total volume of the system, $\rho = N/V$ is particle number density. The one dimensional phase diagram of hard sphere colloids is shown in Fig. 1.1.

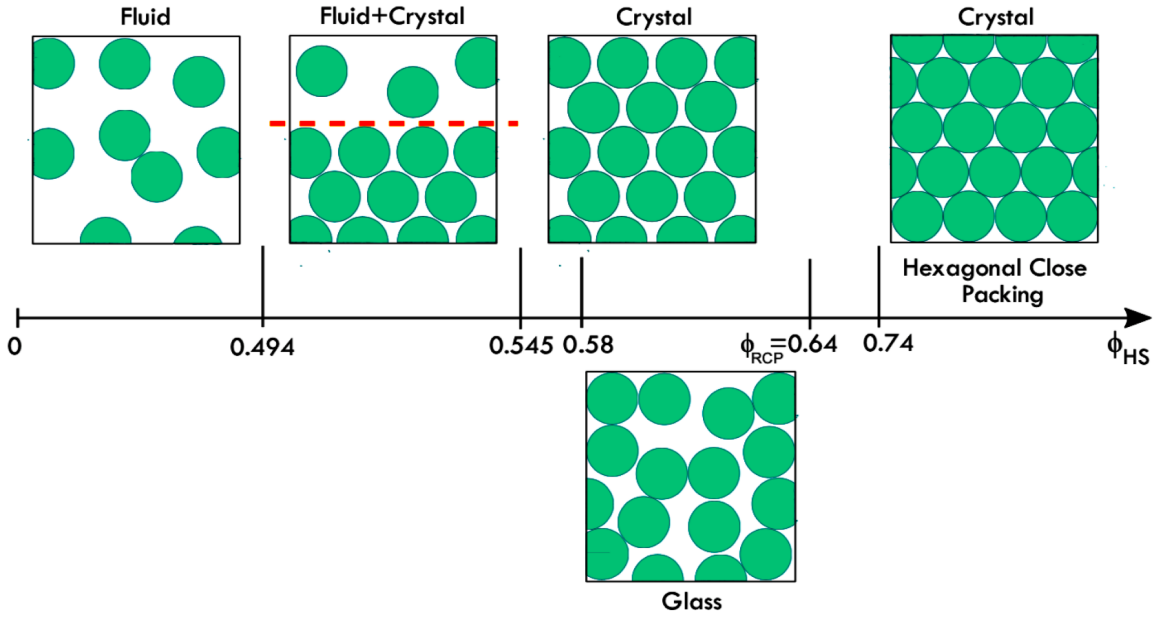

Fig. 1.1 Phase diagram of hard sphere colloids. The only axis in the phase diagram is the particle volume fraction ϕ. The freezing point is 0.494 and the melting point is 0.545, fluid and crystals coexist in this range of volume fractions. In equilibrium, only crystals should be found above the melting point until the maximum volume fraction of 0.74. However the system falls out of equilibrium if the volume fraction increases too fast. At high volume fraction $\phi > 0.58$, amorphous colloidal glasses are formed[13].

At low volume fraction when $\phi < 0.494$ which is the freezing point, the system is a fluid. Above the freezing point, crystals start forming and the system is in a coexistence state of crystals and liquid, until the melting point $\phi = 0.545$. Above the melting volume fraction, the

system should only consist of crystals. The maximum volume fraction is achieved when the system is in hexagonal close packing at $\phi_{hcp} = \pi/3\sqrt{2} \approx 0.74$.

However these crystal and coexistence phases are equilibrium states for hard spheres. If ϕ is increased from a low volume fraction fast enough, crystallisation is avoided and the liquid becomes supercooled. At higher volume fraction $\phi > 0.58$, the viscosity of the system increases dramatically of several orders of magnitudes, the system is therefore dynamically arrested and forms a glass. The upper bound of glass formation is the random close packing volume fraction $\phi_{RCP} = 0.64$, which is the maximum density of particles with completely random packing, particles are jammed above this volume fraction. To avoid crystallisation, polydispersity of particle sizes that is larger than 8% is required. As the polydispersity in the system increases, the phase boundaries will shift to larger values[8].

The first experimental demonstration of hard sphere phase diagram was achieved by Pusey and van Megan, where they also observed a colloidal glass transition[14]. The experimental system is colloidal suspensions of polymethylmethacrylate (PMMA) particles that are dispersed in a refractive-index and density matched mixture of cyclohexyl bromide (CHB) and cis-decalin. These colloidal particles are sterically stabilised by a thin layer (10 nm) of poly-(12 hydroxystearic acid) (PHSA). Because the experimental system contains particles with a simple and well-defined interaction, it allows the comparison with a wide range of other systems and with computer simulations, it can also be studied using various experimental technique such as microscopy, scattering and rheology, it is thus still widely used nowadays[8].

1.2 Colloidal glasses

In hard sphere colloids, rapidly increasing the volume fraction (or reducing the temperature), the system falls out equilibrium, liquids are supercooled. Approaching the glass transition, the dynamics in the system slows down dramatically, over a small change in volume fraction, the structural relaxation time τ_α and viscosity increase by many orders of magnitude, as shown in the Angell plot in Fig. 1.2. The experimentally determined glass transition temperature T_g is when the structural relaxation time τ_α rises to 100 s.

In the Angell plot, there are two types of glass formers: strong and fragile liquids. Strong liquids such as silica (SiO_2) have Arrhenius behaviour, the viscosity and relaxation time increase exponentially as temperature is reduced, as described in equation 1.5.

$$\tau_\alpha \propto \exp(\frac{E_a}{k_B T}) \tag{1.5}$$

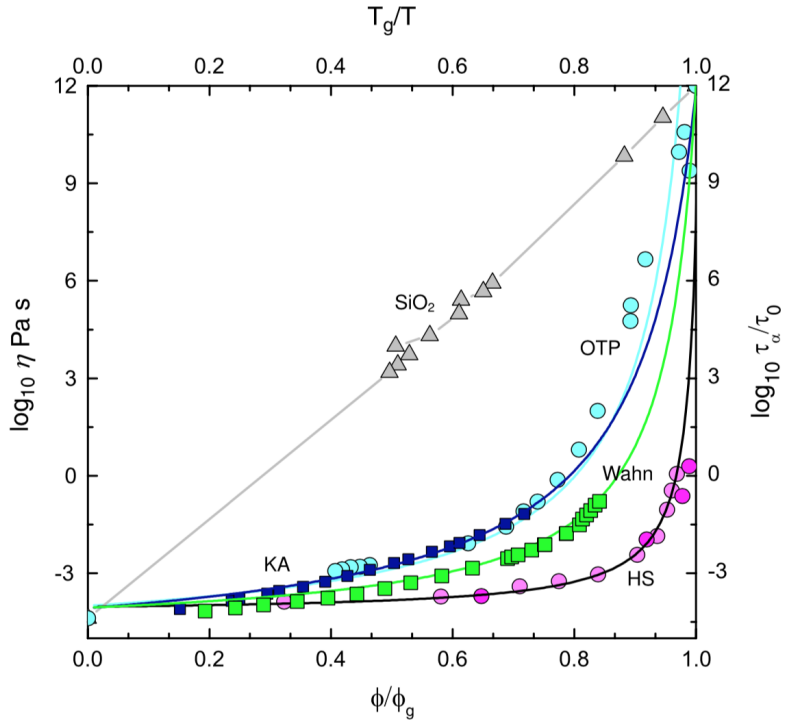

Fig. 1.2 The Angell plot: Liquid viscosity against inverse temperature scaled by T_g in Arrhenius representation. The behaviour of strong liquids is Arrhenius, characterised by an approximately straight line. This indicates the activation energy E_a is temperature-independent. Fragile liquids, by contrast, reveal super-Arrhenius behaviour, where activation energy grows as temperature decrease[15, 16].

This is approximated as a straight line in the Angell plot, indicating that the activation energy E_a is independent on the temperature. On the contrary, fragile liquids have characteristics of super-Arrhenius behaviour, the activation energy E_a increases when reducing the temperature. The relaxation time in the super-Arrhenius behaviour is often well characterised by the semi-empirical Vogel-Fulcher-Tammann (VFT) law,

$$\tau_\alpha = \tau_0 \exp[\frac{\tilde{E_a}}{k_B(T-T_0)}] \tag{1.6}$$

where T_0 is much lower than the experimental glass transition temperature T_g. The fragility - the degree to which the τ_α increase as approaching the glass transition temperature, is revealed by the value of $\tilde{E_a}$[15, 16].

The dramatic increase of viscosity and relaxation time when approaching T_g, turns the liquid to some kind of solid. Another typical solidification process, crystallisation, is a first-order (discontinuous) phase transition where there is clear symmetry breaking during

the transition between two equilibrium thermodynamic phases (liquid and crystalline solid). However the questions of whether there is a glass transition, and if any, what is the nature of the transition, are still not understood. Despite glassy materials being crucial in our daily life, the understanding of the nature of glass transition can help us develop glassy materials with novel properties, such as metallic glass which has demonstrated the possibility to manipulate glass into various shapes and colours and has superior mechanical properties.

In search of the truth of the glass transition, a wide range of experimental techniques and computer simulations have been applied, and various theories have also been proposed but the theory of the glass transition is still not unified. Some of these theories link clearly to the thermodynamics of the system (and thus are coupled to the structure). These include the Adam–Gibbs[17], energy landscape[18], and random first order transition[19] theories. Some, such as geometric frustration[20, 21], make explicit reference to local structures. Other theories are decoupled from the thermodynamics, such as dynamic facilitation[22].

1.3 Colloidal gels

Gels are complicated state of matter and there is not yet a unifying framework describing gels. A general definition of gel is that a disordered arrested state formed at low density, it does not flow and possesses solid-like properties like a yield stress[23]. The structure of a gel does not show significant order and therefore is liquid like, while a gel also has elastic and mechanical properties like a solid. In terms of the approach of gel formation, gelations can be divided into chemical and physical gelations.

Chemical gelation is usually associated with formation of irreversible or covalent bonds. At the chemical gelation point, the system stops flowing, and a fully connected (infinite space spanning) network is emerged with finite shear modulus and infinite zero-shear viscosity[23]. The transition of chemical gelation can be described by the mean-field percolation theory which was developed by Flory[24]. The chemically formed gel has a correlation at wave vector $q \to 0$ which corresponds to the infinite network, while it is quasi-ergodic for all other length-scales.

The bond energy in physical gels is typically of the order of $k_B T$, therefore bonds have the possibility to break and reform. Compared with the infinite bond life time in chemical gels, the bond life time in physical gels is transient and finite. One example of physical gel is colloidal gel which is formed by particles or droplets dispersed in a liquid solvent. The addition of non-absorbing polymers to colloids induces effective attractions to the system. This colloid-polymer mixture is described by spherically symmetric attractive potentials, and one famous example is the Asakura-Oosawa (AO) potential[25].

1.3.1 Asakura-Oosawa (AO) potential

In AO model, there are three types of interactions without considering hydrodynamics of the solvent. Firstly, colloidal particles with diameter of σ and radius a behave as hard spheres, the interaction between particles u_{cc} is described as equation 1.4. Secondly, non-absorbing polymers are treated as freely interpenetrable coils, they behave thermodynamically as an ideal gas therefore they do not have interactions with each other. The polymer - polymer interaction u_{pp} is

$$u_{pp}(r) = 0 \tag{1.7}$$

Finally, the interaction u_{cp} between colloids and polymers is also HS, meaning that polymers cannot overlap with colloidal particles,

$$\beta u_{cp}(r) = \begin{cases} \infty & \text{for } r < a + R_g, \\ 0 & \text{for } r \leq a + R_g \end{cases} \tag{1.8}$$

where $\beta = 1/k_B T$.

In the schematic of AO model in Fig. 1.3, the dashed lines indicate the depletion zones around colloidal particles, inside which centres of polymers are excluded. The volume of the depletion zone of a particle is equal to that of a sphere with radius of $a + R_g$. The total excluded volume can be estimated using Widom's particle insertion method[26]. Inside a colloid-polymer mixture with particle volume fraction ϕ and polymer to colloid size ratio $q = R_g/a$, the fraction of available volume for polymers is described as,

$$\alpha = (1-\phi) exp(-A\gamma - B\gamma^2 - C\gamma^3) \tag{1.9}$$

where $\gamma = \phi/(1-\phi)$, $A = 3q + 3q^2 + q^3$, $B = 9q/(2+3q^3)$ and $C = 3q^3$.

The osmotic pressure of the colloid-polymer mixture Π_e in experiments, is the same as the osmotic pressure Π_r of a pure polymer solution (called reservoir polymer solution), in which the number of polymers N_p is the same but the volume is only the available volume in the experimental colloid-polymer mixture. Therefore the reservoir polymer number density is higher than the experiment value, $\rho_{pe} = \alpha \rho_{pr}$. The reservoir value of polymer number density ρ_{pr} or polymer volume fraction $\phi_{pr} = \rho_{pr} v_p$ is a convenient parameter to determine the strength of AO interaction.

As we can see from all three types of interactions described above u_{cc}, u_{pp} and u_{cp}, there is no attraction in the system and the system is purely entropic. Therefore at a given particle volume fraction, polymers will explore a configuration to maximise its entropy (or minimise its energy) in the mixture. As shown in Fig. 1.3, when the surface to surface

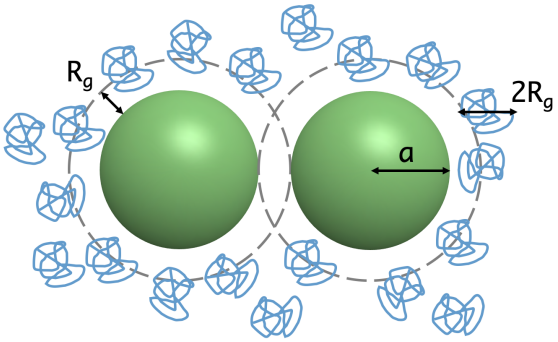

Fig. 1.3 Schematic of depletion interaction in mixtures of colloidal particles and non-absorbing polymers. Green spheres represent colloidal particles with diameter of σ and blue coils are non-absorbing polymers with gyration radius of R_g. Dashed lines represent depletion zones which have an extra distance R_g from surfaces of colloidal particles[27].

distance of two particles are smaller than the diameter of the polymer $2R_g$, *i.e.* depletion zones are overlapping, the free volume for polymers will increase. Polymers cannot access the overlapping regions, and polymers have higher entropy due to the increase of free volume. This results imbalanced osmotic pressures and leads to an effective attractive depletion force between the two particles.

The effective attraction comes entirely from the entropy of polymers, therefore the strength of attraction depends the overlap of depletion zones around colloidal particles. The AO potential between two colloids with separation of r can be defined as follow[28],

$$u_{AO}(r) = \begin{cases} \infty & \text{for } r < \sigma \\ -\Pi_p V_{overlap} & \text{for } \sigma \leq r < \sigma + 2R_g \\ 0 & \text{for } r \geq \sigma + 2R_g \end{cases} \tag{1.10}$$

where $\Pi_p = \rho_{pr} k_B T$, the overlap volume is

$$V_{overlap} = \left[1 - \frac{3r}{2(1+q)\sigma} + \frac{r^3}{2(1+q)^3 \sigma^3} \right] \times \frac{\pi}{6} \sigma^3 (1+q)^3 \tag{1.11}$$

From equation 1.10, given the colloid volume fraction ϕ_c, polymer concentration C_p (or polymer reservoir volume fraction ϕ_{pr}), sizes of colloidal particles and polymers, we are able to calculate the AO interaction potential in the colloid-polymer mixture. The potential well depth is proportional to the polymer concentration, and the range of the potential depends on the polymer to colloid size ratio q. Higher polymer concentration leads to a deeper potential well, so that stronger attraction strength. Polymer concentration ϕ_{pr} can be considered as the

parameter of an effective inverse temperature $1/T$, increasing polymer concentration equals to cooling or quenching the system.

1.3.2 Phase behaviours

In a theoretical description of AO model proposed by Asakura and Oosawa and also Vrij, as the concentration of polymers increase above a critical value, the suspension will phase separate to colloid-rich and colloid-poor phases due to the depletion interaction. The latter phase is normally considered as a gas phase, whereas the colloid-rich phase can be a liquid like phase or even a solid phase with crystal arrangements[25, 29].

The phase behaviour of a system is governed by the ratio of interaction energy $u(r)$ and k_BT. Unlike atomic systems in which the behaviour is tuned by temperature T while the interaction energy is fixed. In colloid-polymer mixtures, the temperature T is fixed, the polymer volume fraction ϕ_p controls the interaction strength $u(r)$, therefore ϕ_p is equivalent to inverse temperature $1/T$ for atomic systems.

The range of AO potential is controlled by the polymer to colloid size ratio $q = R_g/a$, the phase behaviour of colloid-polymer mixture also depends on the choice of q. Lekkerkerker *et al*[30] calculated phase diagrams of colloid-polymer mixtures using free-volume theory (FVT), two types of phase diagrams are found depending on the range of AO interaction, as presented in Fig. 1.4.

When no polymer is added, the phase behaviour is pure hard sphere, with a fluid - crystal coexistence region at $0.494 < \phi_c < 0.545$. For short range AO interactions with $q \lesssim 0.32$, adding non-absorbing polymers strongly broaden the fluid - crystal coexistence region, as shown in the blue region in Fig. 1.4 (a). With further addition of polymers, the mixture will phase separate to colloid-rich (colloidal liquid) and colloid-poor (colloidal gas) phases, which is a metastable state. The colloidal liquid phase itself has very high density which is similar to that of a colloidal glass. The high density slows down the dynamics dramatically, and leads to a dynamical arrest in the liquid phase. This consequently impedes the mixture further phase separate to thermodynamically stable gases and liquids. This state is commonly considered as a colloidal gel.

In the other scenario with longer range of interaction, for $q \gtrsim 0.32$, critical and triple points emerge in the phase diagram, as shown in Fig. 1.4 (b). This is similar to that of a simple atomic material such as C_{60} and Argon[31, 32]. Different from the phase diagram of the short range attraction, there are stable liquid and gas phases in the phase diagram of long range interaction. When the polymer concentration is higher than the critical point, the fluid phase separates to metastable liquid and gas phases (a gel state). The dashed line

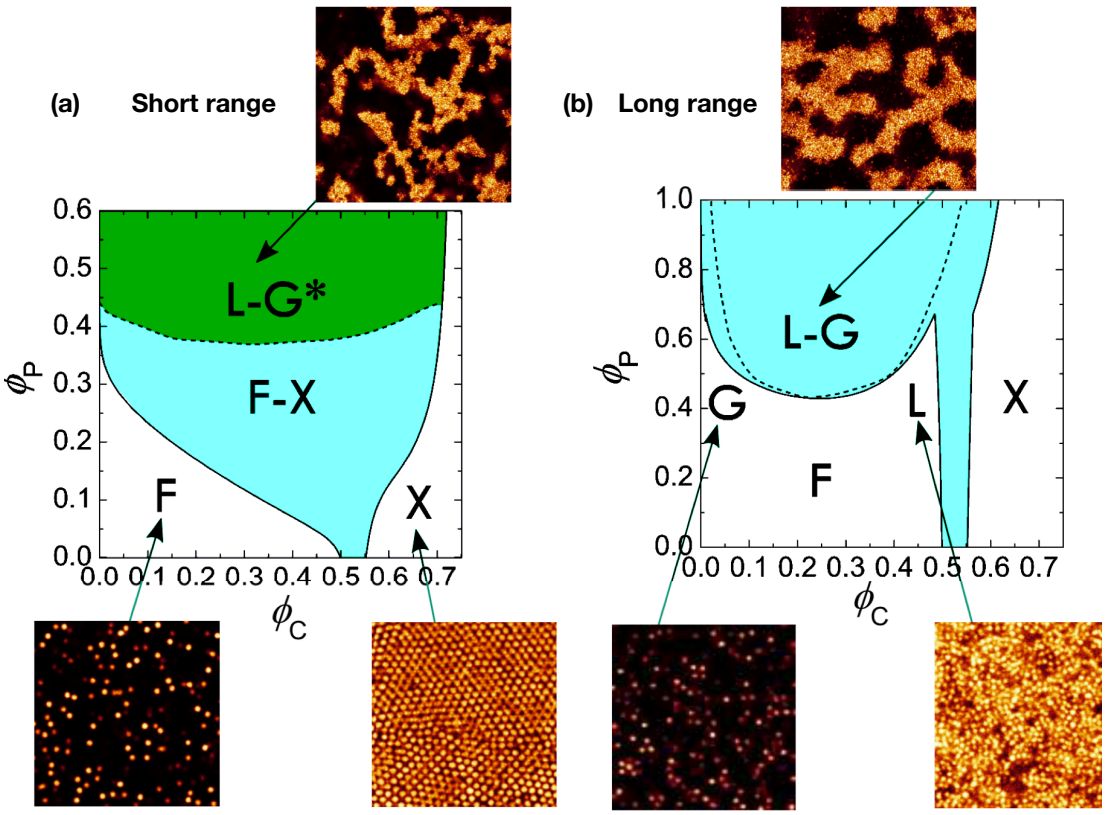

Fig. 1.4 Phase diagrams of colloid-polymer mixtures. (a) A short-range system with $q \lesssim 0.32$. (b) A long-range system with $q \gtrsim 0.32$. The x-axis is the colloid volume fraction ϕ_c and y-axis is polymer reservoir volume fraction ϕ_p which is equivalent to inverse temperature $1/T$. Images are confocal images of colloid-polymer mixtures, demonstrating the characteristic features of certain phases in the phase diagrams[27, 30]. The meanings of symbols in the phase diagrams are: L - liquid, G - gas, F - fluid, and X - crystal.

indicates spinodal instability, which is inside binodal lines *i.e.* the equilibrium liquid - gas phase boundaries.

1.3.3 Other colloidal gels

Colloid-polymer mixtures are out-of-equilibrium gels because locally dense configuration is formed in the metastable region and undergoes dynamical arrest with relaxation time longer than the experimental observation window. Other out-of-equilibrium gels such as Diffusion-Limited-Cluster-Aggregation (DLCA) gels are formed at very low particle density and strong attraction strength which is much higher than k_BT, so that they are regard as irreversible. This type of gel is the percolation of aggregated clusters rather than particles, and inside the gel, phase separation is kinetically arrested due to the freezing of bonds[23].

Equilibrium gels are formed continuously through a series of equilibrium states, from fluids to equilibrium clusters and further to stable particle networks. These gels can be realised by introducing sufficiently long range repulsions in the attractive system, such as controlling the residual charges on particles by adjusting salt concentrations. The repulsive barrier prevents phase separation, and pushes phase separation at larger attraction strengths. Alternatively, inducing directional interaction potentials in colloidal systems (*e.g.* patchy particles) leads to lower the coordination number and thus shifts the critical point to lower particle density. These two approaches either increases the attraction strength or reduces the particle volume fraction of the phase separation critical point in order to obtain equilibrium gels[23].

1.4 Structural measurements

1.4.1 Pair correlation function

The pair correlation function $g(r)$, also known as radial distribution function, measures the probability of finding a particle at a given distance r from the reference particle, it characterises how density varies in the system. Given a reference particle as shown in Fig. 1.5 (the grey particle), the method needs to find the number of particles $n(r)$ whose centres are within the distance between r and $r+dr$, *i.e.* how many orange particles are within the dotted spherical shell, which has a volume of $4\pi r^2 dr$. This gives the local number density $\rho(r) = n(r)/(4\pi r^2 dr)$. The pair correlation function $g(r)$ is the ratio between the local number density in the sample and number density in the ideal gas, *i.e.* $\rho(r)/\rho$ where $\rho = N/V$. The way of computing $g(r)$ is first calculating distances between each pair of particles, and binning distances into histograms; the histograms are then normalised with histograms of an ideal gas, after which we can obtain the $g(r)$.

The example in Fig. 1.5 shows a $g(r)$ of a hard sphere liquid at volume fraction of 0.4. When $r < \sigma$, $g(r)$ stays at zero, showing that no particle is found within a distance of σ which means particles cannot overlap. The first and highest peak appears at $r = \sigma$, corresponding particles within the first shell. The second peak corresponds to the probability of finding particles in the second shell with respect to ideal gas. As r increases larger than 4σ, the peak disappears and $g(r)$ decays to 1, which means there is no spatial correlations between particles beyond this distance.

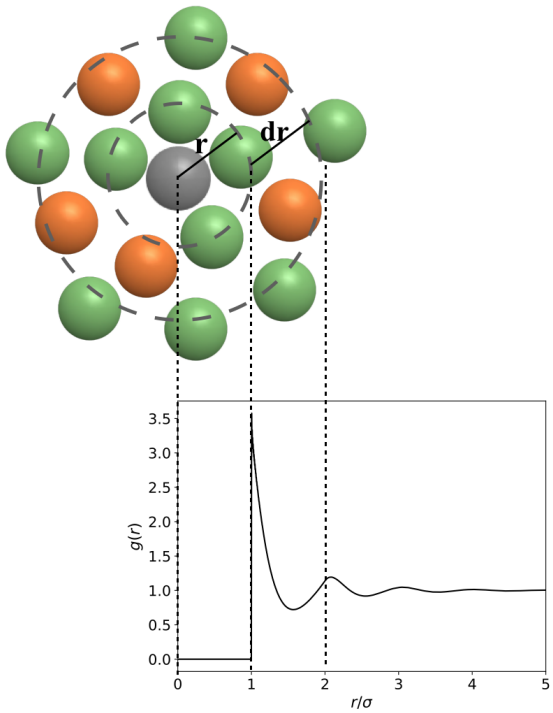

Fig. 1.5 Shematic of calculation of the pair correlation function and the $g(r)$ of a hard sphere liquid at volume fraction of 0.4.

1.4.2 Topological cluster classification

It has been shown that two-point correlation function such as pair correlation function has difficulty probing structural differences in amorphous systems. Higher order structural correlations are therefore demanded to measure structural characteristics in disordered systems. One sufficient method is the topological cluster classification (TCC), which was developed by Malins *et al*[33].

Given a configuration of particles, the TCC algorithm detects the arrangement of m particles whose bond network is similar to that found in the minimum energy clusters of a given interaction potential, as shown in Fig. 1.6. The algorithm can therefore identify the link between given model of interest and structural ordering in the system, by searching the minimum energy clusters.

An overview of the TCC algorithm is described as follow[33]. First the algorithm identifies neighbours of each particle. Secondly, the particle and its neighbours form a network which is searched for shortest-path ring of 3, 4, and 5 particles, as shown in Fig.1.7. Thirdly, from the shortest-path rings, when there are additional particles that are common neighbours of all the particles in a shortest-path ring, additional particles along with the shortest-path ring particles are distinguished as basic clusters. Finally, by adding one or

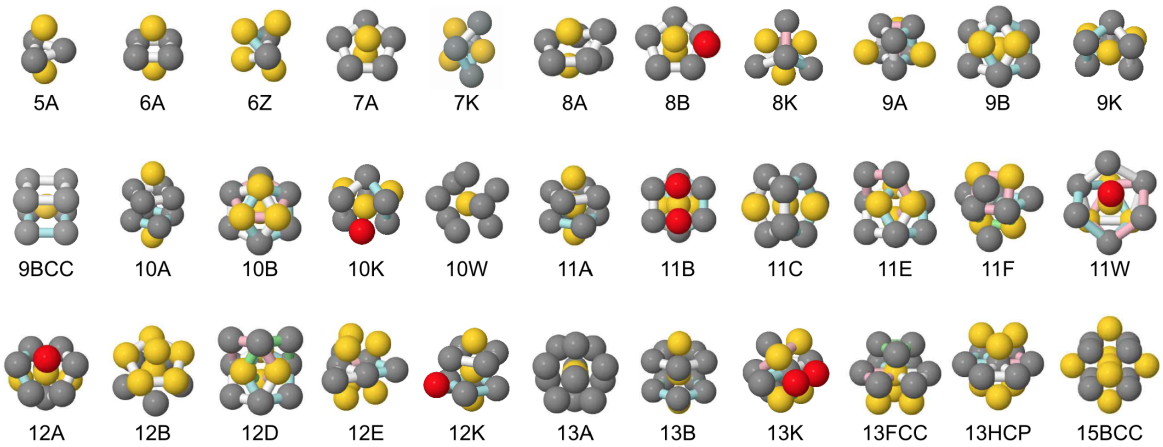

Fig. 1.6 Minimum energy clusters with $m = 5$ to 15 particles. The letter after the number represents different interaction potentials[33].

two separately bonded particles or combining basic clusters together, larger clusters can be determined. The method outputs structures with similar topology to the structures with bond networks of the minimum energy clusters found in various interaction potentials (Fig. 1.6).

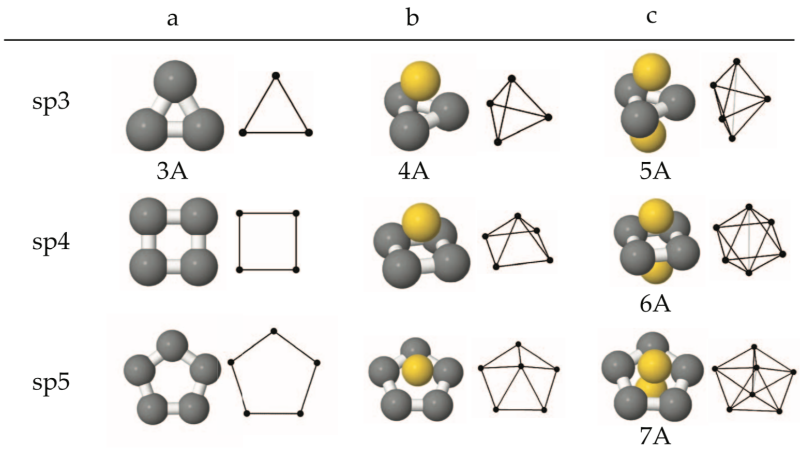

Fig. 1.7 The basic clusters identified from shortest-path rings with 3, 4 and 5 particles. Rendering of basic clusters: gray and yellow particles represent ring and spindle particles respectively, particle bonds are in white[33].

In order to identify local structures, the way of detecting nearest neighbours is crucial. Voronoi method is one of the standard techniques to find particle neighbours. Voronoi tessellation decomposes space into non-intersecting domains called Voronoi cells, they are convex polyhedra in three dimensions. Each contains only one particle, and cells have distinct boundaries. In the standard Voronoi method, if two particles share a face of their Voronoi cells, they are considered as neighbours; if they only share an edge or a vertex, they are

not bonded. In TCC algorithm, if the line joining two neighbouring particles do not cross their shared face, they are called indirect neighbours and the bond will be removed, because these indirect neighbours tend to cause the misrecognition of second-nearest neighbours as first-nearest neighbours.

The TCC algorithm also introduces a control parameter f_c called four-membered ring parameter, which determines the maximum degree of distortion that a four-membered ring structure can have. In the standard Voronoi method, if a four-membered ring structure has some asymmetry, it will possibly be detected as two triangle rings, therefore the performance is poor in terms of finding four-membered rings. By allowing some degree of distortion, TCC algorithm works better in identifying clusters with fourfold symmetries, such as octahedral.

TCC is heavily inspired by an idea proposed by Charles Frank[**?**]. He pointed out that during the cooling process of a liquid, if the symmetry of the structures formed on short length-scales is incompatible with that of the bulk crystal symmetry, the structures would remain under-cooled liquid and inhibit crystallisation. TCC is therefore developed to detect clusters with different symmetries especially fivefold symmetry which cannot tile entirely in a three dimensional Euclidean space. It has been widely employed in both experiments and simulations to study the glass transition and nucleation processes.

Taffs *et al*[34] performed simulations on supercooled liquids with a model where the degree of fivefold symmetry can be tuned. They have shown that increasing fivefold symmetry in the system would suppress crystallisation process but has little effect on growth rate. The thermodynamic effect of fivefold symmetry suppresses freezing and the phase boundary moves to higher densities and pressures. Fivefold symmetry also has kinetic effect which suppresses the homogeneous nucleation of FCC crystals, and this suppression arises from the increasing interfacial energy between fluid and crystal.Colloidal experiments have been carried out by Wood *et al*[35] to investigate the influence of sedimentation on hard sphere nucleation. The TCC algorithm was applied to the system with tuned degree of density mismatch, to detect local structures with fivefold symmetry. They discovered that by inducing sedimentation, fivefold symmetry is suppressed by a factor of two, and consequently changes the expected nucleation rates. However the effect is too small to explain the staggering discrepancy of nucleation rate in hard sphere experiments and simulations.

As for the study of the glass transition, Pinchaipat *et al*[36] prepared hard sphere colloidal experiments and employed TCC to identify locally favoured structure (LFS) in colloidal supercooled liquids. As the density increases, they found existence of a purely dynamical first-order transition in trajectory space between a normal liquid and a LFS-rich phase. Supercooled liquids with relaxation time three orders of magnitude longer than conventional experiments have been achieved by Hallett *et al*[37], by preparing colloidal particles at a

few hundred nanometre scale and using stimulated emission depletion (STED) microscopy. They probed the local structures of different supercooling states by using TCC algorithm, and found at deep supercooling, icosahedron is more stable than the defective icosahedra and there is a stronger correlation between dynamics and LFSs. By showing that local structure is significant at deep supercooling, they claim the glass transition can be interpreted by geometric frustration which is a thermodynamic description, rather than approaches which prioritise dynamic aspects.

1.5 Microfluidic emulsification

Emulsions are mixtures of two immiscible fluids, they are widely used in food, cosmetic, personal care and agrochemical industries. An emulsion is generally one dispersed liquid in another immiscible liquid which is called the continuous phase[38]. In an oil and water mixture, emulsion droplets are formed when enough mechanical agitation is introduced to the system, however it will eventually phase separate due to high interfacial tension between oil and water. Surfactants which are amphiphilic molecules, preferentially stay in between oil and water interfaces, thereby reduce the interfacial tension and act as stabilisers for emulsion droplets.

The most common method to produce emulsion droplets in industries is using homogenisers. A homogeniser can provide high mechanical energy at various shear speed in an oil and water mixture, it efficiently breaks the dispersed phase into droplets and can also be applied in large scale production. The size of droplets is mainly controlled by the shear speeds, shear time, surfactant concentrations and viscosity of fluids[38]. The size distribution of produced droplets is broad, the polydispersity is often above 20%. Bibette [39] proposed the method of fractionating polydisperse emulsions to reduce polydispersity. Due to the size difference of droplets, droplets will cream or sediment at different speed under gravity, at a particular height in the sample vial, it contains droplets with a narrower size distribution, compared with droplets in the whole vial. By fractionating crude emulsions for several times, droplets are obtained with much less polydispersity. However this method still struggles to produce droplets with polydispersity less than 8%, which is crucial in studying colloidal crystals.

Microfluidic devices offer channels for mixing fluids at micron scales, the volume of operating fluids is from μL to fL. Fluids flowing through microfluidic channels are in laminar regime mainly due to the low flow rate in micron sized channels. Laminar flows play an important role for producing monodisperse droplets. The controllable production of micron scale emulsions is an area of highly active research. Allowing extreme reductions in sample volumes, microdroplets currently find use across both fundamental research

and industrial applications. One promising manufacturing method for these droplets is microfluidic emulsification [40]. Offering unparalleled control over droplet formation, microfluidic emulsification systems have been applied in the generation of artificial cells [41], high-throughput screening of patient samples [42–45], colloidal model systems [46], or even traffic dynamics [47].

1.5.1 Dimensionless numbers in microfluidics

Physical properties of microfluidic devices can be characterised by a number of dimensionless numbers, despite different designs and geometries of microfluidic devices. Among all dimensionless numbers, Reynolds number *Re* and Capillary number *Ca* are the most import parameters in droplet microfluidics.

Reynolds number *Re* relates inertial forces to viscous forces, is calculated:

$$Re = \frac{Inertial}{Viscous} = \frac{\rho U_0 L_0}{\eta} \tag{1.12}$$

where ρ is the fluid density, U_0 is characteristic velocity scale, L_0 is the typical length scale, η is the fluid viscosity. Due to the low flow rate and small dimension, $Re \ll 1$ is often found in microfluidic devices. This shows that inertial forces are small enough so that inertial effects are irrelevant. Low values of *Re* guarantee that viscous forces are typically much larger than inertial forces, the non-linear term in Navier-Stokes equations can be neglected and the resulting flows are linear.

When two immiscible fluids meet and form an interface, the interfacial tension between the two fluids tend to minimise the interfacial area, while the viscous stress will drag the interface downstream. The competency from the interfacial tension and viscous drag is characterised by the capillary number *Ca*,

$$Ca = \frac{Viscous}{Interfacial} = \frac{\eta U_0}{\gamma} \tag{1.13}$$

where γ is the interfacial tension between the two immiscible fluids. The competing stresses from the two factors result in the capillary stresses which destabilise the interface. The interface forms Rayleigh-Plateau instability and droplets with radius of *R* break up from the jet interface. In some dripping and jetting regimes, drop radius scales inversely with *Ca*[48].

1.5.2 Device geometries and droplet formation regimes

Conventionally, droplet generation in a microfluidic device is achieved via three main geometries as shown in Fig. 1.8: (a) coaxial devices where an outer continuous phase fluid

flows parallel to and surrounding an inner dispersed phase fluid until droplet generation occurs via stretching of the fluid interface [49], (b) flow-focusing devices, where the interface between co-flowing streams are forced through a flow constriction causing droplet breakup through the generation of a velocity gradient [50] and (c) T-junctions in which viscous shear stress at one fluid interface pulls off droplets into the flow of a second immiscible fluid [51].

Drop formation depends on the growth or suppression of the instability of the interface. Depending on where the instability happens, there are typically two regimes of droplet generation regime, dripping and jetting. When the instability happens at the junction, it is called a dripping regime, while jetting occurs when instability occurs downstream away from the device junction. Droplets break up through dripping normally have sizes comparable to the size of the device channels, while in the jetting regime, the jet is independent of the dimension of the source, jets that are much smaller than the source dimension can form and thus form very small droplets[52].

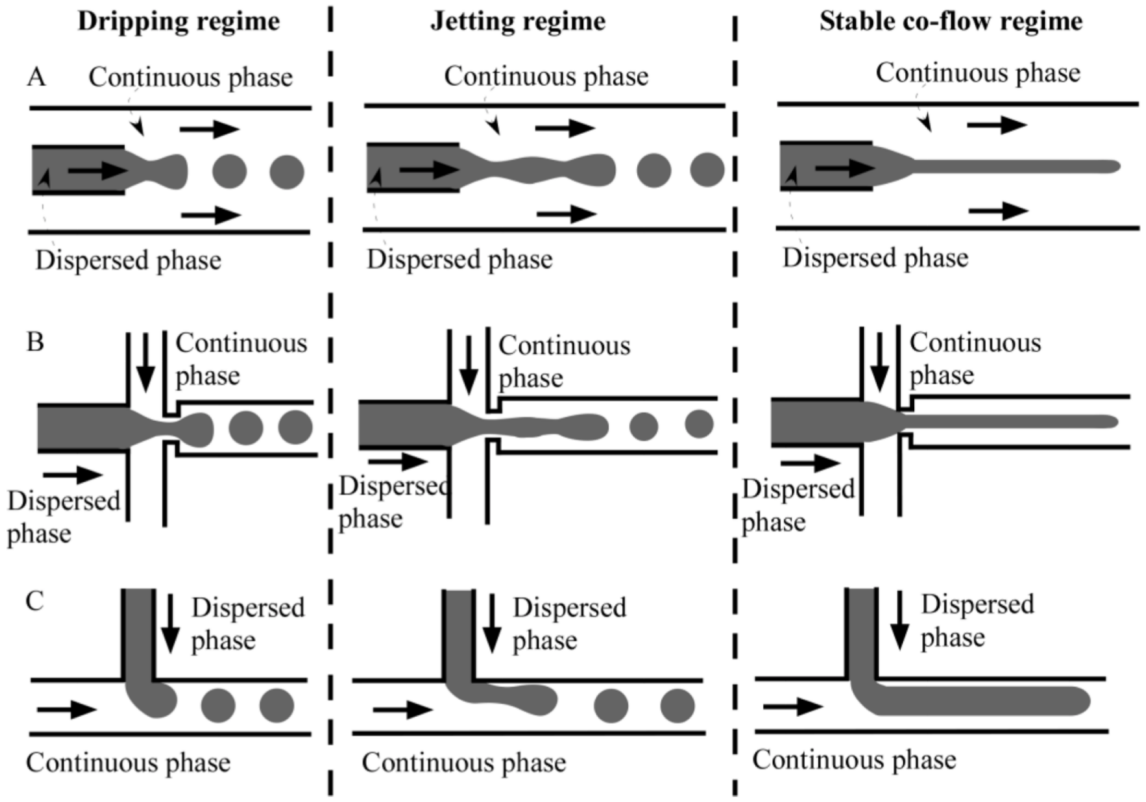

Fig. 1.8 Schematic of different flow regimes in Example geometries used in a (A)coaxial, (B)flow focusing and (C) T-junction microfluidic device[52].

In a coaxial flow device, in the jetting regime, droplets breakup due to the Rayleigh-Plateau instability, so the droplet size scales linearly with the jet radius; while in the dripping regime, the size of droplet is comparable to the channel width of the dispersed flow.

In a flow focusing device, dripping and jetting regimes have both been observed. In the dripping regime, it has been found that droplet radius either scales inversely with Ca, or is affected by the flow rate ratio of two fluid phases. In the jetting regime, droplets are formed due to a combination of the natural growth of the interfacial instability and the viscous shear stresses form the continuous flows[53, 54].

In a T-junction device, squeezing and dripping modes are most common regimes to produce droplets. In the squeezing regime, when the dispersed phase reaches the junction, it increases the pressure for the continuous flow and thus creates a pressure gradient. When the pressure is higher than the pressure inside the tip of the disperse phase, the interface starts to deform and neck, the neck eventually breaks up into droplets. In the dripping regime, droplets break up mainly due to the viscous shear stresses exerted by the continuous flow, generated droplets are typically smaller than the size of channels and scale inversely with Ca.

Droplet generation regimes strongly depend on the capillary number Ca, the transition from dripping to jetting can occur by controlling the parameters which affect Ca. When increasing the flow rate of continuous phase, the interface will experience higher shear stresses which stretch the interface further downstream, till a distance where interfacial tension is balanced and droplets break up. Jetting can also happen when the inertia of the dispersed phase play an role, *i.e.* the Reynolds number of dispersed flow $Re > 1$, so that the inertia drags the interface downstream in the channel[55].

1.5.3 Review of small droplet generation

However, while these methods can effectively produce droplets with sizes below 100 μm, the production of true micro-droplets with sizes below 10 μm in diameter via microfluidic means remains a significant challenge. Typical droplet sizes realized in previous microfluidic set-ups are summarized in Table 1.1. To produce smaller droplets, one possibility is to reduce the size of the microfluidic device, but this is limited by the resolution of the manufacturing process available [53]. In addition, small channel sizes lead to both large velocity gradients and large pressure gradients needed to drive the flow. Furthermore,smaller device sizes lead to a significant increase in the surface are to volume ratio of the fluids, and thus a larger dependence on the chemical compatibility of the fluids. As a result, emulsification on the micron scale remains a largely unexplored field for oil-in-water systems in particular.

In order to generate multiple sizes of droplets in a single chip, Link *et al*[56] designed two geometries, a T-junction where stretched thin droplets break up into two small droplets

Table 1.1 Comparison of microfluidic droplet generation methods

Droplet generation method	Emulsion type	Water droplet diameter	Oil droplet diameter
Geometric break-up	W/O [56]	50 μm	-
T-junction	W/O [57] or O/W [58]	50 μm	100 μm
Capillary coflow	W/O or O/W [59]	20 μm	10 μm
Partial wetting	Fluorinated O/W [60]	-	6 μm
Dripping	Fluorinated O/W [61]	-	3 μm
Flow focusing	W/O [50] or O/W [62]	10 μm	20 μm
Flow focusing (converging and diverging nozzle)	W/O [63]	10 μm	-
Flow focusing (flow films on needle)	Oil-in-air and O/W [64]	-	1 μm
Tip-streaming	W/O [65]	3 μm	-

due to the pressure drop; and a obstruction-mediated breakup design, where obstructions are placed inside channels, daughter droplets are obtained when large droplets pass through the obstacle, as shown in Fig. 1.9 (a). Daughter droplet sizes and polydispersity can be controlled by tuning flow rates, length ratio of splitting channels, the position and size of obstacles.

A converging-diverging nozzle is applied to achieve flow focusing regime. The converging part is designed for increasing the velocity and the pressure of inlet dispersed fluid while the diverging part next to it is creating opposite effects. This leads to a maximum velocity and pressure gradient near the nozzle throat where droplet breakup takes place[63]. Bardin *et al*[61] managed to obtain 3 μm droplets in the dripping regime in a flow focusing device with the converging-diverging nozzle, as shown in Fig. 1.9 (b).

In many droplet producing regimes, geometry confinement is one limitation for producing small droplets, therefore reducing the channel dimensions is a possible way to generate ultra-small droplets. Shui *et al*[66] fabricated nanochannels with height from 100 to 900 nm using standard photolithographic technique, as shown in Fig. 1.9 (c). By suddenly increasing the outlet channel diameter, the confinement is removed and capillary instability was therefore induced for droplet breakup. They were able to produce water-in-oil droplets down to 400 nm in diameter, the droplet breakup also was only influenced by the channel height rather than flow rates, surfactants and liquid properties.

Gañán-Calvo[67] proposed a core liquid - sheath liquid - focusing gas, double flow-focusing arrangement. The most inner liquid (*eg.* mercury or aqueous solutions) formed a continuous steady jet down to sub-micron by the middle sheath liquid capillary jet (*eg.* silicone oil), which was focused by the outer gas fluid, as shown in Fig. 1.9 (d). This pure hydrodynamic means can produce mercury droplets as small as 600 nm in diameter

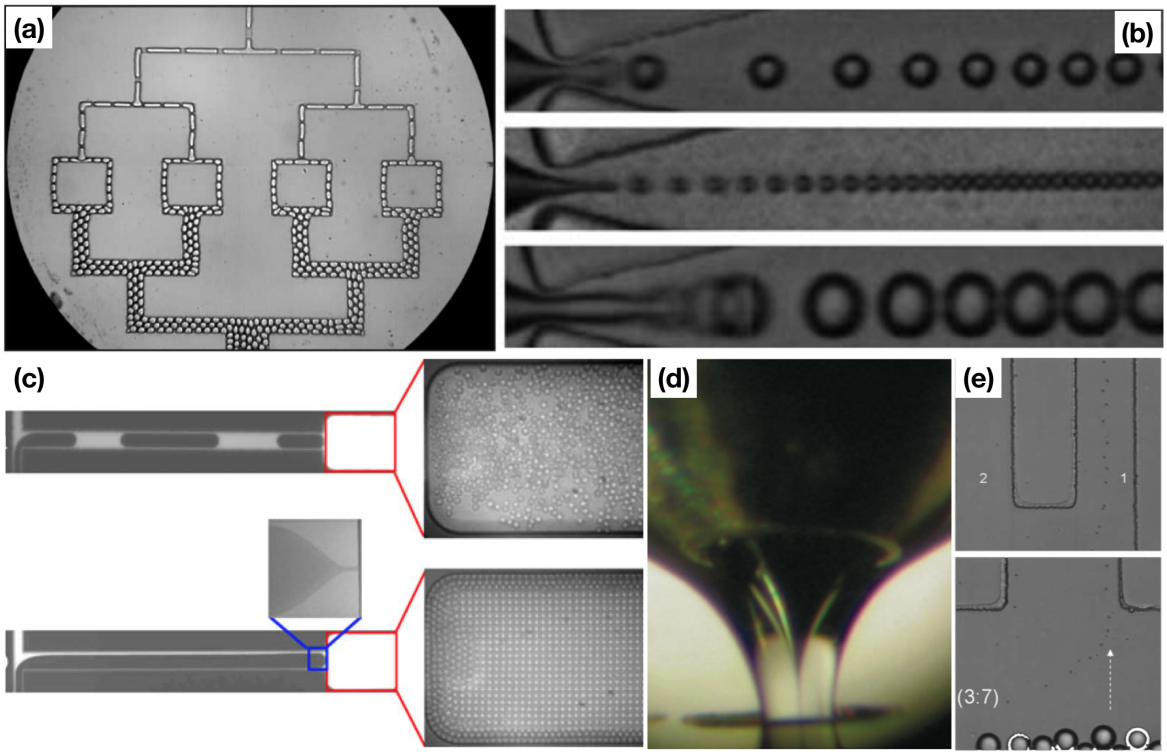

Fig. 1.9 Microfluidic emulsification of small droplets. (a) Small droplets are obtained by sequentially breaking large droplets, using channels as obstructions[56]. (b) Flow focusing device with a converging-diverging nozzle[61]. (c) Nanochannels are placed at the device junction, combining with a large outlet channel, droplets with size as small as 400 nm are obtained[66]. (d) Double flow focusing. Sub-micron mercury jet is formed by the middle sheath liquid, which is again focused by the outer gas fluid[67]. (e) Primary and satellite droplets which have sizes from 2.3 μm to 0.4 μm are separated in microfluidic channels[68].

in silicone oil, and the sub-micron capillary jets generated in this configuration are close to the continuum limit. However, for this method to work, highly aligned two needles with an exit orifice were required which is an difficult experimental set-up therefore has limited applications.

Satellite droplets which were produced due to the surface instabilities during the continuous threads breakup, commonly exist in microfluidic emulsifications. The size of satellite droplets which is typically around 1% of parent droplets, can be separated by shear strength gradient. Tan *et al*[68]were able to separate primary, secondary and even tertiary satellite droplets, these droplets have size from 2.3 μm to 0.4 μm, as shown in Fig. 1.9 (e). This is a clever way to collect colloidal oil droplets, however the complicated design of the system indicates its difficulty to be used in general applications.

Chapter 2

Experimental and Image Processing Techniques

2.1 Colloidal emulsion synthesis

Silica and PMMA particles have been widely used as colloidal model systems to study phase behaviours of soft matter, there have been a huge number of literatures presented a number of methods synthesising silica and PMMA particles with various sizes, polydispersity and shapes. However, monodisperse silicone oil droplets were first synthesised by Obey and Vincent in 1993[69]. They proposed a spontaneous nucleation and growth method of silicone oil which is analogous to the St*ö*ber process[70].

The original St*ö*ber process is a one-step process, in which the hydrolysis and condensation of the molecular precursor occur together, macroscopic particles are produced after growing for a certain amount of time[70]. In the example of silica particle, tetraethylorthosilicate (TEOS) is hydrolysed in water and alcohol mixtures, with ammonia as catalyst. The reaction produces various types of ethoxysilanols (depends on the degree of hydrolysis) which can then condense to nuclei or aggregates with other silanols and lose water. The final size and polydispersity of particles prepared by St*ö*ber process ultimately depend on the competition between the hydrolysis and condensation rate. For example, higher initial TEOS concentration leads to greater number of nucleation sites, therefore results in smaller particle sizes and higher polydispersity.

Using the same principal and changing the molecular precursor to dimethyldiethoxysilane (DMDES), Obey and Vincent were able to produce monodisperse PDMS oil droplets in the size range 1-5 μm[69]. The processes of hydrolysis and polymerisation reactions are spontaneous due to the negative enthalpy change, and the dynamic interfacial tension between

oil molecules and water is lowered by transferring the alcohol across the interface. Modified methods have been proposed by Elbers *et al*[**?**] without using ethanol for the reaction.

Without the presence of ethanol, the oil precursor does not mix with water completely at the beginning. Hydrolysis of oil molecules produces slightly acidic silanol groups and therefore increases the water solubility of monomers. The increase of interfacial area between oil molecules and water, improves the hydrolysis rate of the monomers, therefore the solubility and ionic strength. This can be achieved by adding mechanical energy to the system using homogeniser or vortex mixing, which is considered as a prehydrolysing step. The prehydrolysed oil and water mixture will condensate to droplets immediately when the catalyst ammonia is added. In this thesis, we mostly followed the method of Elbers *et al*[**?**] to prepare monodisperse colloidal droplets as the model system for studying the stress transmissions in gels.

2.1.1 Emulsion synthesis procedures

Monomers of DMDES were prehydrolysed by mixing them with deionised water with a volume ratio of 2:5. The mixture was stirred on a vortex mixer at a speed of 1300 rpm for 6 min, after which there is no separation between water and DMDES. The mixture was then placed on a roller at a speed of 26 rpm for up to 24 hours to homogeneously hydrolyse DMDES monomers. To prepare silicone oil droplets, the prehydrolysed DMDES (9% v/v) was added to an aqueous ammonia solution with ammonia concentration of 22.7% v/v, and the mixture was immediately placed on a vortex mixer for 5 min at a speed of 1300 rpm. After vortex mixing, the opaque sample was placed on a roller at speed 26 rpm for 72 h for droplet growth. The synthesis is then followed by a dialysis process with 1 mM SDBS to remove the ammonia from the emulsion while avoid droplets from coalescence by introducing surfactants. The dialysis is finished when the pH of the emulsion stays around 7.

It is often observed an layer of oil at the top of the sample after dialysis. This is the extra oil that is not completely reacted. This layer of oil is removed in order to reduce the polydispersity of the sample. Surfactant solutions of 50 mM sodium dodecylbenzenesulfonate (SDBS) are added to the emulsions resulting an surfactant concentration of 2 mM in the emulsions. The critical micelle concentration CMC of SDBS is about 0.4 mM[71]. Salt solutions of KCL are also added to a concentration of 20 mM in emulsions, in order to screen out charges on the droplet surfaces. The dilute emulsions are then concentrated under gravity for up to 2 weeks depending on the size of the droplets. The concentrated emulsions are then fluorescently labelled with Nile Red dye. Glycerol is added to the dyed emulsions drop by drop, until the sample becomes transparent with a pink color for refractive index matching. This yields the weight ratio of water to glycerol around 51% : 49%, and the refractive index

is 1.40 at 20°C. The index matched emulsions are centrifuged at 1000 rpm for 20 min to 1h (depends on the size), until the volume fraction of the creamed emulsions reached random close packing.

2.1.2 Characterisation of synthesised emulsions

Through the bottom up approach using the synthetic method, the size of final oil droplets varies according to the prehydrolysing time of DMDES monomers. As shown in Fig. 2.1(a), the droplet size decreases from 4.5 μm to 1.5 μm by increasing prehydrolysing time from 0.5 h to 24 h. The longer time DMDES monomers were prehydrolysed, the higher nucleation rate was obtained when the monomers were presented in a ammonia solution, therefore leading to smaller droplets.

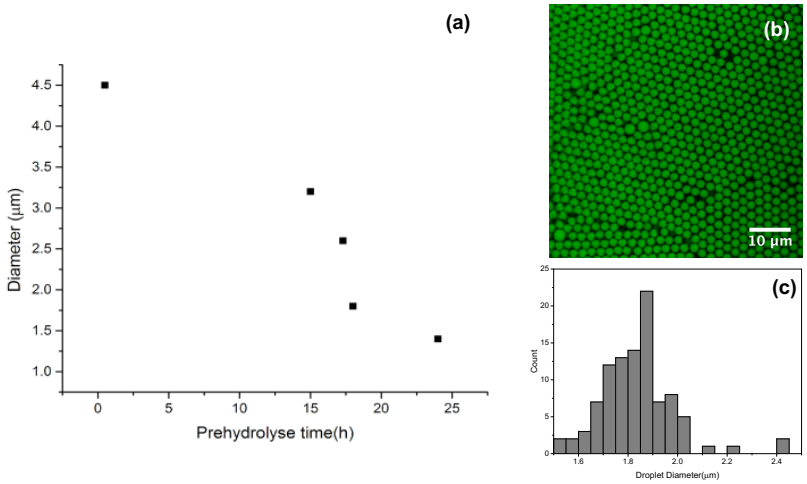

Fig. 2.1 (a)Droplet diameter decreases with increasing prehydrolysing time of DMDES monomers. (b) A confocal image of emulsions with prehydrolysing time of 18 h. (c) Size distribution of droplets in (b).

Emulsions synthesised by prehydrolysing DMDES monomers also have low polydispersity. Fig.2.1(b) is a confocal image of an emulsion sample with prehydrolysing time of 18 h where droplets start to crystallise due to low polydispersity. After measuring the size of droplets in ImageJ, the size distribution was plotted, as shown in Fig. 2.1(c). The mean size of the droplets is 1.84 μm and the polydispersity is 8.2%. Such monodisperse colloidal emulsions have great potential for structure and dynamics studies of soft matter at single particle-resolved level.

2.2 Principle of confocal microscopy

Confocal microscope was first built by Marvin Minsky in 1955. It has been widely used in biological sciences thanks to the non-destructive way of tracking molecules and structures of fluorescence technique and its ability to give 3 dimensional visualisation of the sample . The application in colloidal science was first performed by Yoshida *et al* in 1991[72], who observed hexagonal packing of charged polystyrene latex colloids in 3D. The advantage of visualising colloids in 3D combined with accurate particle tracking, confocal microscopy gives the chance to advance our knowledge in colloidal phenomena.

Fluorescence microscopy and bright-field microscopy are two common types of optical microscopy used in studying substances that are not accessible to human eyes. They utilise fluorescence techniques and white light to illuminate samples respectively and both generate 2D images of the sample because the out-of-focus signals from different height of the sample cannot be distinguished which also reduce the resolution of the microscope. Based on fluorescence microscope, a spatial pinhole is added inside confocal microscope before the detector, as shown in Fig. 2.2, to reject out-of-focus signals emitted from the sample, and thus improve the resolution and have the ability to obtain 3D images.

A confocal laser scanning microscopy (CLSM) works as shown in Figs. 2.2. A laser with certain wavelength is firstly focused at the excitation aperture which produces point illumination. The excitation laser is then reflected by the dichroic mirror, passes the objective lens and reaches the sample. Due to the point illumination, only a small part of the fluorescently labelled sample (point) is excited by the laser, and emit signals with longer wavelength. The emitted fluorescence passes the same objective lens and dichroic mirror, before reaching the signal detector, the pinhole will reject out-of-focus signals from different depth of the sample, and only signals in the focused plane can reach the detector.

Therefore, the pinhole size affects the resolution and intensity of the image. Small pinhole only accepts signals strictly close to the focused plane, this on one side increases the resolution, but on the other side the image will become dark because only very few signals are accepted. This can be improved by increasing the exposure time, so that there is more time to detect fluorophores from the sample, or increase the intensity of excitation laser but lower than the fluorophore photobleaching limit, or using a more sensitive detector.

In confocal microscopy, the detectors are usually photomultiplier tubes (PMTs). The detectors transform the emitted light signals to current and multiply the current as much as 100 million times, and then recorded by the computer. Confocal microscope scans only one point in the specimen at a time, to obtain a 2D rectangular image, the position of laser point is changed by oscillating mirrors. A 3D image is generated by stacking a series of 2D

images which are acquired at different horizontal planes, the z position of the image can be controlled by the sample stage.

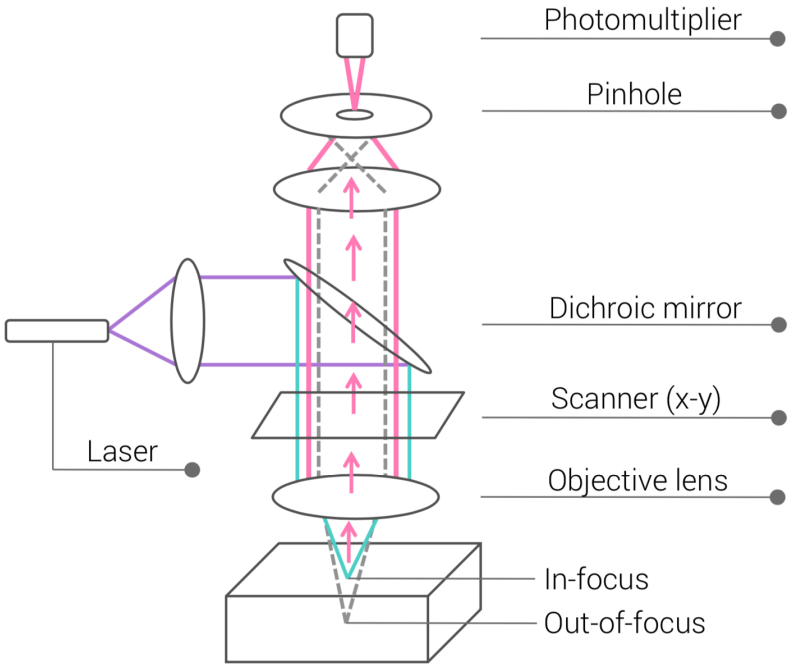

Fig. 2.2 Schematic of confocal laser scanning microscopy (CLSM).

2.2.1 Stimulated Emission Depletion (STED) microscopy

Stimulated emission depletion microscopy (STED) was developed by Stefan W. Hell in 1994, he was awarded the Nobel Prize in Chemistry in 2014 for the STED development[73, 74].

In conventional confocal microscopy, when the excitation laser hits the fluorophore, an electron in the fluorophore molecule is excited from the ground state to a higher energy electronic state. The electron will then relax back to the vibrational energy level of the ground state, and emits a photon, which will be detected as fluorescent signals.

However STED applies a second laser beam to the fluorophore, before the excited electron relaxes back to the ground state, so that the excited electron will relax to a higher vibrational energy level of the ground state compared with only one excitation laser. The reduction of the energy difference between the two electronic states leads to a red shift of the wavelength of the emitted photon. Since the wavelength of depleted photons is at the red end of the spectrum, only the undepleted electrons will be detected.

As shown in Fig. 2.3 (middle), the first excitation laser has a Gaussian point spread function (PSF), the width of which decides the resolution of conventional confocal microscopy.

The stimulated beam which has a donut shape applied in STED (Fig. 2.3 left), depletes the photons in this area, therefore only photons inside both the Gaussian PSF and middle of the donut (Fig. 2.3 right), which are dramatically less than the original photons inside the Gaussian beam, will be detected by the detector. By applying the stimulated depletion laser, the lateral resolution of STED microscopy can reach 30 nm, makes STED one of the super-resolution microscopy and nanoscopy.

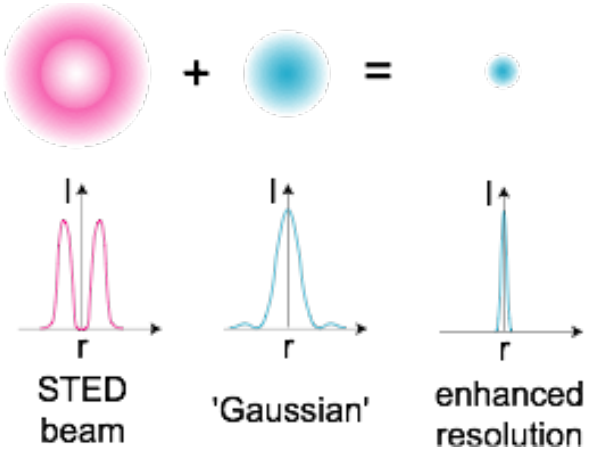

Fig. 2.3 Additional to the only Gaussian beam (middle blue) applied in conventional confocal microscopy, STED microscopy implements a second beam with donut shape (left pink). Fluorophores inside the donut shape will be depleted, resulting in a much sharper beam (right blue) and enhancing the resolution[73, 74].

2.3 Microscopic contact force model

When droplets deform under compression, as shown in the schematic in Fig. 2.4 the deformation is small with respect to the droplet surface area, therefore the Laplace pressure can be considered unchanged during the deformation. All the energy from the compression is presumed to be stored as elastic energy in the deformation area, at microscopic level, the interdroplet forces between two droplets with radii of R_1 and R_2 can be described by Princen force law[2]:

$$f = \frac{\sigma}{\tilde{R}} A \tag{2.1}$$

where A is the deformation area at contact, $\tilde{R}$ is the geometrical mean radius of the two undeformed droplets, $\tilde{R} = R_1 R_2/(R_1 + R_2)$, σ is the interfacial tension, which is taken as 9.2 mN/m between silicone oil and water-glycerol mixture, measured by Brujic with a similar system[76]. This force model has been applied to various systems to measure microscopic

forces, such as athermal emulsions[76], and liquid droplets labelled with a monolayer of fluorescent nanoparticles or modified cowpea mosaic virus (CPMV)[78].

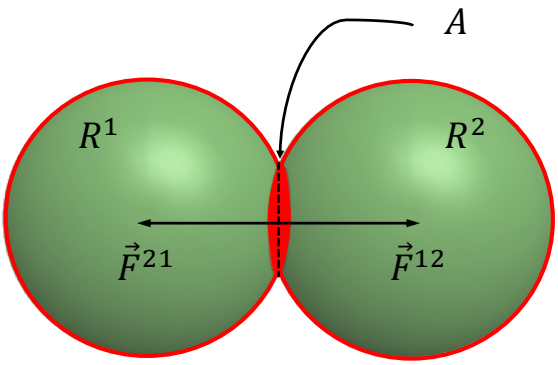

Fig. 2.4 Schematic of interdroplet contact forces. Different colours of oil droplets and interfaces indicate that Fluorescent emissions from droplets and interfaces are at different wavelengths and detected separately by two HyD detectors. Because interdroplet contacts have higher fluorescent intensities compared with oil droplets and other interfaces, the contact area A can be obtained after thresholding. Interdroplet forces are then calculated using Princen force model[2, 76].

In equation 2.1, the interfacial tension σ is a constant for a given experimental system and is known. In order to calculate contact forces, we need to know the contact area A and radii R_1 and R_2 of the two contacting droplets. From a 3D confocal image of emulsion, we obtain the position and size of droplets using a particle tracking method which is described in section 2.5. As for the contact area A, first we take advantage of a solvatochromic dye, Nile Red, for the emulsion, which helps identify the contact area in a confocal image. The mechanism of Nile Red is explained in section 2.4. The tracking of contacts is more complicated than tracking of particles, due to the small area of contacts and intensity variation. A detailed tracking of contacts method is described in section 2.6

2.4 Solvatochromic fluorescent technique

The fluorescent label employed to visualise interdroplet contacts is Nile Red dye. The chemical structure of Nile Red is shown in the inset of Fig. 2.5. Due to the hydrophobicity of the dye, it is often used for labelling lipids or oil droplets. The main feature of Nile Red utilised in our system is the solvatochromic property. The molecule itself is not charged, however due to a large group of electron conjugation in the structure, it can become surface active from the induced polarity. Depending on the dielectric constant and hydrogen bonding capacity of the environment, the energy gap which is determined by the electronic ground

stated and excited state will change, therefore Nile Red is very sensitive to the polarity of the solvents. Both the absorption and emission can shift when the solvent polarity varies[75].

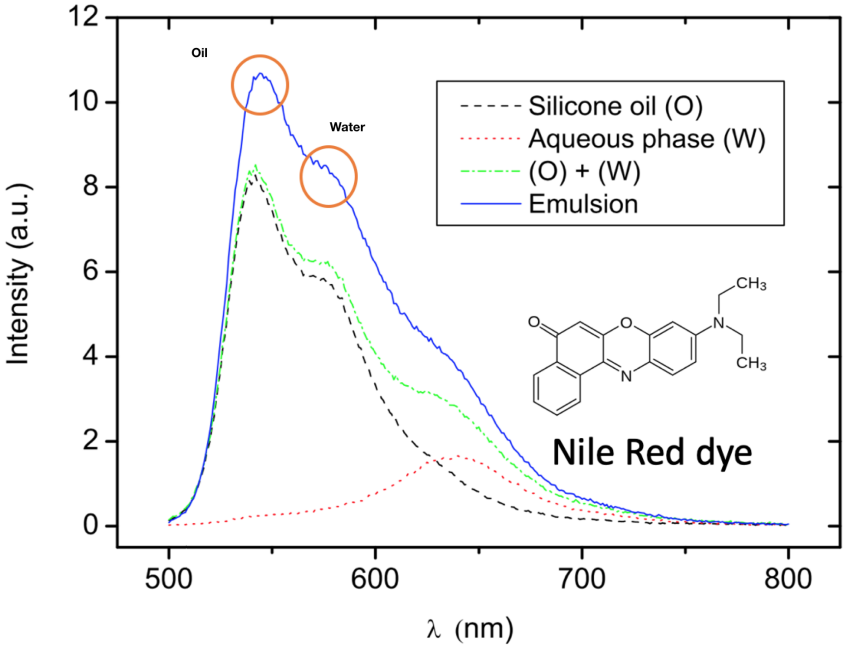

Fig. 2.5 Emission spectra of silicone oil emulsions fluorescently labelled with Nile Red dye and stabilised with sodium dodecyl sulfate (SDS) surfactants. The inset shows the chemical structure of Nile Red molecule [76] .

In a polar solvent such as water, Nile Red is almost non-fluorescent. As the polarity decreases, the fluorescence becomes stronger and also has blue shifts. In our emulsions of silicone oil in the mixture of water and glycerol, Nile Red will primarily stay inside silicone oil droplets and make the droplets fluorescent while the aqueous being non-fluorescent[77]. However, since the dye has surface active property, it will also be spreaded on the oil and water interfaces just like surfactants. The dye molecules at the interface experience higher environment polarity, compared with those inside silicone oil droplets, thus they emit fluorescence with a longer wavelength.

The emission spectra of the silicone oil emulsion system, stabilised with sodium dodecyl sulfate (SDS) surfactant, have been measured and shown in the blue curve in Fig. 2.5[76]. It is clearly shown that there are two emission peaks at different wavelengths and with different intensities. Fluorescence from bulk oil droplets has higher intensity and at shorter wavelength (the first peak in the blue curve). The absorption has also been measured, and it has the same trend as the emission depending on the environment polarity[76].

By using two detectors with different ranges of wavelengths in confocal microscopy, fluorescent signals from oil droplets and oil-water interfaces can be detected separately and

simultaneously. In the schematic of two contacting droplets, as shown in Fig. 2.4, the green colour for oil droplets and red colour for oil-water interfaces indicate that fluorescent signals are detected at different wavelengths by two HyD detectors. When two droplets are in contact, droplets are slightly deformed resulting in a deformation area A. Because of the deformation, fluorophores at both droplet surfaces are accumulated at the deformation area, leading to the increase of local fluorophore density. As a result, the contact area in the confocal image of emulsions shows higher fluorescent intensity than the rest part of the image. We therefore can obtain the size of contact area A by applying an intensity threshold to the confocal image, a detailed method of the image processing method is described in section 2.6.

From Fig. 2.5, we observe that the positions of two peaks are around 545 nm and 645 nm. The values of absorption peaks are at 488 nm and 568 nm respectively[76]. This is the case when emulsions are stabilised with SDS. In order to dissolve more Nile Red at interfaces and obtain higher fluorescent signals, we change the surfactant to sodium dodecylbenzene-sulfonate (SDBS) which has one more benzene molecule between the hydrocarbon chain and anionic group. We did not measure the absorption and emission spectra, but we find the range of maximum intensity is different by using STED microscopy. When the emulsion droplets are stabilised with SDBS, the excitation wavelengths are 514 nm for the oil signals and 580 nm for the interface signals, the detection ranges become 520-575 nm and 585-640 nm respectively. This shows clear red shifts when the surfactants are changed from SDS to SDBS. We further change the solvent to water and ethylene glycol mixture, which is also index matched with silicone oil droplets, but we can barely observe difference of fluorescent signals between oil and interfaces. Therefore a considerate choice of chemical combinations is crucial to visualise contacts.

Nile Red molecules do not dissolve in pure water, however if there is presence of surfactant molecules or micelles, Nile Red can be trapped inside surfactant micelles and then are fluorescent in water[76]. Hence the concentration of surfactants will affect the contrast of confocal images. When the surfactant concentration is above the CMC value, there are a large number of micelles dispersed in the aqueous phase, dye molecules tend to migrate from oil droplets and interfaces to the aqueous phase, this process therefore lowers the desired fluorescent signals. In the meantime, the background of aqueous phase will also be fluorescent, and dramatically reduce the intensity contrast.

Nile Red only work for limited emulsion systems to detect interdroplet contacts. The combination of Nile Red and the most common colloidal model systems of PMMA and silica particles does not give the contact information. Suhina and Chantal and co-authors synthesised solvatochromic probes which can attach to functionalised silica and PMMA particle surfaces, performing similarly as Nile Red in emulsions. These fluorescent probes

are very useful to study systems with frictional forces, forces when particles are buckled or at jammed state[79, 75, 80].

2.5 Particle tracking methods

Particle centres and radii of emulsion droplets were detected using colloids tracking package which was developed by Leocmach[81]. The method takes advantage of algorithm of Scale Invariant Feature Transform (SIFT) which is often used in the field of computer vision to match common features across different images. In colloids tracking algorithm, experimental images are blurred using two Gaussian filters with different kernels s and $s\prime$, and result in two blurred images G_s and $G_{s\prime}$. The difference of Gaussians (DoG) is defined as $DoG = G_s - G_{s\prime}$. Bright pixels which are normally in the centres of particles will be local minima in the response function of DoG. The difference between two Gaussian kernels $k = s - s\prime$ is set as an input parameter by the user. Once the k is fixed, a series of kernels s and $s\prime$ are applied to experimental images. With small Gaussian kernels, the positions of small particles will have clear minima in the image of DoG, while the regions where larger particles stay are not completely blurred so that no obvious minima appear in DoG, as a result the positions of smaller particles can be detected. As the kernel size increases, positions of larger particles will be identified.

The application of Gaussian kernels with various sizes makes it possible to track polydisperse spheres, which is not achievable in many other particle tracking methods, such as the first colloidal particle tracking algorithm developed by Crocker and Grier[82]. Their method requires samples with monodisperse particles, an estimated radius of particles is also needed in order to determine particle centres. The algorithm searches through the image for bright pixels within area that is defined by the estimated particle radius, which is similar to applying a maximum filter. This will lead to a new filtered image with blobs having maximum intensity around the size of input particles, and the brightest pixel is identified as the centre of a particle. All the blobs have similar sizes, therefore sizes of polydisperse particles can not be well determined.

Although by using colloids tracking method it yields suggestive sizes of particles, the sizes are not true particle sizes and only scale with original particle sizes. In order to have better determination of particle sizes, pair correlation function $g(r)$ of colloidal gels or dense suspensions are plotted based on particle centres. Within a certain polydispersity (less than 8%, samples can be considered monodisperse), the position of the first peak of $g(r)$ indicates the mean particle diameter of the sample. A scale factor of particle radius is calculated as the ratio of the first peak of $g(r)$ and the mean size of particles obtained from particle tracking.

We find good agreement with confocal images when multiplying the size factor to tracked particle radii.

2.6 Tracking of interparticle contacts

In a number of literatures of tracking contacts such as Brujic *et al*[3], they applied an intensity threshold to the contact image, after which they can directly track the image residuals which are the particle contacts. This is possible when particles in the system are large enough and droplet deformations are not significant, this means all contacts on a particle are well separated after the thresholding. However when the size of droplets is reduced considerably to colloidal scale, the small size of particles and resolution limitation of the microscope make it infeasible to track contacts with only one thresholding. Therefore a method was developed in this thesis to effectively segregate connected contacts, determine centres and sizes of contacts.

2.6.1 Histogram equalisation

Because the refractive index matching between emulsion droplets and aqueous phase is not perfect, there is more scattering of the laser as the laser travels deeper in the sample, and this leads to dimmer images where the sample is far from the microscope lens. Since the method to obtain contact area size is strongly dependent on the intensity of the image, the equalisation of intensity in z direction is desired.

A target xy slice is selected as a template, other slices of images are adjusted in order to match the histogram of the target slice. For each xy slice of the 3D confocal image, the number of pixels with intensity i in grey level is n_i, the probability of a pixel with level $4i$ in the image is

$$p(i) = \frac{n_i}{n}, \quad 0 \leq i < I_{max} \tag{2.2}$$

where I_{max} is the maximum value of intensity in grey scale which is typically 255, n is the total number of pixels in the xy image, which is 512×512. From the intensity histogram of each 2D image $p(i)$, we can calculate the accumulated normalised histogram which is called cumulative distribution function (cdf),

$$cdf(i) = \sum_{j=0}^{i} p(j). \tag{2.3}$$

For the target slice and one source slice, we can calculate their cumulative distribution function (cdf), using the method described above[83]. Then we interpolate linearly in order to find the pixel values in the target slice that correspond most closely to the values in cdf in the source image. This returns a new image which is histogram equalised with the target image and is based on the source image. We perform this equalisation for all xy slices of a 3D confocal stack image. One xz slice of a confocal image is shown in Fig. 2.6 (a), where we can see intensity inhomogeneity in z direction, the intensity profile along z is also plotted in Fig. 2.6 (c) (the blue curve). After the histogram equalisation, the intensity is uniform through the sample, as can be seen from the orange curve in Fig. 2.6 (c) and also the xz image in Fig. 2.6 (b).

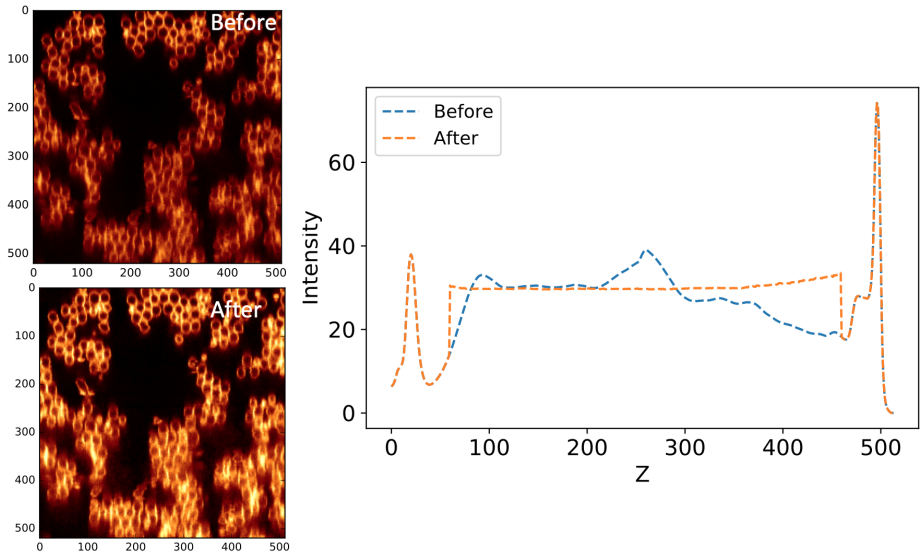

Fig. 2.6 (a) A confocal microscopy image of an emulsion gel in xz direction. (b) The same image after histogram equalisation. (c) Distribution of average intensity in each xy plane of the emulsion gel, before and after histogram equalisation.

2.6.2 Weighted middle points between particles

In order to separate connected contacts, the strategy is to manually add a spatial boundary to each contact. The first step is to find the weighted middle points between a reference particle and its neighbours, which are possible locations of contact centres. To determine the weighted middle points M_{ij} between two neighbouring particles P_i and P_j, first M_{ij} needs to be located on the line P_iP_j and the distances between M_{ij} and two neighbouring particles d_i and d_j are proportional to particle radii, *i.e.* $d_i/d_j = R_i/R_j$. Therefore a binary mask of

the same size (pixels) of the contact image is built, where the positions of weighted middle points M_{ij} have value of 1 while the rest of the mask is 0.

2.6.3 Position blobs on middle points

Based on centres of middle points, nearly spherical blobs were created by dilating a binary kernel in three dimensions. The blobs were constructed as big as possible but without overlapping with each other, this yields a maximum blob size which is 263 pixels in volume. The purpose of building blobs is trying to contain true contacts as much as possible and build an upper boundary for the contacts to separate them from each other if they are overlapping after the thresholding. Because blobs are created in between neighbours (particles are not necessarily in contact), so the number of blobs generated are greater than the number of true contacts.

Screen out connected blobs

After initial placement of blobs, it is inevitable to avoid blobs that are connected when we try to maximise the size of blobs, as shown in Fig 2.7(a). By looking at the distribution of blob volumes, it is clear that connected blobs have noticeable larger volumes than segregated blobs, the binary mask with all blobs was separated into two masks: a connected blob mask and a well separated blob mask, as shown in Fig 2.7(b) and (c). In the mask with connected blobs, we eroded the mask in order to separate these blobs and resulted in Fig 2.7(d). Next, the eroded mask (Fig 2.7(d)) and non-connected blob mask (Fig 2.7(c)) were combined into a final binary mask (Fig 2.7(e)). This mask effectively sets spacial bounds for contacts and can be used to segregate connected contacts.

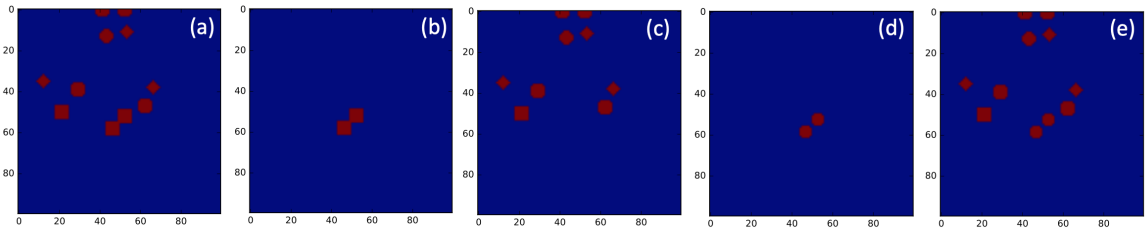

Fig. 2.7 Binary masks with blobs based on the weighted middle points between neighbouring particles. (a) All drawn blobs, which are generated by dilating kernels at middle points. (b) Connected blobs and (c) well separated blobs in (a). (d) Mask (b) after erosion. (e) Final binary mask with combination of (c) and (d). Numbers on axes represent pixels, all images are small part of the confocal image.

2.6.4 Thresholding contact images

The mechanism of force detection from confocal images is based on the fact that contact area has higher fluorescent intensity than the rest of the image. To distinguish contact area from the bulk droplets and the aqueous background, an intensity threshold is required to apply to the image. In order to generate the threshold value systematically and without bias, the Otsu thresholding method was employed. Analysis of contact images was performed using the function of SKIMAGE.FILTERS.THRESHOLD_OTSU in Python, and the principle is explained below[84].

When applying one testing threshold to the image, pixels have lower intensity than the threshold fall into the background class, while the other pixels are considered as foreground (binary image). The weight of each class (W_b and W_f) is determined by the number of pixels in the class divided by the total number of pixels of the image. Within each class, the mean (μ_b and μ_f) and variance (σ_b and σ_f) of intensity are calculated. The sum of two variances multiplied by their weight ($\sigma_W = W_b\sigma_b^2 + W_f\sigma_f^2$), which is called 'Within-Class Variance', tells the spread of background and foreground. In Otsu algorithm, all possible threshold values are applied to the image, the value that gives minimum variance of background and foreground is considered Otsu threshold.

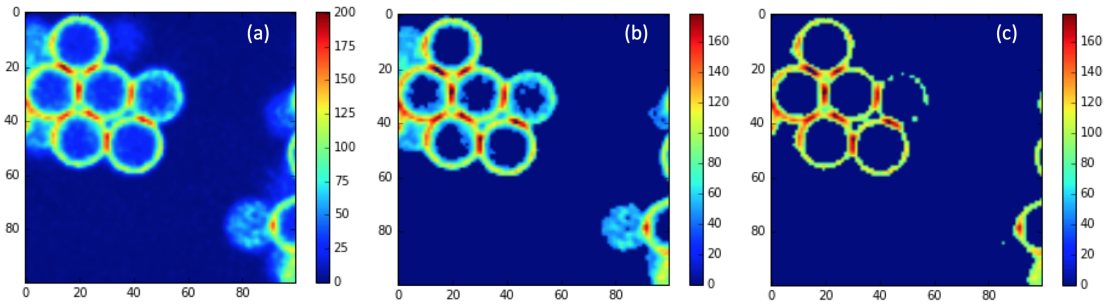

Fig. 2.8 An example of application of Otsu threshold. (a) A small part of the original contact image. (b) The image after first Otsu threshold (40). (c) The image after second Otsu threshold (76). Numbers on axes represent pixels, colour bars represent intensities

Otsu threshold can only divide an image into background and foreground, therefore the algorithm is applied twice in the contact image to effectively isolate contact area. The first Otsu threshold distinguishes droplets (with contacts) from aqueous background. The second value separates contacts (foreground) from bulk droplets (background), as shown in Fig 2.8. The exact values vary on different samples.

2.6.5 Edge enhancement

The aim of applying Otsu threshold is to only keep high intensity contacts remaining in the image. However, it is possible that other parts of the image, the middle of the droplet for instance, would also remain after applying the second Otsu threshold. This will lead to the detection of contacts that are in the centre of droplets, which are not feasible. To resolve this issue, another mask is desired to remove the residuals inside droplets. Sobel filter which is commonly used for edge detection can clearly define the interfaces of droplets and therefore improve the accuracy of the detection of contacts.

The Sobel filter identifies a sharp intensity change *i.e.* intensity gradient, in the image by calculating the approximate first derivatives of the image in X and Y directions separately. Sobel operators are two kernels of 3 by 3 matrices for calculating derivatives. The original image with intensity of $I(x,y)$ is convolved with Sobel operators, and this gives the derivatives of the image G_x and G_y, as shown in equations below.

$$G_x = \begin{pmatrix} 1 & 0 & -1 \\ 2 & 0 & -2 \\ 1 & 0 & -1 \end{pmatrix} * I(x,y) \tag{2.4}$$

$$G_y = \begin{pmatrix} 1 & 2 & 1 \\ 0 & 0 & 0 \\ -1 & -2 & -1 \end{pmatrix} * I(x,y) \tag{2.5}$$

The magnitude of gradient is calculated combing these two derivatives in equation 2.6.

$$G = \sqrt{G_x^2 + G_y^2} \tag{2.6}$$

The result of directly applying the Sobel filter to the particle image is shown in Fig. 2.9(b). The edges between colloid-rich and colloid-poor phases are clearly detected. However, inside the colloid-rich phase, edges of each particle are not well defined because some particles are in contact, due to the high number density of particles inside colloid-rich phase. Therefore we need a mask which contains spheres that well separated in order to detect their edges. Since the centres of droplets are obtained by multi-scale colloid tracking method, we can construct a binary image of the particle image as shown in Fig. 2.9(c). Then the Sobel filter is applied to the binary particle image, this resulted in Fig. 2.9(d) which shows the edge of each particle in the gel.

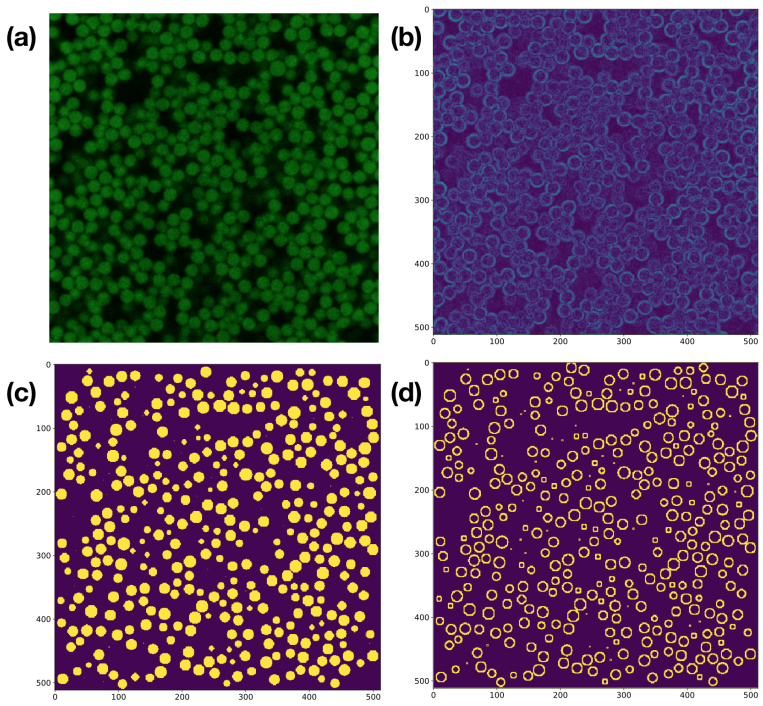

Fig. 2.9 (a) Confocal image of particles in a colloidal gel. (b) Sobel filter image of confocal image (a). (c) Binary image from tracked particle positions. (d) Sobel filter image of the binary image (c).

2.6.6 Centres and sizes of contacts

Three masks are generated in order to correctly detect the positions and sizes of contacts, as indicated in Fig. 2.10. The first mask, Fig. 2.10(a), is the binary mask of spheres that are placed between particles. This mask can effectively segregate some contacts that are connected after thresholding the contact image. It is possible that some pixels which are located in the middle of particles remain after the thresholding. Therefore a second mask, Fig. 2.10(b), which contains edges of all particles is desired, in order to set constraints to contact positions. This means contacts can only be located at edges of particles but not inside particles. The third mask (Fig. 2.10(c)) is the thresholded contact image, which is obtained by applying Otsu threshold to the confocal image of contacts. By convolving these three masks, the remaining pixels are the contacts between droplets, as shown in Fig. 2.10(d).

Each contact is then labelled with an index, by counting the number of pixels in each contact it gives the volume of the contact. The contact centre is determined by finding the geometrical centre or maximum intensity pixel in the contact. The size of contacts is proportional to the interdroplet contact forces, and it is the main component to find contact force distributions, force chains in colloidal gels or dense suspensions.

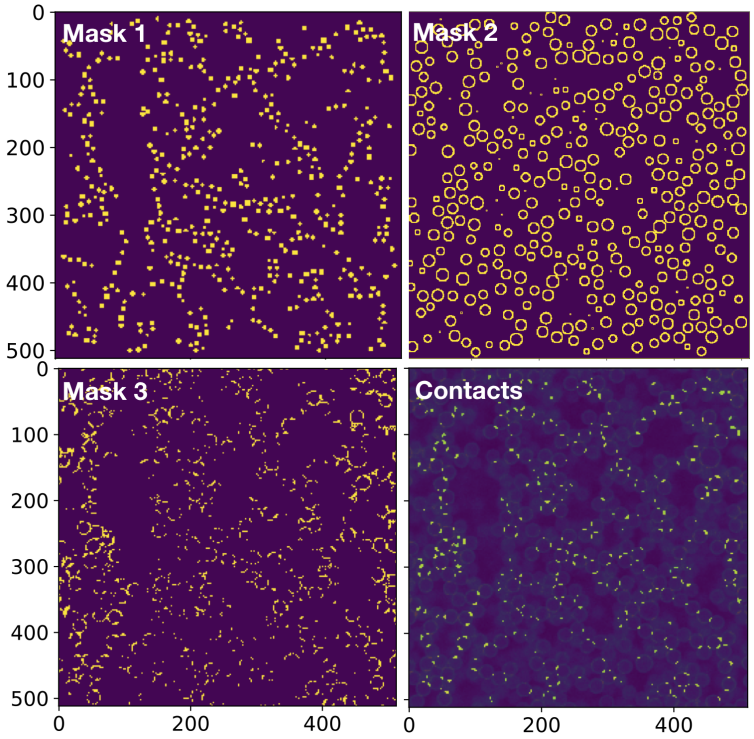

Fig. 2.10 (a) A binary mask of spheres placed between particles, which is generated for separating contacts that are connected spatially, due to the limit of microscope resolution. (b) A binary mask of droplet edges. (c) A binary mask of potential interdroplet contacts. The mask is obtained by applying Ostu threshold twice on a confocal image. (d) A binary image of only interdroplet contacts which is the result of the convolution of mask (a), (b) and (c). The size and position of contacts are obtained by labelling each individual contact from this binary image.

2.6.7 Allocate contacts to particles

After particle and contact tracking, both coordinates and sizes are obtained. The coordinates of particles and contacts are $\boldsymbol{p}_i$ and $\boldsymbol{c}_j$ respectively. The distances between each particle and contact are computed, and stored in a $i \times j$ 2D matrix d_{ij}.

$$\boldsymbol{d}_{ij} = \{i \in N_p, j \in N_c \mid\mid \boldsymbol{p}_i - \boldsymbol{c}_j \mid\} \tag{2.7}$$

where N_p and N_c are the number of particles and contacts respectively. For a contact $\boldsymbol{c}_j$, the closest two particles $\boldsymbol{p}_a$ and $\boldsymbol{p}_b$ are detected by searching for the first two minimum values d_{aj} and d_{bj} in $\boldsymbol{d}_{ij}$. These two particles are in contact through the contact area $\boldsymbol{c}_j$. For each contact, we find two neighbour particles, in turn we can determine neighbour contacts for each particle, and this gives the contact number Z.

2.7 Stress computation

For a reference particle $\boldsymbol{p}_0$, for example, there are three particles $\boldsymbol{p}_1$, $\boldsymbol{p}_2$ and $\boldsymbol{p}_3$ that are in contact with particle $\boldsymbol{p}_0$, through contacts $\boldsymbol{c}_1$, $\boldsymbol{c}_2$ and $\boldsymbol{c}_3$, as shown in Fig. 2.11. The compressive force from particle $\boldsymbol{p}_1$ is $\boldsymbol{f}^1$, with magnitude of f^1, which is determined from the size of contact c^1. The stress tensor σ_{ij} of a particle is calculated by summing stress contributions from each contact particle, on all element axes, indicated in equation 2.8.

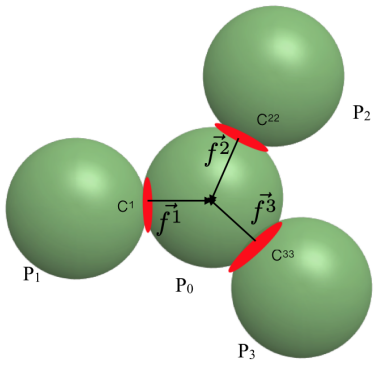

Fig. 2.11 Schematic of stress tensor calculations.

$$\sigma_{ij} = \frac{1}{V} \sum_{c=1}^{N^c} \boldsymbol{f}_i^c \boldsymbol{r}_j^c \tag{2.8}$$

where $\boldsymbol{r}^c = \boldsymbol{c}_c - \boldsymbol{p}_0$, $\boldsymbol{r}^c$ is the vector from the centre of the particle $\boldsymbol{p}_0$ to the centre of contact $\boldsymbol{c}_c$, i, j are the coordinate axes x, y, z of a Cartesian coordinate system, and V is the

volume of the reference particle, N^c is the number of neighbours of the reference particle $\boldsymbol{p}_0$. For each particle, we obtain a stress tensor σ_{ij} with nine components as presented in below.

$$\sigma_{ij} = \begin{bmatrix} \sigma_{xx} & \sigma_{xy} & \sigma_{xz} \\ \sigma_{xy} & \sigma_{yy} & \sigma_{yz} \\ \sigma_{xz} & \sigma_{zy} & \sigma_{zz} \end{bmatrix} \tag{2.9}$$

The diagonalisation of the stress tensor generate three eigenvalues and eigenvectors of the matrix, which represent principal stresses and principal directions respectively. The principal stresses and principal directions characterise the stress at a point and are independent of the orientation. A coordinate system with axes oriented to the principal directions implies that the normal stresses are the principal stresses and the stress tensor is represented by a diagonal matrix.

$$\sigma_{ij} = \begin{bmatrix} \sigma_x & 0 & 0 \\ 0 & \sigma_y & 0 \\ 0 & 0 & \sigma_z \end{bmatrix} \tag{2.10}$$

With the tension-positive convention, the most negative the eigenvalue, $(\sigma_x, \sigma_y, \sigma_z)_{min}$ is the minor principal stress which is the most compressive stress, while the maximum value of the eigenvalue $(\sigma_x, \sigma_y, \sigma_z)_{max}$ is the major principal stress. Since the microscopic forces measured here are only compressive forces, therefore the most compressive stress is a relevant property to characterise the system. The sum of all three principal stresses is the stress trace $tr(\sigma_{ij})$ of the stress tensor, which is also the local pressure for a droplet.

$$tr(\sigma_{ij}) = \sigma_x + \sigma_y + \sigma_z \tag{2.11}$$

2.7.1 Force chain determination

Once we obtain the information of stresses on each particle, combining the positions of particles, we can characterise how forces are transmitted from one particle to another when they are in contact, *i.e.* through force chains.

The emergency of percolated force chains have been accounted for one of the signatures of the jamming transition.Percolated force chains along with minimum number of isostatic contacts make sure stresses are able to thoroughly transmit through the system and remain mechanically stable. Hence, the identification of force chains not only tells the pattern of stress transmission of the system, but also gives information of the mechanical stability.

The concept of force chains is not completely unified, but one plausible definition is a quasilinear assemble of at least three particles where stress is concentrated[85]. Based on this

definition, a quantitative method was created by Peters *et al*[85]. The first requirement is that particles in a force chain should carry large stresses. They choose the minor principal stresses as the particle property, if the minor principal stress of a particle is larger than the average compressive stress in the system, these particles are taken account for candidates making up force chains. This method has been applied to a simulated jammed configuration with an external force constantly pressing the system[85]. However in our experiments, we consider the intensity threshold applied to the image with contacts is performing in the same way as the threshold of average compressive stress. Thus contacts remained after the intensity threshold are recognised as high stresses in the sample.

After selecting these particles with large stresses, the algorithm should satisfy the second criteria: these particles with concentrated stresses should be quasilinear spatially, allowing only small amounts of rotation. The searching algorithm is explained using the schematic as shown in Fig .2.12.

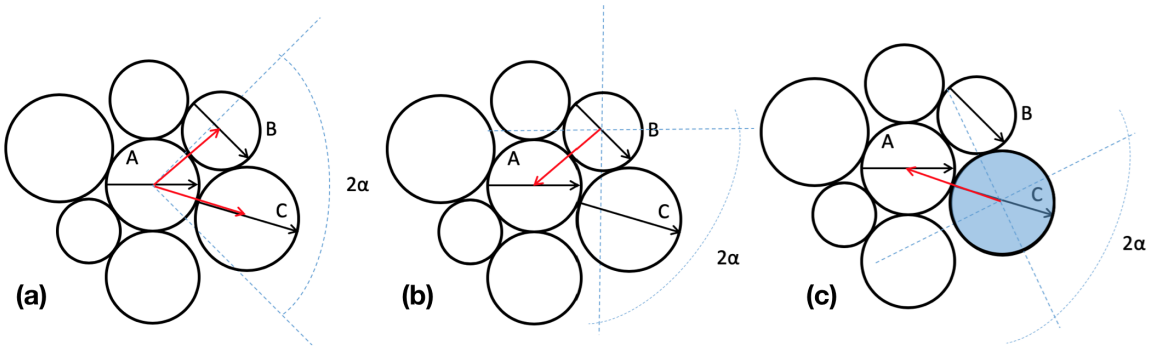

Fig. 2.12 Schematic of force chain determination method[85].

The black arrows represent the direction of stress of the particle, red arrows are vectors connecting two particle centres, the blue dashed lines show the region in which satisfy the angle range. As shown in Fig. 2.12(a), given a reference particle A, from the centre of particle A, we define a region that deviates of an angle of $\alpha(\pm\alpha)$ from the direction of the stress σ_A, as indicated by the blue dashed lines. The value of α determines the linearity of force chains, with $\alpha = 0$, the constraint only allows for a perfect linear chain; with $\alpha = \frac{\pi}{2}$, are particles that are in contact will be considered in the chains. From Fig.2.12(a), we find that particle B and C are within the angle region, because vectors $\vec{AB}$ and $\vec{AC}$ are within this region. Therefore they are considered candidate particles in a force chain for the reference particle A, but we also need to check if particle A qualifies as a candidate for particle B and C.

In Fig. 2.12(b), from the centre of particle B and based on the stress on σ_B, we also define a angle region indicated by the blue dashed lines using the same value of α. We can clearly

see that the vector $\vec{BA}$ does not lie in this region. Therefore particle A is not a force chain candidate particle for particle B, and they do not form a force chain. Candidate particle C is also checked in the same way, and we find $\vec{CA}$ falls in the blue dashed line region, therefore particle A is a force chain candidate particle for particle C and we say they are in the same force chain.

Since a reference particle is picked up randomly, so it can be in the middle of a force chain. In order to fully search force chain particles lie in both sides of the reference particle, when the searching from on direction reaches the end of the force chain particle, we will set the end particle as the reference particle, and search backwards till the other end of the force chain.

The angle α is chosen as $\frac{\pi}{4}$ in this work and this allows for some deviation from a perfect linear chain. Using this method, we can identify which particles form force chains, characterise the length and distribution of force chains in our system. This analysis provides information and bridge the gap between the macroscopic mechanical response and microscopic structures of force networks.

Chapter 3

Microfluidic Emulsification by Noland Optical Adhesive Devices

Author contributions: the contents of the chapter were based on a published article: M. Meissner, J. Dong, J. Eggers, A. M. Seddon and C. P. Royall. *Soft Matter*. 13, 788 (2017). In this paper, J. Dong produced and collected colloidal emulsions, imaged and tracked coordinates of dense emulsions. M. Meissner performed measurements on viscosity and flow rate ratios, and structural analysis on tracked coordinates, and wrote the manuscript.

3.1 Introduction

The vast majority of work on colloidal systems concerns itself either with the study of solid particles, for example solid colloidal spheres, or with emulsions, where an oil phase is dispersed in an aqueous medium or vice versa[86]. For solid colloidal spheres, unsurprisingly, the ratio of particle viscosity to the suspending fluid viscosity, $\lambda = \eta_o/\eta_i$, will tend towards infinity. On the other hand emulsions are much "softer" with viscosity ratios λ much closer to 1. This allows emulsion droplets to function as exciting new colloidal model systems. For example, emulsion droplets have negligible friction at their surfaces with intriguing consequences for the jamming-glass crossover [7, 87], alternatively, the ease of adsorption of lipids or polymers onto droplets opens new and exciting directions in self-assembly[88–90, 6, 91].

Emulsions, with their multitude of food, care product, and petrochemical applications [92, 93], are a system of great scientific and industrial interest, and so it should come as no surprise that the formation of emulsions is a well explored field with a huge range of emulsification techniques available. These methods include such techniques as mechanical milling, blending,

high pressure homogenisation, or shear mixing. While powerful, these techniques tend to produce large emulsion droplets, or emulsions with a broad size distribution. Microemulsions on the other hand, while extremely versatile due to their self assembly behaviour, have sizes in the range of 10-100 nm, and are thereby far too small for real space imaging and coordinate tracking [94]. An emulsion that combines the best of both worlds possessing both an average droplet size in the range of a few microns, with a narrow size distribution, would open up a wide range of new possibilities.

An alternative to the aforementioned methods is microchannel emulsification, a versatile technique where two or more distinct fluid phases are flowed through a microscale channel and interfacial stresses are induced to generate droplets with very narrow size distributions [95]. Currently microfluidic emulsification techniques remain focussed primarily on the formation of water-in-oil emulsions, usually with the viscosity ratio λ below 1.

In order to develop the desired colloidal model system we must first consider the behaviour of a droplet in solution using the Peclet number $Pe = \tau_B/\tau_{\text{sed}}$, where τ_B is the particle Brownian time, τ_{sed} is the time particle sediment to the distance of one particle diameter. A Peclet number of around one is generally seen as the dividing line between a colloidal system and an athermal granular system [27]. As the Peclet number scales with both particle diameter and buoyant mass a colloidal emulsion can be achieved either by producing droplets of a sufficiently small diameter or by using liquids with suitably similar densities [96]. As such, it is vital that a microfluidic system for the production of colloidal oil-in-water emulsions is capable of both producing droplets which are suitably small and uniform, but also to be solvent-compatible enough to produce emulsions from a range of component materials.

Microfluidic droplet generation can be realised with three types of device: T-Junction devices where a slug of the dispersed phase is extruded into a flowing fluid until the dispersed phase fluid breaks up into droplets[51], co-flowing devices where an outer continuous phase fluid flows parallel to and surrounding an inner dispersed phase fluid until droplet generation occurs via stretching of the interface between the two fluids [97], and flow-focusing devices, where co-flowing streams are forced through a narrow aperture causing droplet breakup [50]. Here we consider flow-focusing devices, as these provide the best system for producing droplets with sizes smaller than those of the channel dimensions.

However, producing suitable oil-in-water emulsions via microfluidic methods remains challenging. The vast majority of microfluidic emulsification systems are manufactured using polydimethylsiloxane (PDMS). While PDMS is an excellent material for water-in-oil microfluidics [98] offering good solvent compatibility, good optical transmittivity, high flexibility and great durability, it is also strongly hydrophobic, preventing the stable formation of oil-in-water droplets [99]. Although techniques for making PDMS devices hydrophilic

and thereby allowing stable droplet generation exist, these are either short lived such as plasma treatment [100] or involve sequential surface coatings [101] which are impractical for use with devices small enough to easily generate micron scale droplets.

Norland optical adhesives provide a viable alternative to PDMS for oil-in-water microfluidics [102, 103] allowing rapid templating of complex microchannels [104]. Their rapid curing speed, alongside their durability, makes them ideal for pattern transfer from PDMS moulds. Additionally, while natively more hydrophilic than PDMS, exposure to an Oxygen plasma forms a long-lasting hydrophilic surface, ideal for the formation of oil-in-water droplets [102]. Here we introduce a microfluidic flow focussing system based on the use of NOA microfluidics for the generation of monodisperse oil in water emulsions which can produce droplets on the micron scale with polydispersity of below 5%. To demonstrate the utility of this technique, we use the topological cluster classification to investigate the higher order structure of a polydimethylsiloxane oil emulsion, and compare this to a simulated hard sphere system.

3.2 Experimental protocols

3.2.1 PDMS device assembly

Device patterns were fabricated as SU-8 on silicon wafers using standard photolithographic methods, the patterns on the silicon wafer are negative as shown in Fig. 3.1. Silicon device moulds were treated with trichloro(1H,1H,2H,2H-perfluorooctyl) silane to allow easy siloxane lift-off. Polydimethylsiloxane(PDMS) was mixed up in a 10:1 ratio of elastomer to curing agent (Sylgard 184). The mixed silicone elastomer was degassed, and approximately 20 g was poured on the silicon wafers, degassed a second time to remove any remaining bubbles, and heat cured at 60 °C for 6 hours. Once cured, PDMS layers were cut to shape and carefully removed from the silicon wafer. Tubing connectors were punched into the PDMS slabs using a 0.8 mm diameter biopsy punch. The cut and punctured PDMS was subsequently thoroughly washed with isopropanol to clean out any PDMS remnants from the puncturing process. The PDMS chips were then plasma treated for 30 s in a 100 W Diener plasma cleaner. The oxygen plasma treatment modifies the surface of PDMS and introduces silanol group (SiOH) on the PDMS surfaces, this makes the PDMS surfaces hydrophilic for around 30 minutes. Immediately following plasma treatment, the device chip was brought into contact with a similarly prepared glass microscope slide, bonding the activated surfaces together.

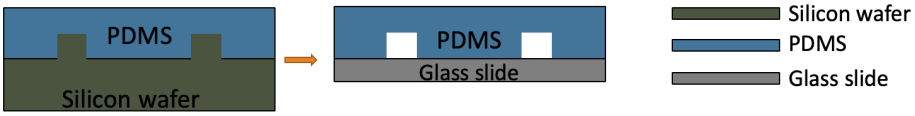

Fig. 3.1 Processes of PDMS microfluidic device fabrication. Mixed PDMS elastomer and curing agent is poured onto the negative silicon wafer, the cured PDMS has positive geometries. The PDMS chip is then enclosed with a glass slide after oxygen plasma treatment.

We consider two different flow geometries, as shown in Fig. 4.1, produced from the same device with a central straight oil channel, to which four water side channels are attached in an x-shaped configuration. Two of the side channels are not punctured during the fabrication process, and therefore are blocked when liquid flows through the device. In the opposed flow system, shown in Fig. 4.1(a), the oil channel is connected so that oil flows from the side of the blockage, so that the water channel makes a 165° angle with the oil channel. Figure 4.1(b) shows the coflowing system, in which the oil comes from the direction of the open channels, leading to an angle of 15° between the aqueous and the oil flow.

3.2.2 NOA device assembly

The geometry of NOA microfluidic device pattern is shown in Fig. 3.2. The dimensions are at similar scale to desired colloidal droplet sizes. There are three patterns with apertures of 3, 5, and 8μm on one silicon wafer, the height of channels is 8μm and the width is 50μm for all devices. NOA devices can not be fabricated directly from silicon wafer, because curing NOA on silicon wafer can very likely damage the features of photoresist on silicon wafers, also it is difficult to peel a stiff cured NOA from silicon wafer. As shown in Fig. 3.3, a PDMS mould is employed in order to prepare NOA devices.

Compared with the silicon wafer utilised to fabricated PDMS devices, the silicon wafer for NOA devices has positive features. A negative PDMS mould is obtained by curing Sylgard 184 on the silicon wafer, which is the same procedure as preparing PDMS devices. Then NOA81 is poured onto the negative PDMS mould, and cured under 365 nm UV light for 30 minutes. Once cured, the NOA chip is drilled at tubing connections, the drilled holes have diameters of 1 mm. The drilled chip is then cleaned with isopropanol and deionised water, in order to remove powder residuals after drilling. A thin slice of NOA is prepared by sandwiching a few drops of liquid NOA in between two flat PDMS sheets, and cured under the same UV radiation for 2 minutes.

Both drilled NOA and the thin slice are treated under oxygen plasma at power of 100 W for 60 s. The plasma treated surfaces of NOA are more hydrophilic (smaller contact angle) than treated PDMS, also the hydrophilicity lasts longer than PDMSThe NOA chip

is enclosed by sticking to the NOA thin slice. Because of the rigidity of cured NOA, the bonding between two NOA surfaces is not as strong as bonding two PDMS surfaces. To improve the bonding between two surfaces, the bonded chip is heated at 60°C for 1 h, before the final step of curing under UV exposure for 2 hours.

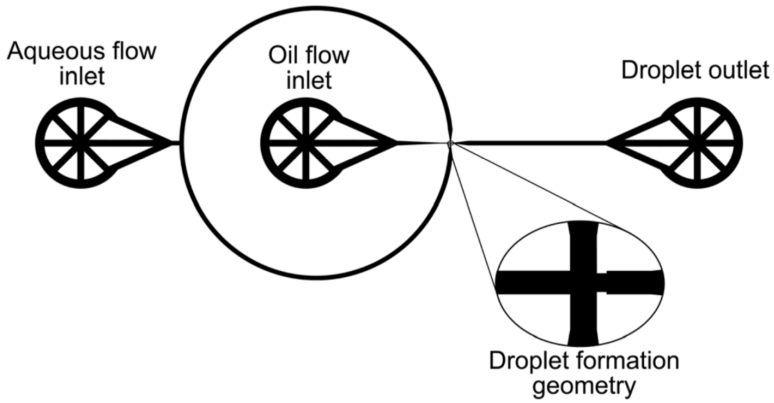

Fig. 3.2 Geometry design of NOA devices. The zoom in image shows the aperture of droplet production. The widths of channels are 50 μm whereas widths of apertures are 3, 5, and 8 μm for three devices, and the height of channels are 8 μm for all devices[46].

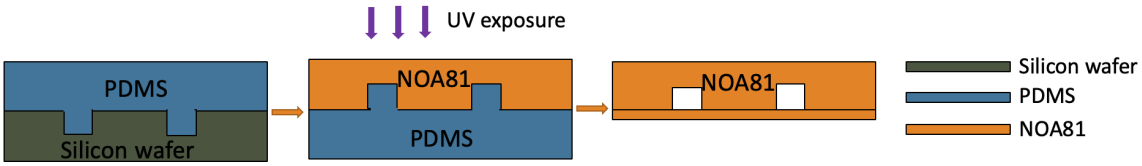

Fig. 3.3 Processes of NOA microfluidic device fabrication. A negative PDMS mould is obtained by curing on the positive silicon wafer. NOA is then cured on the PDMS mould under UV radiations. A thin layer of NOA is made by sandwiching two flat PDMS sheets. The NOA chip and thin slice are bonded after oxygen plasma treatment, and further heating and UV exposures enhance the bonding.

3.2.3 Flow measurements

Liquid flows were pushed through microfluidic channels by using a nitrogen driven pressure pump (Fluigent MFCS), channels are connected to the pump with polyethylene tubings. The maximum pressure of the pressure pump is 1 bar, the minimum increment of pressure is 1 mbar *i.e.* 100 pa.

In the preparation of O/W emulsions, the fluids used for dispersed and continuous phases are listed in Table. 3.1. The control of viscosities is realised by mixing various types of oil and mixing glycerol with water for the aqueous phase. Silicone oil with viscosity of 5 cst is also employed to produce silicone oil in water droplets for confocal imaging.

Table 3.1 Liquid phases used to produce the emulsion systems considered in NOA devices

Oil phase	Aqueous Phase	η_o/η_i
80:20 Cis-decalin/Bromocyclohexane	Deionised water	0.3
80:20 Cis-decalin/Bromocyclohexane	50:50 Deionised water/Glycerol	1.5
Dodecane	50:50 DIW/Glycerol	3.8

3.3 Results and discussion

NOA devices with aperture of 8 μm is employed to produce O/W colloidal emulsions. We investigated the production of droplets at various flow conditions, *i.e.* at a series of flow rate ratios and viscosity ratios of the two phases. The pressure ratio is defined as $r = Q_o/Q_i$ which is the flow rate ratio of outer aqueous to inner phases. The viscosity ratio is $\lambda = \eta_o/\eta_i$.

When the flow rate ratio r is between 1 to 60, droplets are produced in a stable manner. Too low flow rate ratio leads to dewetting of the continuous phase, while too high flow rate ratio results in the situation that the inner channel is filled by the outer continuous fluids.

Two droplet production regimes were found in NOA devices. At low Ca which is the order of 10^{-2}, fluids meet at the aperture, where Rayleigh-Plateau instability happens and leads to the breakup of droplets, as shown in Fig. 3.4(a). The droplets produced in this regime have sizes similar to the dimension of the device aperture, this regime is often called a squeezing regime. At higher Ca of order 10^{-1}, the interface between dispersed and continuous phases is narrowed into a smaller tendril compared with the channel size. The tendril stays stationary at the aperture and breaks up to droplets, droplets are then carried by the continuous flow downstream, as shown in Fig. 3.4(b). This is called a dripping regime, droplets produced through this mode are smaller than the device geometry.

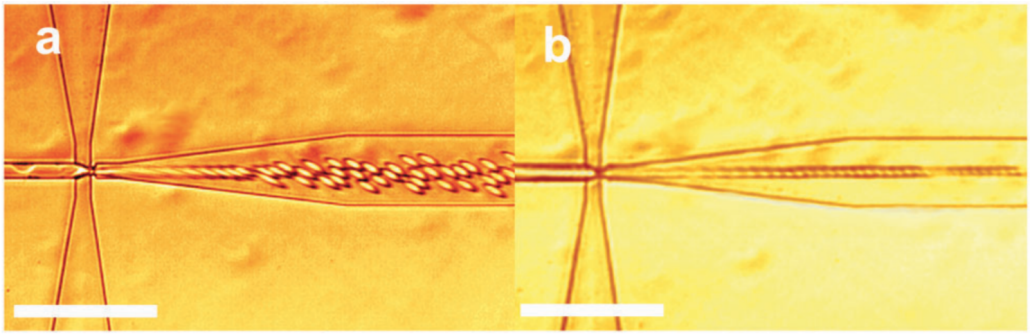

Fig. 3.4 Two droplet production regimes in NOA microfluidic devices. (a) The squeezing regime, where droplets break up at the aperture. The size of droplets is similar to the dimension of device. (b) The dripping regime, where the interface between two phases is narrowed to a smaller tendril, droplets also break up at the aperture but the size is smaller than the device geometry.

3.3.1 Droplet sizes against viscosity ratios

Three viscosity ratios λ of 0.3, 1.5 and 3.8 are examined in the experiment. At low viscosity ratio of $\lambda = 0.3$, droplets are formed stably across the entire range of flow rates stated above, the size of droplets scales inversely with the flow rate ratio r, as shown in Fig. 3.5(a). When increases the viscosity ratio λ to 1.5, first of all, the range of flow rate ratio r is much narrower to stably produce droplets, compared with that of lower λ. Secondly, two different droplet production modes, squeezing and dripping, were found, two modes can be switched by changing the flow rate ratio r, as shown in Fig. 3.5(b). When the viscosity ratio λ becomes 3.8, the continuous phase is much more viscous than the inner dispersed phase, the formation of droplets become unstable. Due to the high viscosity of outer flows and the maximum pressure of 1 bar from the pressure pump, only low flow rates can be achieved. Droplets generated at low flow rates are twice bigger than those produced at lower viscosity ratios, the average radii is above 6 μm, as indicated in Fig. 3.5(c).

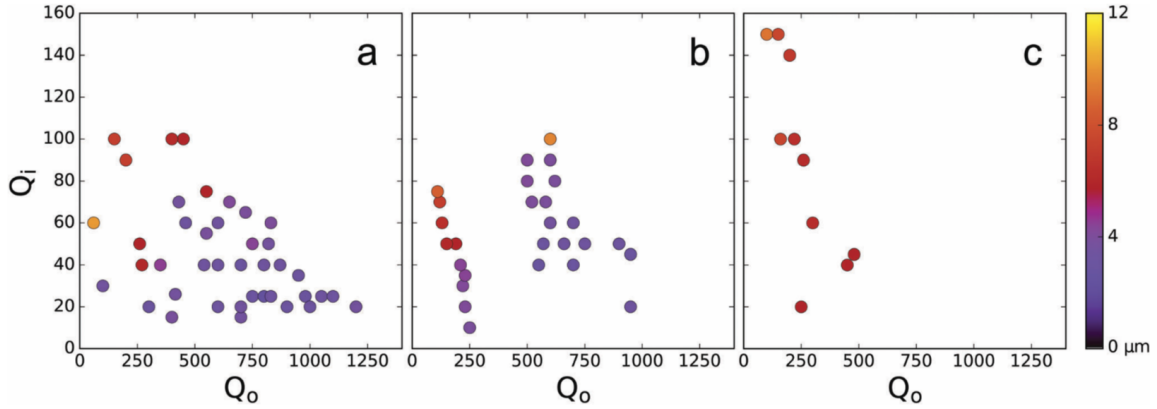

Fig. 3.5 Heatmap of droplet radii against flow rates of outer and inner flow rates at three viscosity ratios $\lambda = 0.3$, 1.5 and 3.8. (a) At low viscosity ratio $\lambda = 0.3$, droplets are stably produced at all flow rates within the range of r, droplets generated have radii from 2 μm to 12 μm. (b) At intermediate viscosity ratio $\lambda = 1.5$, two droplet production regimes were found, it can be switched by changing r. (c) At high viscosity ratio $\lambda = 3.8$, droplet production becomes unstable, droplets formed at low flow rates are twice bigger than those produced in (a) and (b). The increase of λ results in the decrease of flow stability and narrower range of droplet radii.

3.3.2 Droplet sizes against flow rate ratios

We plot droplet radius against flow rate ratios Q_o/Q_i for all three viscosity ratios in a log-log plot, we found a linear scaling in Fig. 3.6. Droplets produced from this NOA device have radii ranging from 2 μm to 12 μm. The slope in the log-log plot is -0.268. Different viscosity

ratios fall into the same scaling of droplet sizes against flow rate ratio. Low viscosity ratio covers the whole range of droplet sizes while high viscosity ratio can only produce relatively bigger droplets from the device. This linear scaling in the log-log plot is in agreement with predictions by Garstecki *et al*[53], and indicates droplets are produced in the dripping regime.

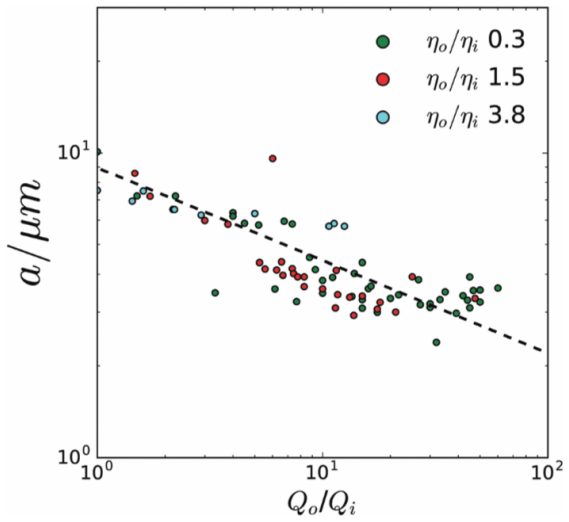

Fig. 3.6 Log-log plot of droplet radius against flow rate ratio. The dotted line which has a slope of -0.268 is drawn to guide eye. The scaling is the same for three viscosity ratios.

3.3.3 Structures of dense emulsions

A few millilitres of silicone oil (5 cst) in water emulsions were collected from the NOA device, at flow rate ratio $r = 10$. In order to match the refractive index of oil and aqueous phase, glycerol was added to the emulsion drop by drop, until the sample becomes transparent. The transparent emulsion is left on the bench for oil droplets to cream under gravity, due to the density mismatch between silicone oil and mixtures of water and glycerol. We took the creamed emulsion droplets and characterised them under a confocal microscope, a 3 dimensional XYZ stack was taken and shown in Fig. 3.7(a). The stack has dimensions of $128.8 \times 128.8 \times 60.1$ μm. Particle coordinates and sizes were obtained using colloidal particle tracking algorithm as described in section 2.5[81]. The average radius of droplets is 4 μm with polydispersity of 5%, the volume fraction of the emulsion is $\phi = 0.42$.

Based on particle coordinates, we calculated the radial distribution function $g(r)$ of the dense emulsion and compared with a hard-sphere liquid at the same volume fraction, as shown in Fig. 3.7(b). The $g(r)$ of the emulsion is more noisy due to the small sample size (1675 droplets were tracked). The comparison of $g(r)$ is qualitatively similar, showing that,

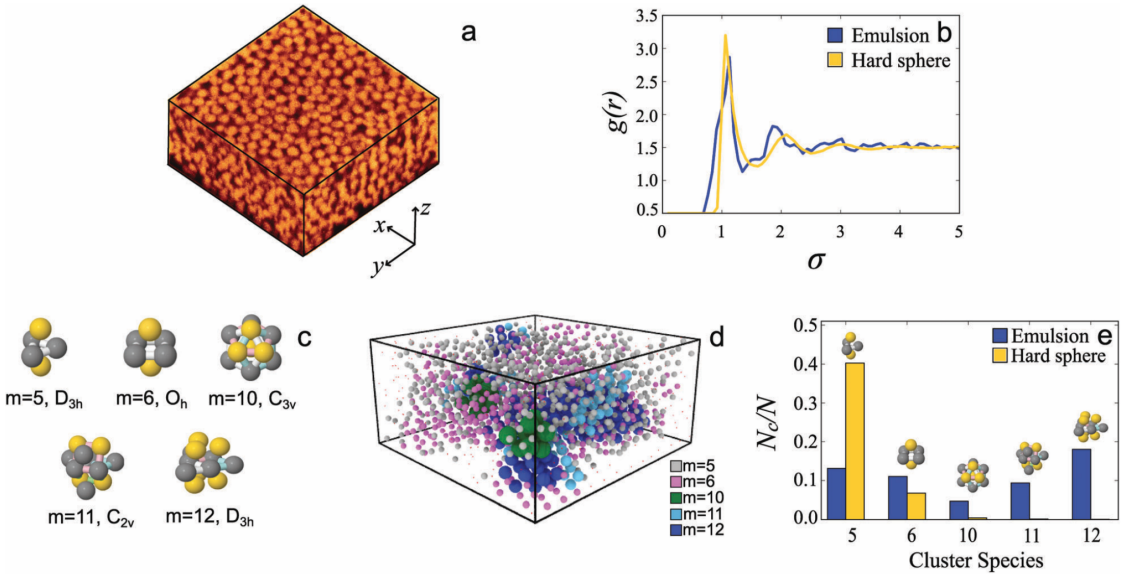

Fig. 3.7 Structural analysis of dense silicone oil emulsions. (a) Confocal microscopy image of the dense emulsion, image dimension is 28.8 × 128.8 × 60.1 μm. (b) Radial distribution function volume fraction $g(r)$ of emulsions and hard sphere liquid, both at volume fraction ϕ = 0.42. (c) A selection of topological cluster classification (TCC) local structures with number of particles m = 5, 6, 10, 11, and 12. (d) Rendering of droplets forming TCC clusters, droplets forming larger clusters are rendered with larger radius. (e) Comparison of TCC populations in creamed emulsions and simulated hard sphere liquid.

at the level of two-point correlations, the emulsions obtained from the NOA device can be used as a hard sphere model.

However, higher order structural measurements show different behaviours. We performed TCC analysis on the dense emulsions, locally favoured structures with number of particles of m = 5, 6, 10, 11 and 12 are the main clusters that are detected, the clusters are shown in Fig. 3.7(c). A rendering of detected clusters in the dense emulsion is also shown in Fig. 3.7(d), the different colors indicate clusters with different number of particles. Fig. 3.7(e) shows the population of clusters detected in both systems.

It is clear that tetrahedra (m =5) is the prevalent local structure in hard sphere liquid at ϕ = 0.42, which accounts for more than 40% of the total number of particles. A few percent of octahedron (m =6) is also identified while larger clusters are almost missing in the hard sphere system. Larger clusters are often detected in hard sphere systems with higher volume fractions such as colloidal glasses, and gels in the colloid-rich phase. The number of clusters with five-fold symmetry, *i.e.* icosahedron (m = 13) or defective icosahedron (m = 10), has been proved to be an effective order parameter to characterise the transition from supercooled liquids to glasses[105]. By comparison, in the emulsion with the same volume fraction, the

population of tetrahedra drops to around 10%, the octahedron accounts for a similar portion. Clusters with number of m = 10, 11, and 12 particles are also identified, which are totally absent in a hard sphere liquid.

The analysis of TCC indicates the interactions between emulsion droplets is distinct to hard sphere interactions. There are two possible reasons to explain the results. First, silicone oil droplets are stabilised with SDS which is an anionic surfactant. The charge stabilisation can lead to a higher effective volume fraction, thereby increases the population of local structures with higher number of particles. The second reason is due to the softness of droplets. Although small droplets have high Laplace pressures which prevent droplets deforming significantly, droplets still can deform to some extent. This deformation allows droplets to rearrange locally more compared with hard particles, therefore leads to the arise of higher order structures.

3.4 Summary

It remains difficult to make sub 10 μm droplets using conventional microfluidic methods, particularly in the case of oil-in-water systems. In this chapter, the application of NOA microfluidic devices provides robust hydrophilic surfaces, and avoids problematic surface coating for channels with a few micrometers. This enables us to generate monodisperse silicone oil in water colloidal droplets.

Droplet size is influenced by the viscosity ratio and flow rate ratio of the two phases. At low viscosity ratio, λ =0.3, the size of droplets scales inversely with the flow rate ratio r. As the viscosity ratio λ increases to 1.5, the range of flow rate ratio r of producing stable droplet becomes narrower. Further increase of viscosity ratio leads to unstable droplet production along with bigger sizes.

The log-log plot of droplet radius against flow rate ratio $r = Q_o/Q_i$ for all viscosity ratios λ = 0.3, 1.5 and 3.8. Different viscosity ratios collapse on a single curve on the log-log plot, with a slop of -0.268. This linear scaling indicates that droplets are generated in the dripping regime.

Using this NOA device, we are capable to produce droplets which have radii ranging from 2 μm to 12 μm. We are also able to collect a decent amount droplets to study the local structural behaviours of dense emulsions.

Chapter 4

Opposed Flow Focusing Microfluidics

Author contributions: the contents of the chapter were based on a published article: J. Dong, M. Meissner, M. A. Faers, J. Eggers, A. M. Seddon and C. P. Royall. *Soft Matter*. 14, 8344 (2018). In this paper, J. Dong discovered the geometry, measured droplet size change with pressure ratio in two geometries, and confocal analysis. M. Meissner carried out the measurement of pressure collapse and drafted the manuscript. All other authors supervised the work and participated in writing of the manuscripts.

4.1 Introduction

Droplet production from a highly focused jet, also known as tip streaming, is a flow mode in which a thin jet emerges from a nearly conical point [106–111]. The jet is subject to the Rayleigh-Plateau instability [112], and decays into droplets further downstream, whose sizes are set by the radius of the jet. However, the circumstances under which such a jet is produced are not understood, and depend crucially on the confined flow conditions realizable in a microfluidic device [111]. In unbounded flows produced by a four-roll mill, G.I. Taylor[106] was able to deform the end of a drop into a conical tip, yet tip streaming occurred only when a small amount of surfactant was added. As the system was drained of surfactant, the jet disappeared once again.

A similar phenomenon was observed in the selective withdrawal geometry, in which an upper fluid phase is withdrawn through a nozzle from near the interface between two fluids layered on top of one another [113, 114]. As the flow rate is slowly increased, the interface is deformed into an increasingly sharp "hump". When the tip of the hump has reached a radius of curvature of about 200 μm, it transitions toward a "spout", in which a thin jet is entrained into the nozzle; with increasing flow rate, the jet becomes thicker.

However, there is hysteresis in the system: one needs to go to lower flow rates for the spout to disappear than those at which the spout was first formed. Thus this system bears the characteristics of a first order transition, in analogy with phase transitions [115, 116]: firstly, it is discontinuous, in that the jet radius jumps from zero (no jet) to a finite value, and vice versa. Secondly, there is hysteresis, in that the values of the control parameter are different depending on whether one passes from jet to no jet or vice versa. Both the hump and the spout states are characterized by a power-law dependence of their characteristic sizes as the control parameter approaches a critical value. This indicates that one is close to a second order transition, in which the characteristic size goes to zero. Hence the difference between jet and no jet disappears, and in the spirit of Landau theory [115] the transition becomes continuous or of second order.

The aim of this section is to use the precise control over the flow field made possible by microfluidics in order to realize this hypothetical second order transition. As the difference between the two states vanishes at a second order transition, we also expect there to be no hysteresis in that case. Achieving a second order transition would mean that the length scale of the jet is no longer set by the size of the microfluidic setup, but rather by our ability to tune the flow parameters close to the transition.

Recently, there has been some progress describing the formation of narrow tips and thin jets in microfluidic devices, both experimentally and computationally [117, 108, 109, 111]. Usually this is achieved by extracting the dispersed fluid from a nozzle with an exterior phase flowing in the same direction (the coflowing configuration). In this situation the "jetting" state, which allows for the formation of the smallest drops, competes with a "dripping" state, characterized by the periodic formation of individual drops from near the nozzle opening [50, 118, 55, 67, 108].

This is what is known as an "absolute instability" [119, 120], in that breakup occurs in the frame of reference of the nozzle. By contrast, drop formation from the jet occurs by a "convective instability", which grows in a frame of reference convected with the flow. Numerical calculations in simple flow geometries have confirmed the possibility of creating thin jets from the tip of conical points [107, 110]. However, jet radii have not been reported in a systematic fashion; in particular, the crucial question of what limits the size of the smallest jet has not been addressed.

A nonlinear analysis of tip streaming [109] uses slender body theory to find jetting states which continue to a vanishing radius. The limiting state at vanishing flux of the inner fluid is the conical solution first found by G. I. Taylor [121]. However, as shown in [122], this solution breaks down if the full axisymmetric Stokes equation is considered, calling into question the basis of this analysis. Another approach uses linear stability analysis of a jet

[108, 67, 123]to find that jetting occurs above a critical capillary number between 0.1 and 1, which depends on the viscosity ratio between the two fluids alone, independent of the size of the jet. However, stability of the jet is only a necessary condition for jetting to occur; the analysis certainly cannot capture the influence of geometry on the transition, as we do. A notable exception is a recent global stability analysis of aerodynamic flow focusing [123], which could be extended to study the effect of geometry.

In this section, we contrast jetting in the conventional coflowing geometry with a novel opposed flow geometry. For each geometry, we systematically vary parameters to reduce the flux of the dispersed phase, to study the behaviour of the system as the jet radius goes to zero.The droplets produced in the opposed flow geometry are small enough so that they are susceptible to the thermal energy of the system, i.e. they are colloidal. Assemblies of such droplets have a well-defined thermodynamic state and thus can explore their ground state, *i.e.* the minimum energy structural conformations under a given effective interaction potential between the droplets [124].

One experimental system where the size of these droplets can be readily exploited is the study of colloidal clusters. Displaying structural ordering rather different from that of bulk materials, colloidal clusters represent one of the clearest links between local geometry and bulk condensed matter [33]. In particular, due to the five-fold symmetry found in structures such as icosahedral and decahedral, colloidal clusters can act as model systems for both biological systems such as viral capsids, or materials such as glassy states where colloidal model systems have led to great insight into how atoms self-organize into (free) energy minimizing locally favoured structures [125, 126, 33, 127]. We demonstrate the utility of the droplets produced via our opposed flow-focusing methods by producing colloidal clusters of droplets via the addition of a depletion potential.

4.2 Experimental protocols

4.2.1 PDMS device assembly

The procedure of PDMS device assembly is previously described in section 3.2.1. We consider two different flow geometries, as shown in Fig. 4.1, produced from the same device with a central straight oil channel, to which four water side channels are attached in an x-shaped configuration. Two of the side channels are not punctured during the fabrication process, and therefore are blocked when liquid flows through the device. In the opposed flow system, shown in Fig. 4.1(a), the oil channel is connected so that oil flows from the side of the blockage, so that the water channel makes a 165° angle with the oil channel. Figure 4.1(b)

shows the coflowing system, in which the oil comes from the direction of the open channels, leading to an angle of 15° between the aqueous and the oil flow.

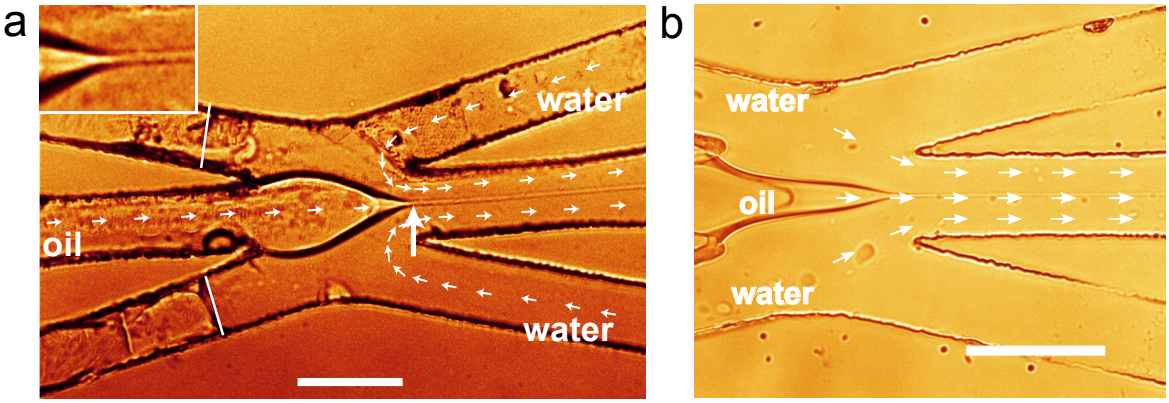

Fig. 4.1 Schematics of: (a) opposed flow system with an angle of 165 ° between the aqueous and oil flow. Inset shows close-up of jet. (b) Coflowing system with an angle of 15 ° between the aqueous and the oil flow. White lines show blocked channels. Scale bars represent 75 μm.

4.2.2 PDMS surface coating

The hydrophobic surface properties of PDMS lead to clogging when producing oil-in-water emulsions. We overcome this difficulty by covering the PDMS with several layers of polymer coating [101], which were applied by flowing alternating polymer electrolyte solutions through the channel by use of a syringe pump. Layers were applied as follows: first 4 μl of poly(allylamine hydrochloride) (PAH), a positively charged electrolyte, was inserted into the channel, so that it coated the negatively charged PDMS surfaces. This was followed by depositing the same volume of poly(sodium 4-styrenesulfonate) (PSS), a negatively charged electrolyte, onto the PAH layer. In total, four layers of PAH and PSS were applied to the PDMS surfaces. In between polymer electrolyte segments, 2 μl of NaCl solution was flushed through the channels to remove excess charge. The solutions of PAH and PSS were used at the same concentration of 0.1 % w/v in 0.5 M NaCl, and the concentration of the NaCl solution used for washing in between the polymer segments was 0.1 M. These segments were loaded into a length of tubing, and flushed through the PDMS device at a flow rate of 50 μl/h.

4.2.3 Flow measurements

Jetting experiments were carried out by connecting the assembled PDMS chip to a pressure pump (Fluigent MFCS) with polyethylene tubing. Silicone oil (shear viscosity 4.57 mPa·s)

dyed with Nile Red was used as the dispersed phase and the continuous phase was a mixture of water and glycerol (30 : 70 wt%) with viscosity 23 mPa· s. This leads to the viscosity ratio of outer to inner phase $\eta_o/\eta_i = 5.0$. The concentration of glycerol is required to be more than 50 wt% for flow focusing to occur under the pressures we applied in the experiments. At this concentration, the dispersed and continuous phases have similar refractive index, it becomes difficult to observe flow behaviours, therefore 70 wt% of glycerol is chosen for this study. In order to produce a stable jet, we reduced the surface tension by adding the maximal soluble concentration of 21mM of sodium dodecyl sulfate (SDS) to the aqueous phase. As this is several times the critical micelle concentration (CMC) [128], we believe that a) desorption of surfactant at the interface is suppressed, and b) replacement of surfactant at the interface is fast enough that the surface tension can be considered constant [111].

4.3 Results and discussion

4.3.1 Droplet and jet production

The driving pressure was controlled using MaesFlo 3.2 software (Fluigent, Paris, France). Pressures were adjusted until the oil flow was stable and producing droplets, as shown in Fig. 4.1 for the opposed flow (left) and coflowing geometries (right). Once stable droplet formation was achieved, flow parameters were adjusted by either holding the external pressure constant and varying the internal pressure, or vice versa. Between measurements, we waited for 15 s after changing the pressure for the jet to stabilize, after which there were no noticeable jet size variations.

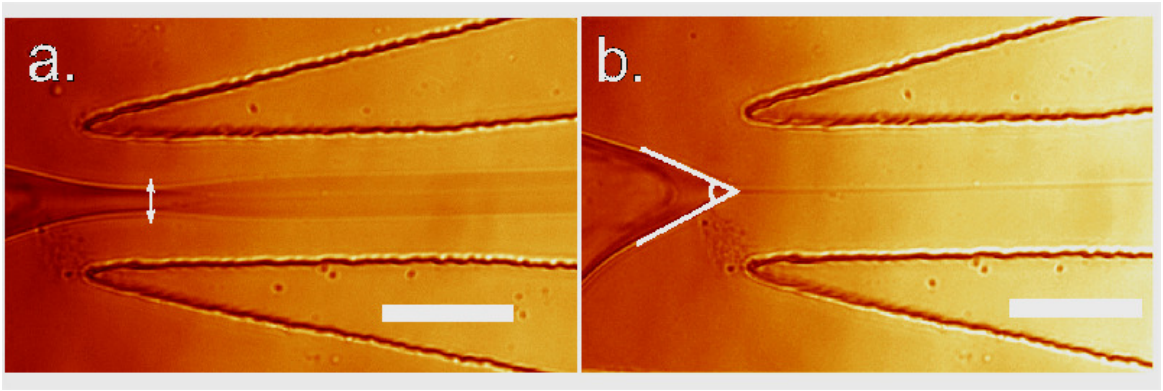

Fig. 4.2 Images of microfluidic devices with opposed flows showing measurement method for (a) the jet width and (b) the cone angle. The pressures of the liquid phases are 700 mbar external, 350 mbar internal, and 700 mbar external, 309 mbar internal, (a) and (b) respectively. Scale bars represent 50 μm.

The former mode of control is illustrated in Figs. 4.2 and 4.3 for the opposed flow geometry. As the internal pressure is lowered, the jet radius becomes very thin, and the oil drop near the nozzle exit assumes an almost conical shape, from which the jet emerges. In Fig. 4.3(a), each color represents the jet radius a as the inner phase pressure is decreased, while the outer phase pressure was held fixed at a certain value from 1034 to 700 mbar. The pressure of 1034 mbar is the upper limit of the pressure pump, while 700 mbar of external pressure is a value slightly higher than the minimum value for flow focusing to occur. In Fig. 4.3(b) we show that all curves can be brought to a near collapse by plotting the radius as a function of the pressure ratio $R = p_i/p_o$, establishing that this ratio is the main parameter determining the state of the system. Since the pressure ratio R is less than 1, the minimum change of pressure is 1 mbar for both the internal and external pressure, by changing the same amount of pressure, the change of internal fluid will lead to a greater change in pressure ratio R and jet radius, comparing to tuning the external pressure. This explains the greater sensitivity to the internal pressure versus the external pressure shown in Fig. 4.3(a).

The jet radius versus pressure measurements were carried out under a Leica DMI3000B bright field microscope. Collected droplets were also characterized under the same microscope with image pixel size of 150nm when using the $\times 40$ magnification lens.

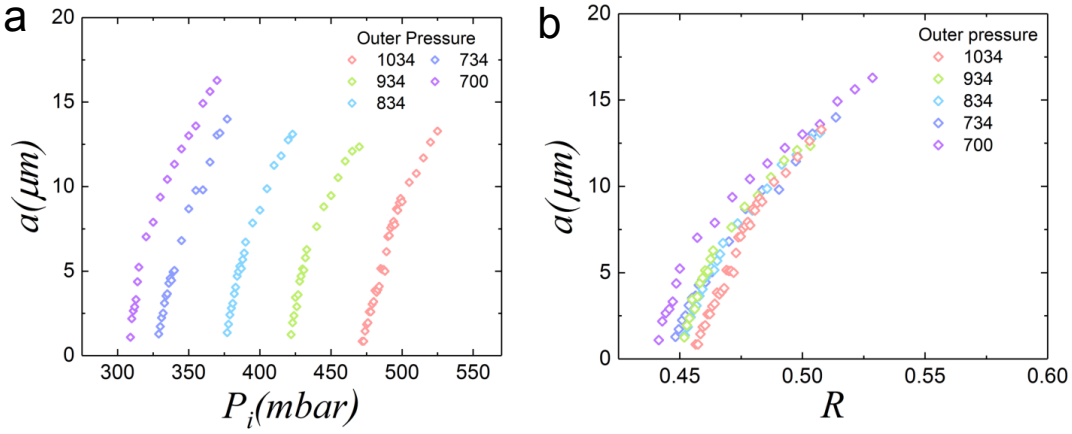

Fig. 4.3 Jet radius a as function of the outer and inner pressures in the opposed flow system. All pressures are given in mbar (a) jet radius versus inner pressure for various outer pressures. (b) Same data plotted against the pressure ratio $R = p_i/p_o$.

Below we contrast the two geometries of coflow and opposed flow. In the coflowing geometry, the smallest attainable jet gives way to dripping, leading to a hysteretic first order transition. In the opposed flow geometry, the smallest jet size is limited only by our ability to control the pressure, leading to a state where flow ceases. Oil drops with radii below 1 μm,

can be produced by this process. Here we show that such colloidal-sized droplets assemble into clusters with the addition of non-adsorbing polymers.

4.3.2 Coflowing jet formation

We begin with the conventional coflowing orientation in order to produce an oil jet from the drop attached to the nozzle, the aqueous flow channels making a 15° angle with the oil channel. By controlling the pressure ratio $R = p_i/p_o$ as detailed in the methods section above, stable droplet formation was induced in the microfluidic device. To characterize the size scaling with pressure ratio, the radius at the narrowest point of the jet was measured.

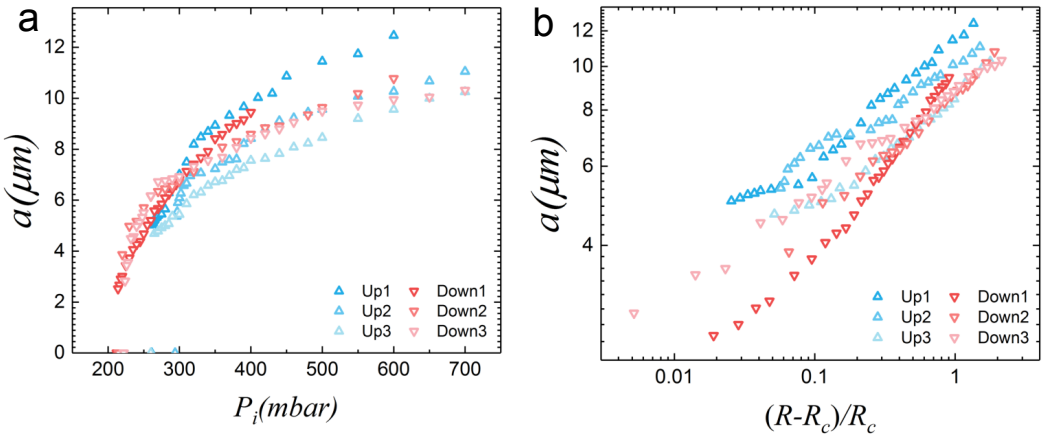

Fig. 4.4 In the coflowing geometry, the outer phase pressure was fixed at $p_o = 700$ mbar, the jet radius was measured while varying the inner oil phase pressure. 'Up' refers to an experimental run during which the inner pressure increases (increasing the jet radius), 'down' where the inner pressure decreases (decreasing the jet radius). 'Up' and 'down' processes were repeated three times to check the stability of the data. (a) jet radius as a function of the inner oil pressure p_i, (b) log-log plot of the jet radius as function of $(R-R_c)/R_c$.

The raw data of jet radius a as a function of the inner flow (oil) pressure p_i is shown in Fig. 4.4(a), while the outer aqueous pressure was fixed at 700 mbar. Shown are three cycles during which p_i increases from zero until a jet is formed and subsequently increases in radius (blue symbols), followed by a sequence of measurements for decreasing p_i (red symbols). There is considerable scatter in the data between each cycle. In addition, for each cycle there is significant hysteresis in that a jet forms at a radius of about 5μm, while the jet disappears only when the radius has decreases to about 2μm. Just below the transition, the system is in the dripping mode, in which oil drops are produced directly from the nozzle in a periodic

fashion. Upon further decrease of p_i, flow stops completely and the interface between oil and the aqueous phase assumes a rounded shape.

To test whether there is some indication of scaling in the coflowing data, in Fig. 4.4(b) we plotted the same radius data in a log-log plot as function of $(R-R_c)/R_c$. For each cycle, and for each data set going up or down, we adjusted a critical pressure ratio R_c such that we obtained a power-law fit

$$a = A(R-R_c)^{\alpha}, \tag{4.1}$$

where A and the exponent α were also adjustable parameters. This means that R_c is the value of the pressure ratio at which the jet radius would vanish in a second order (continuous) transition. However, similar to measurements in the selective withdrawal geometry [113, 114], scaling is cut off at finite a in a discontinuous transition. Scaling exponents also give inconsistent values and were found in the ranges $\alpha = 0.2-0.24$ in the "up" direction, and $\alpha = 0.22-0.37$ in the "down" direction.

4.3.3 Opposed flow jet formation

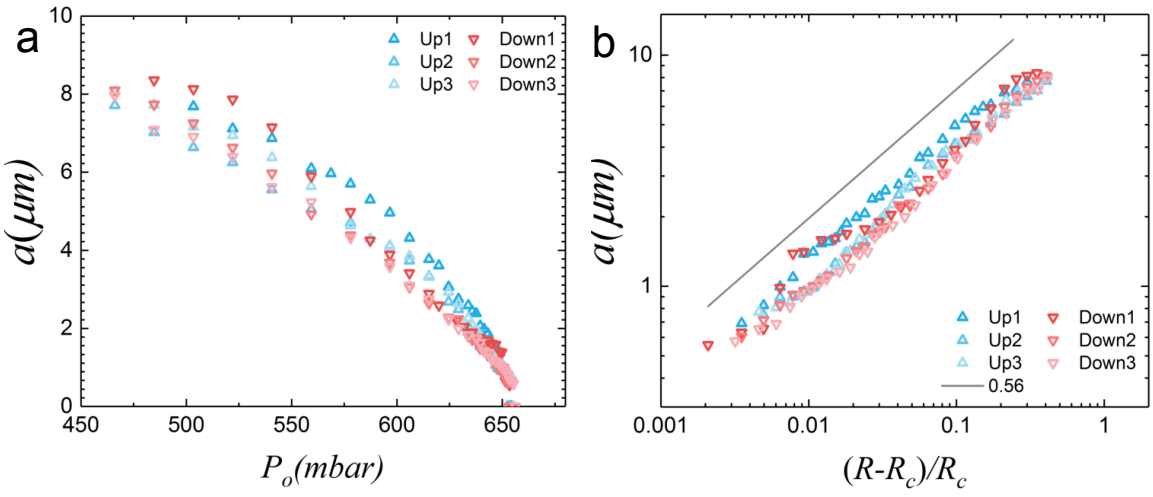

Fig. 4.5 In the opposed flow geometry, the inner oil phase pressure was fixed at $p_i = 275$mbar, the jet radius was measured while varying the outer phase pressure. 'Up' refers to an experimental run during which the outer pressure decreases (increasing the jet radius), 'down' where the outer pressure increases (decreasing the jet radius). (a) jet radius as a function of the outer aqueous pressure p_o, (b) log-log plot of jet radius as a function of $(R-R_c)/R_c$. The line in (b) has a slope of 0.56.

By inverting the flow direction of the oil, we now report results for the novel opposed flow geometry, in which the angle between the aqueous flow channel and the oil flow channel is 165°. In Fig. 4.5(a) we show the jet radius for three cycles of increasing jet radius and

decreasing jet radius. This time, the inner oil phase pressure was fixed at $p_i = 275$ mbar, while the outer pressure p_o was varied. Hence during the "up" phase, p_o is decreased so as to increase R, while during the "down" phase p_o is increased. In the opposed flow geometry, there is very little hysteresis, and there is a much better collapse of the data across the three cycles of varying the outer pressure. This is even clearer in the log-log plot of Fig. 4.5(b), where for each cycle and for each direction of increasing and decreasing p_o, we fitted the data to the power law (4.1). With the critical value R_c in hand, we plotted a against the critical pressure parameter $(R-R_c)/R_c$.

There is now little variation of the slope in each case; in the "up" direction we obtain values $\alpha = 0.55-0.58$, in the "down" direction $\alpha = 0.54-0.57$. Fitting to the data for all three cycles leads to an average exponent of $\alpha = 0.56$, shown as the straight line in Fig. 4.5(b). The smallest jets produced in the opposed flow geometry have a radius of about 0.5μm, this approaches the smallest droplets that are currently produced in flow focusing devices, see Table 1.1. Similar size oil droplets were generated in a needle facilitated flow focusing system[64], even smaller droplets were only realised when dispersed phase is mercury in a double flow focusing set up[67]. One example of collected droplets from the device was characterized under the confocal microscope and is shown in Fig. 4.6(a), with mean radius of 1.2μm. We were unable to determine whether there remained a small discontinuity as the jet disappears, or whether our ability to produce a small jet is limited by the accuracy with which the outer pressure can be adjusted. Most importantly, in the opposed flow geometry we no longer see a dripping state, but we pass directly from a jetting state to a state of no flow.

4.3.4 Droplet clusters

With this novel opposed-flow geometry, we have collected droplets with radius of approximately 1.5 μm. Being in the colloidal regime, thermal motions of these droplets are able to compete with the gravitational stresses. These droplets thus can self assemble to different complex structures which in turn show intriguing behaviours and have wide potential applications. Among these complex structures formed by colloidal particles, we are particularly interested in cluster aggregations and colloidal gels which have extensive applications in formulation industries.

By adding non-absorbing polymers tho these colloidal emulsions, depletion attraction is induced. We add hydroxyethyl cellulose (HEC) to the aqueous phase with concentration of 6.34 mg/ml. The gyration radius of HEC is 50 nm, this leads to a colloid to polymer size ratio of approximately $q \approx 0.03$. Droplets are collected at fixed inner phase pressure of 275 mbar with the aqueous flows kept at 640 mbar. The resulting droplets were collected

into a glass capillary and imaged under a confocal microscope (Leica SP-8) with excitation wavelength of 514 nm.

Since the jet decays into droplets further downstream, the very thin jets produced in the opposed flow geometry allow us to make correspondingly smaller droplets, with hydroxyethyl cellulose polymers added to them. Owing to the short-range depletion attractions induced by HEC polymers, colloidal droplets with mean radius of 1.5 μm form clusters, as shown in the confocal images of Fig. 4.6(b)-(e). These enable studies in the same spirit as [126], but with 3d imaging, as the system is refractive index matched. In Figs. 4.6(b)-(e) we show closeups of individual clusters with $N = 2 - 5$ particles; the wireframe inserts indicate the geometry of the cluster.

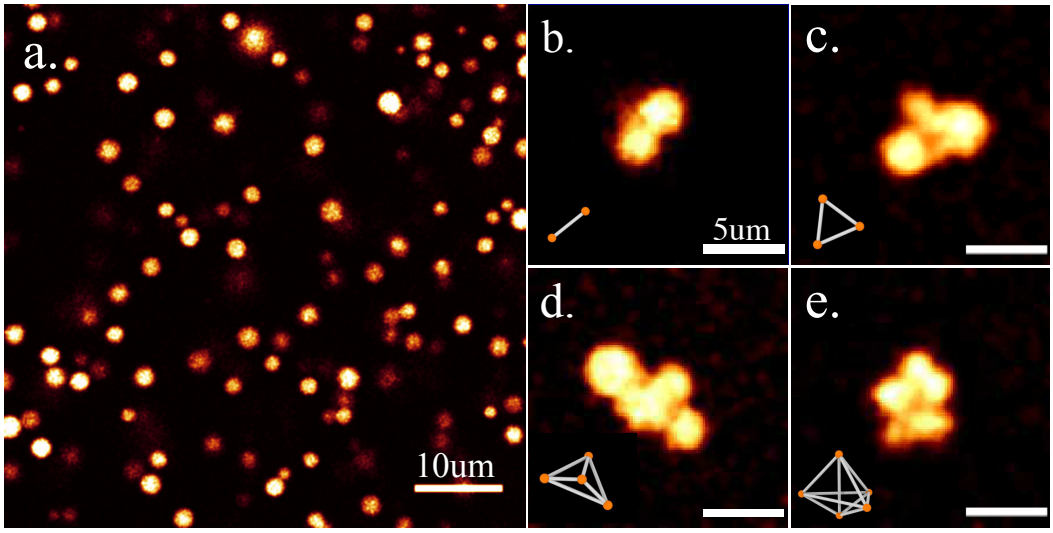

Fig. 4.6 Confocal microscopy images of collected droplets and clusters from the opposed flow focusing device. (a) Colloidal emulsion droplets with mean radius of 1.2 μm, the scale bar represents 10 μm. (b) - (e) Collected droplet clusters that are formed by depletion attraction of non-absorbing polymers HEC. Clusters contain droplets from N=2 to N=5, with wireframes indicating the geometry of clusters; scale bars represent 5 μm.

Our new model system enables the study of near-frictionless droplets. Unlike systems with solid particles, where access to the thermodynamic ground state is often suppressed [127, 129], perhaps due to the polymer stabilizer layer thickness being the same size as the depletion polymers [130], these near-frictionless droplets may be better able to reach the ground state. The potential to generate smaller droplets with this method further enables us to form clusters with less tendency to sediment, and which may explore their configuration space very quickly, as the colloid diffusion time scales with the cube of the diameter. With a higher volume fraction of droplets, percolating colloidal gels can be obtained through the same depletion mechanism [23, 131, 132].

4.4 Summary

By tuning close to a second order transition in an opposed-flow geometry PDMS microfluidic device, we can reduce the droplet size by almost an order of magnitude compared with the dimension of the device. With finer control over the relative pressures of inner and outer flow, one can approach even closer to the transition, our method therefore has the potential of reducing droplet size practically without limit.

In agreement with previous results, we find that the smallest jet size is limited by transition to a dripping state. In the opposed flow geometry, on the other hand, dripping is suppressed, and the smallest jet size of about 1μm appears to be limited only by our ability to adjust parameters close to a second order transition.

We demonstrate the utility of the droplets produced here via the production of colloidal clusters, an experimental system which is challenging to access otherwise. In addition to the many applications that colloidal clusters offer, we believe the phenomenon detailed above presents many opportunities for further development.

Of primary interest would be a thorough investigation of the effect of angle on the droplet generation behaviour, as well investigating whether the same effect is suitable for the production of bubbles, a useful system with many biomedicine applications [1].

Chapter 5

Contact Force Measurements in Colloid-Polymer Mixtures

5.1 Introduction

The response of a material to mechanical loading is one of its most basic properties, and many applications require control over yielding, flow, and fracture of soft matter. These phenomena observed in macroscopic systems are ultimately determined by the microscopic structure of the material.

To link macroscopic yield behaviour to the microscopic structure of these systems, it is useful to consider the (tensorial) stress field $\sigma_{ij}(r) = \frac{1}{V}\sum_{c=1}^{N^c} \boldsymbol{f}_i^c \boldsymbol{r}_j^c$, which may be defined in terms of the particle positions $\boldsymbol{r}_j^c$ and the interparticle forces $\boldsymbol{f}_i^c$[133]. On the micro-scale, the stress is a fluctuating quantity that is intrinsically linked to the particles packing in space, *i.e.* the local structure. However, on passing to the macro-scale, the fluctuations in σ are no longer apparent, and the system obeys a constitutive relation that relates applied forces (stress) and material response (strain).

The stress field is challenging to measure in experiments, because it depends on interparticle forces. Interparticle contact force study has been an important part in the field of granular matter over a long time. Understanding contact forces and their spatial correlations, represents a fundamental goal of granular mechanics. The problem is of relevance to civil engineering, geophysics, and physics, being important for the understanding of jamming, shear-induced yielding and mechanical response[134]. In this chapter we will review some experimental methods and study on measuring contact forces in both 2D and 3D granular matter and then present our tailored method of measuring contact forces in 3D colloid-polymer mixtures.

5.1.1 Contact force measurements in 2D systems

One of the first experimental force measurements on high density packings was carried out using 3 mm Pyrex spheres. These spheres are immersed in a box with refractive index matched fluid which is a mixture of glycerol and water. A piston is placed on the top surface of the sample box to apply forces, spheres become bright if they are under strains because of the stress-induced birefringence[135]. It is found that forces are distributed inhomogeneously, large forces are exponentially rare. It is also observed that beads under stresses are forming chains which are distributed not uniformly. The authors suggested that the formation of force chains is due to the inhomogeneity of the particle packing which causes an unequal distribution of the weights on the beads supporting a given grain.

By far the most popular 2D experimental system of studying contact forces in granular matter is using photoelastic disks. When photoelastic materials are subject to stresses, they become birefringent and when viewed between crossed polarisers, exhibit light and dark bands which encode the detailed stress within each particle, as shown in the left of Fig. 5.1, while they appear colourful transparent disks without polarisers (Fig. 5.1 middle). Based on the image of photoelastic patterns, a nonlinear least-squares fit of the patterns to the known plane elasticity solution for the stresses inside a photoelastic disk is applied. The fitting yields the stress field inside each disk and the determination of contact forces[5][136]. These disks can also be labelled with fluorescent marks, which will glow under UV illumination as shown in the right of Fig. 5.1. In this way it is possible to track the positions of disks and also their rotations.

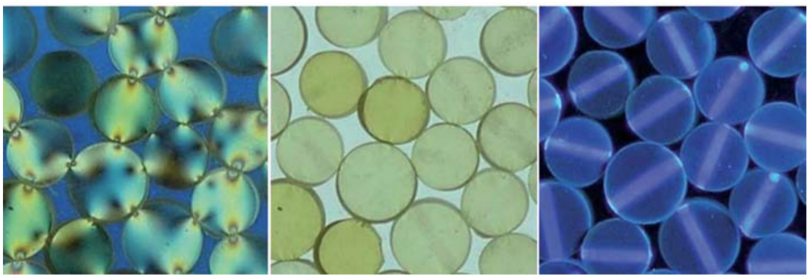

Fig. 5.1 Photoelastic disks between crossed polarisers (left), without polarisers (centre) and without polarisers but with UV illumination (right)[5].

One application of photoelastic disks is studying the mechanical response of a 2D disk system under pure compression or shear. Isotropic force networks are observed when the disks are subjected to compression forces; by comparison, there is anisotropy in both contact forces and contact networks when shear is applied, as shown in Fig 5.2(a) and (b). They also found long-range correlations in the direction of force chains in sheared systems but only short-range correlations in isotropically compressed systems regardless of the direction[136].

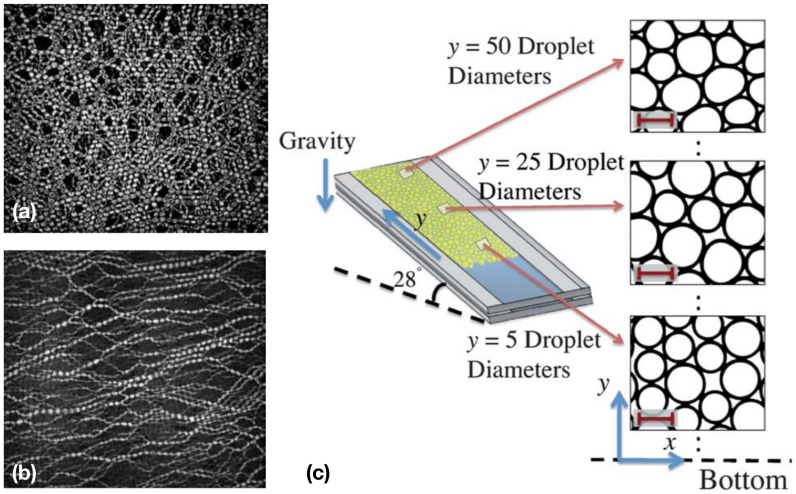

Fig. 5.2 (a) Force networks in photoelastic disks which are subjected (a) compression and (b) shear stresses[136]. (c) A quasi 2D jamming system with emulsion droplets, various area fractions are realised due to the angle of the cell and gravity of droplets. Droplet contacts are calculated from deformation of droplets which are determined from the outline of droplets[6].

A similar system has been applied to investigate the phase behaviour of the jamming transition. In the phase diagram proposed by Liu and Nagel, at T = 0 without external stress, the jamming transition occurs at a critical volume fraction[137]. The value of this critical volume fraction of jamming is lowered when external stresses are presented[134]. By using frictional photoelastic disks, Bi *et al*[134] found that at a relatively small shear stress, the system comes to a fragile state with a strong force network percolating only in one direction. Above a minimum shear stress, the system becomes shear-jammed, having a force network that percolates in all directions.

A quasi-two-dimensional jamming system has been built by Desmond *et al*[6] where bidispersed oil-in-water emulsion droplets with various size and number ratios were confined between two parallel glass plates, as presented in Fig. 5.2(c). They found the contact number and pressure have critical scaling with $\phi - \phi_c$ where $\phi_c \approx 0.86$ in their systems. They did force chain analysis where they define a force segment belongs to a force chain if this segment is one of the two largest forces on both droplets that are joined by the force segment. The relative orientation of force chain segments are random but there is a tendency that force chains are linear which allows the two largest forces to be balanced on a droplet. Through verifying the link between the force law and the critical pressure exponent, the study shows a direct relation between the bulk properties and the particle interactions.

5.1.2 Contact force measurements in 3D systems

Although it has been proved that photoelastic material has the capability to reveal contact forces in granular systems, it is challenging to apply this technique to study 3D systems because the reflection of particle surfaces will affect birefringes. Other materials such as hydrogel particles, elastic shells and emulsions have been functionalised or modified to achieve this goal at the athermal level.

The first example is carried out by Brodu *et al*[138], they utilised hydrogel particles with a mean diameter of 2.1cm labelled with fluorescent dyes. These particles were immersed in a box filled with a mixture of water and vinylpyrrolidone, which is refractive index matched with hydrogel particles and also nearly density matched. A laser sheet is scanning perpendicularly to the direction of uniaxial compression, as shown in Fig. From the laser scan they can construct 3D images of hydrogel particles, find detect particle deformations based on geometric properties of particles and further calculate contact forces. They combined force measurements at micro-scale level and macro-scale mechanical response, along with a mean field calculation they showed a deep entanglement of force and structure in disordered packing systems and this entanglement is crucial for the observed nontrivial mechanical response.

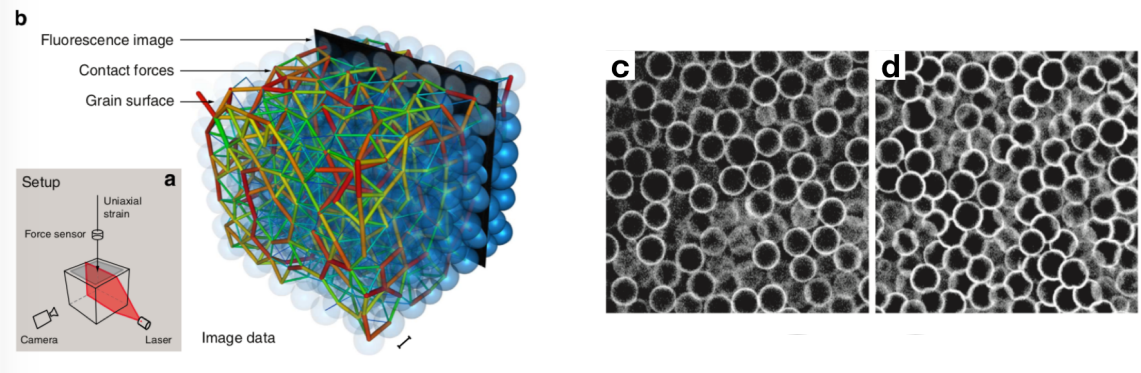

Fig. 5.3 (a) Schematic of the setup of measurements using hydrogel particles. Dyed hydrogel grains are immersed in an index-matched bath, and subjected to a uniaxial strain. Particles are illuminated by a moving laser sheet and imaged by a digital camera. (b) Superimposed image data where blue semitransparent balls are the reconstructed particle surfaces, rods show forces between grains, which are determined from the reconstructed grain surfaces and contact deformations[138]. Confocal images of elastic shells at volume fractions (c) $\phi = 0.663$ and (d) $\phi = 0.908$. Contact forces are calculated based on the degree of shell buckling[80].

Another example is using fluorescently dyed elastic shells. These elastic shells of tetraethoxysilane crosslinked polydimethylsiloxane (PDMS) were prepared by evaporating templating PDMS droplets. These shells were also dispersed in refractive index matched

solvents. The dispersions with various volume fractions were characterised under confocal microscopy, the magnitude of contact forces depends on the degree of shell buckling. Compared with other soft deformable materials, elastic shells show buckling behaviour when the compression is high, the force has a square root relation with the amount of deformations, rather than a linear relation for small deformations. In the jammed granular elastic shell system, Jose *et al*[80] found that near the jamming transition volume fraction, the probability distribution of interparticle forces $P(f)$ decays nearly exponentially at large forces and becomes more Gaussian with increasing packing density up to 0.913. A shear-induced anisotropy was observed after applying a small shear strain to the granular system at low shear rate.

Some earlier studies employed emulsion droplets with functionalised surfaces as model system to resolve particle contacts in 3D. Zhou *et al*[78] visualised interdroplet contacts by labelling liquid droplet surfaces with a single layer of fluorescent nanoparticles or modified cowpea mosaic virus. Droplets which are in contact are fluorescent under confocal microscope, as indicated as yellow parts in Fig. 5.4(a). They measured contact forces in three-dimensional piles of these non-Brownian frictionless droplets, and discovered large forces form long-range chainlike correlations and the correlation decreases as load is applied to the droplet pile.

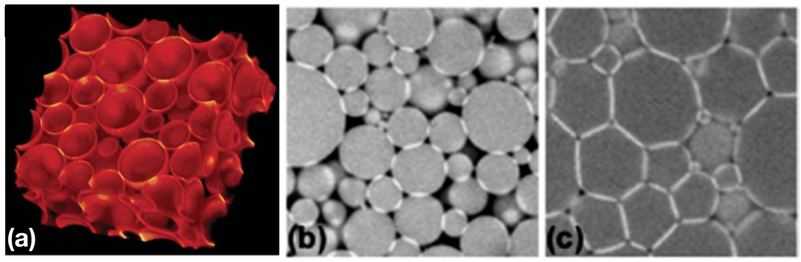

Fig. 5.4 (a) A 3D image of liquid droplets showing the fluorescence from surfaces. Droplets are formed from a mixture of perfluorodecalin and α,α,α-trifluorotoluene, and are labelled with fluorescent nanoparticles[78]. A 2D slice of PDMS emulsion droplets imaged by confocal microscopy under different centrifugation (b) 6000 *g* and (c) 8000 *g*[3].

Brujic developed an emulsion system where PDMS droplets are dyed with Nile Red, droplet contacts have higher fluorescent intensity and can be identified due to the solvatochromic properties of the dye, as shown in Fig. 5.4(b) and (c). This method was proved to be able to effectively measure contact forces in 3D jammed emulsion droplets under different external compression[76, 3, 139]. This experimental method has been applied to study other systems and phenomena. A 'granocentric model' was proposed to describe random packing of jammed emulsions based on particle contact analysis[140]. Jorjadze *et al*[141] found nonlinear response of pressure with packing density away from the jamming point in an emulsion

system with nearly harmonic interaction. The same authors also characterised emulsions with attractive droplets, and discovered that long-range correlations are not important for the system, because for all attractions, the fluctuations in parameters describing each particle agree well with a local stochastic model.

All examples listed above show that there is a series of fruitful research on contact force measurements in granular matter. However to the best of our knowledge no experiment has been carried out to measure contact forces in any colloidal system. Hence we took advantage of the technique developed by Brujic and applied it to a number colloidal systems. We aim to study the mechanical properties at microscopic level from contact force measurements and find the link between microscopic forces, bulk mechanical properties and packing structures.

In this chapter, we present experimental work on contact force measurements and structural characterisation in a number of colloid-polymer mixtures with various attraction strengths.

5.2 Experimental methods

Colloidal PDMS droplets used for this section are prepared through chemical synthesis as described in section 2.1. The average diameter of droplets is 3.2 μm and droplets are dyed with Nile Red.

5.2.1 Colloid - polymer mixture preparation

The non-absorbing polymer utilised to induce depletion attraction is hydroxyethyl cellulose (HEC), which is non-ionic and water soluble. The molecular weight M_W of Natrosol HEC 250 G (Ashland-Aqualon) is 3×10^5 g mol^{-1}. The estimated gyration radius R_g from static light scattering is 50 nm[142, 143].

Colloid-polymer mixtures are prepared by adding stock solutions of HEC polymers (10 gL^{-1}) to concentrated emulsions with volume fractions around random close packing. The solvent of HEC stock solutions is the mixture of water and glycerol (51 wt% : 49 wt%), which has the same refractive index match as oil droplets. The index matched water and glycerol mixture without polymers is also used to adjust the final colloid volume fraction ϕ_c and polymer concentration C_p. All solutions and emulsions contain 10 mM KCl in order to screen negative charges on droplet surfaces, this results in a Debye length λ_D of 6 nm in the final colloid-polymer mixtures[142]. The Debye length is much shorter than the polymer gyration radius so that electrostatic repulsion can be neglected. Once the sample is prepared, the mixture is left on a roller bank for 5 min at the speed of 5 rpm to gently mix the sample.

The critical micelle concentration (CMC) of sodium dodecylbenzenesulfonate (SDBS) in water is 0.4 mM[71]. The concentration of SDBS in the synthesised dilute emulsions is 2 mM, the stock solution of HEC has the same concentration of SDBS. Since this concentration is higher than the CMC, SDBS micelles exist in the concentrated emulsions and colloid-polymer mixtures. These micelles have the possibility to behave like non-absorbing polymers and induce depletion attraction, then it is crucial to know the volume fraction of SDBS micelles and check if they could play the role of depletant. The micelle size of SDBS is 2.0 nm[144], by considering the surfactant concentration of 2 mM, the volume fraction of micelles is 4×10^{-5}, which corresponds to a concentration of 0.014 gL^{-1}. This small number can be considered as zero, therefore we are able to neglect the attraction induced by surfactant micelles.

The well mixed colloid-polymer mixture is then transferred to a home-made glass sample cell. To make the sample cell, firstly two coverslips are glued onto a glass slide with separation around 1 mm. A third coverslip is then glued onto the top of the previous two coverslips using Norland Optical Adhesive (NOA63), in order to bridge between these two coverslips and build a channel similar to a capillary. The glue between the coverslip and glass slide is a mixture of NOA63 with low concentration of silica beads ($\approx 50\ \mu$m in diameter), therefore the gap between the coverslip and glass slide is slightly above 50 μm, between 60 - 80 μm. The confinement of the sample cell is designed in order to fully scan the gel in z direction and monitor the revolution of gels at different timescales. Once the sample is loaded to the channel, the channel is sealed with normal NOA63 glue at two ends.

Given the diameter of the droplet which is 3.2 μm, the viscosity of the continuous phase is 6 mP·s, we calculated the Brownian time of PDMS droplets is 19 s from the equation $\tau_B = \sigma^3 \pi \eta / (8 k_B T)$[9]. Therefore, all colloid-polymer mixture samples are observed under confocal microscope at about 16 τ_B.

5.2.2 Confocal microscopy characterisation

A drop of immersion oil with refractive index of 1.515 was placed on the middle of the glass channel, to reduce the light scattering at the interface between the coverslip and lens, because the immersion oil has a closer refractive index to the glass coverslip than the air. The lens we used is an oil objective lens (HC PL APO 100×/1.40 OIL). We employed two excitation lasers with wavelengths of 514 nm and 580 nm and two HyD hybrid detectors with detection wavelengths of 520 nm - 575 nm and 585 nm-640 nm. These two lasers and detectors are applied to detect fluorescent signals from PDMS oil droplets and interfaces respectively, and they are applied in a sequence by frame fashion.

Table 5.1 Experimental details of colloid-polymer mixtures with various polymer concentrations

$C_p(gL^{-1})$	ϕ_p	ϕ_c	Polydispersity	Potential energy (k_BT)
0.77	0.8	0.27	0.08	37
1.09	1.2	0.24	0.07	55
1.89	2.0	0.23	0.09	93

The image size in x and y directions are 512 $\times$ 512 pixels, the number of pixels in z direction is around 512 but it depends on the height of the sample cell. The diameter of the droplet corresponds to approximately 20 pixels, so the pixel size ranges from 80 nm to 150 nm if the droplets have diameters from 1.6 μm to 3.0 μm. To reduce the noise of the captured images, we applied Line Averaging of 32 to each frame. To increase the scanning speed, we used bi-directional scanning mode. Under this condition, it takes about 19 min to scan a 3D stack with dimension of 512 $\times$ 512 $\times$ 512 pixels.

5.3 Results and discussion

5.3.1 Phase behaviours

A number of colloid-polymer samples are prepared with various polymer concentrations C_p. In the colloid-polymer samples, PDMS droplets have size of 3.2 μm, the depletant polymers are Natrosol HEC 250G which has gyration radius of 50 nm. This gives effective short range attraction in the system, and leads to a polymer to colloid size ratio q = 0.03. Sample details are listed in Table 5.1, the table shows polymer volume fraction ϕ_p, colloid volume fraction ϕ_c, and polydispersity of colloidal emulsions which are obtained from particle tracking.

There are three samples explored with various polymer concentrations. Based on AO model and by matching $B_2^\star$ = -1.5, we found the critical volume fraction of polymers ϕ_p^c = 0.12, above which the system phase separates into colloid-rich (liquid) and colloid-poor (gas) phases, the system is then followed by the dynamical arrest due to the high density in the liquid phase and form a gel[30, 145]. This value corresponds to a attractive potential energy of 5 k_BT. However, the minimum volume fraction of polymer ϕ_p=0.6 is required to form a gel, based on experimental observations. This is four times higher than the theoretical value and we suspect there are two reasons to cause this discrepancy. First of all, there are still charges remaining even after the addition of salts. The charges might come from residual charges on droplets or anionic surfactants that are not completely screened by the salt, or non-absorbing polymers which carry out charges by itself. The second reason is possibly due to the wrong estimation of the gyration radius of non-absorbing polymers HEC. The gyration

radius considered here is 50 nm which is calculated from viscosity measurements, under the condition that water as the solvent[143].The dielectric constant ε_0 of the aqueous phase is 65 at room temperature[146].

All three samples have polymer concentrations higher than the critical value, therefore all of them are in the gel state. Three gels are characterised under confocal microscope following the method described in Section 5.2.2, Fig. 5.5(a) - (c) are confocal images (2D xy slices) of droplets of each gel, and Fig. 5.5(d) - (f) show interdroplet contacts of corresponding samples.

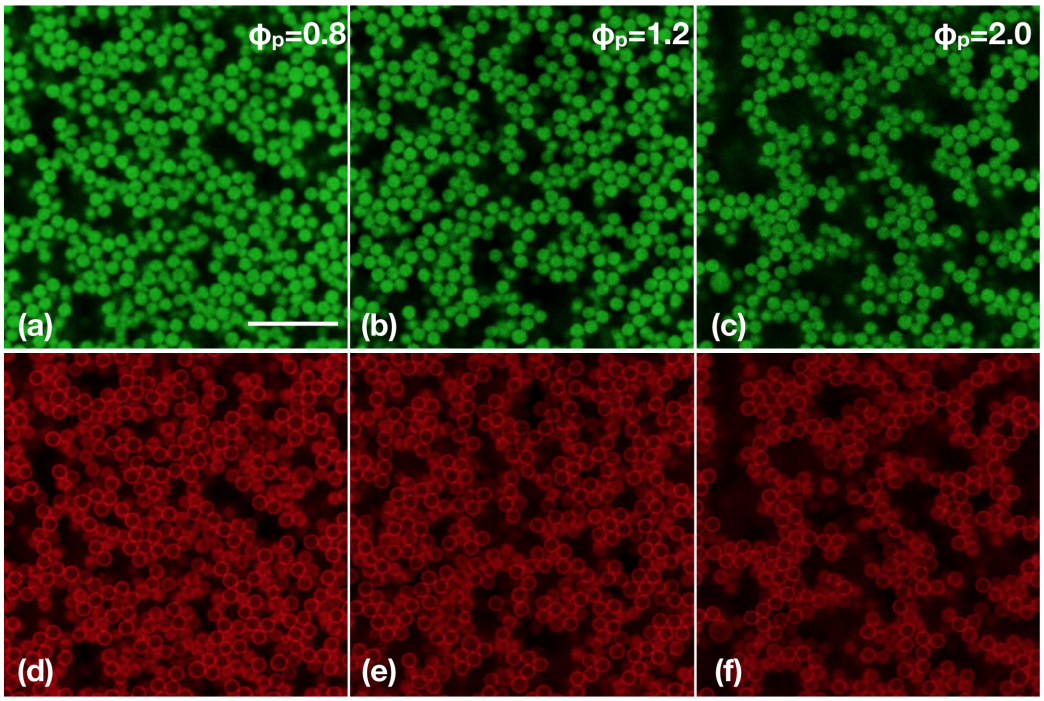

Fig. 5.5 Confocal images of colloid-polymer mixtures with three different polymer volume fractions: (a) 0.8, (b) 1.2 and (c) 2.0. Images of (d) - (f) show contacts of corresponding colloid-polymer mixtures. The scale represents 20μm.

From 3D confocal images, particle coordinates are obtained using the particle tracking algorithm described in section 2.5. The coordinates are rendered in the software Ovito and snapshots are shown in Fig. 5.6 for each gel[147]. The number of particles tracked for all samples is around 6000.

5.3.2 Structural analysis

Based on particle coordinates obtained by particle tracking, we investigate structural properties of three colloid-polymer mixtures, by looking at their pair correlation functions,

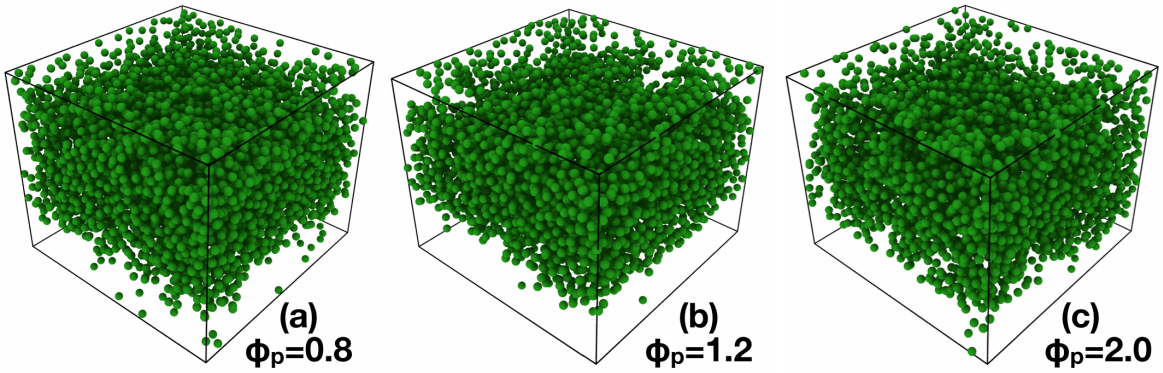

Fig. 5.6 Rendering of particle coordinates of colloid-polymer mixtures with three different polymer volume fractions: (a) 0.8, (b) 1.2 and (c) 2.0.

distributions of number of neighbours and contacts, and populations of topological cluster classification (TCC) clusters, as described in the Introduction chapter in section 1.4.2.

Pair correlation function

From the tracked coordinates of particles, the pair correlation functions $g(r)$ of three colloid-polymer mixtures are calculated and shown in Fig. 5.7. The particle tracking error is approximately 5%[148]. In this figure, as polymer concentration increases, curves are shifted upwards for one unit each time for a better visualisation. A large first peak at the position of one particle diameter is found for all three samples, it indicates a large number of bound particles in the sample and is reminiscent of structures of percolated gel-like networks.

From Fig. 5.7, we also observe non-zero values in $g(r)$ at positions less than a particle diameter σ which is absent in theory calculations such as Percus-Yevick approximation, this means we can find particles around a reference particle at a distance less than the averaged particle diameter, therefore implies a small polydispersity in the sample[149].

Number of neighbours

The number of neighbours of a reference particle is calculated by counting the number of particles within a certain distance from the reference particle. This distance is normally where the first minimum is in $g(r)$, here is 1.2σ for all samples.

The distribution of number of neighbours N for three gel samples is plotted in Fig. 5.8. For both samples with ϕ_p of 0.8 and 1.2, the peak of the distribution stays at 8 while with higher polymer concentration at ϕ_p = 2.0 (yellow), the peak decreases to 7. The decrease of N indicates that gel structures become less packed when gels are deeper quenched. During the quenching process of a colloid-polymer mixture, particles in deeper quenched gels have

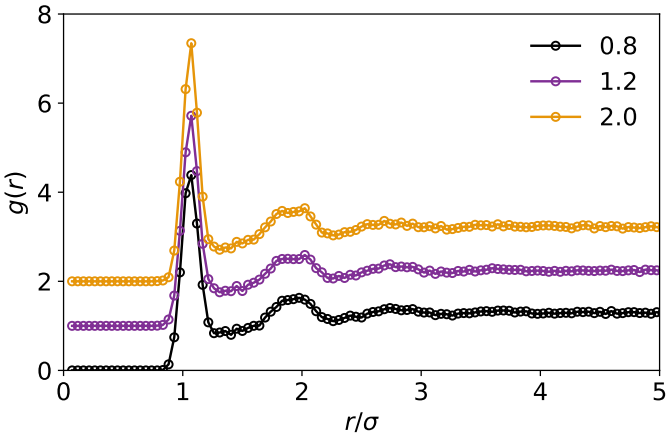

Fig. 5.7 Pair correlation functions $g(r)$ of colloid-polymer mixtures with three different polymer concentrations, the polymer volume fractions ϕ_p are 0.8 (black), 1.2 (purple) and 2.0 (yellow). In this figure, as polymer concentration increases, curves are shifted upwards for one unit each time for a better visualisation.

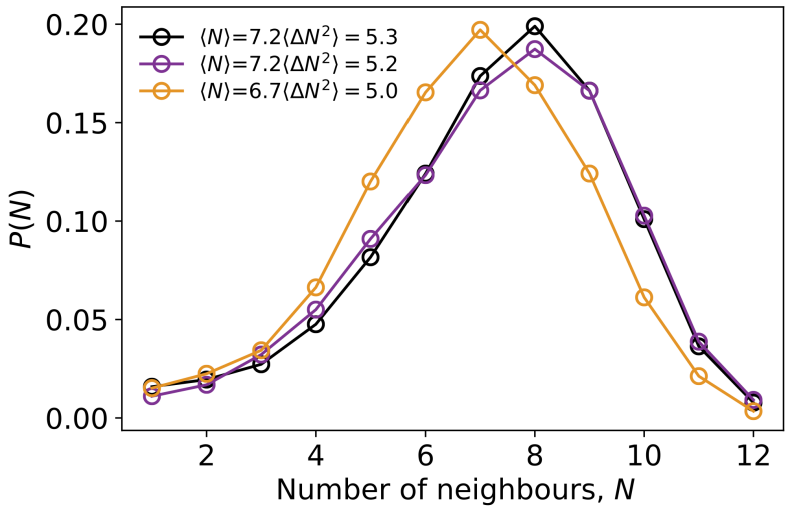

Fig. 5.8 Number of neighbours distribution of three colloid-polymer mixtures with polymer volume fraction ϕ_p of 0.8 (black), 1.2 (purple) and 2.0 (yellow).

less time to rearrange themselves, therefore the resulting structures are more similar to the structures of liquid and locally less packed.

From Fig.5.8, we also found the variance of the number of neighbours $\langle \Delta N^2 \rangle$ declines from 5.3 to 5.0 when we increase polymer concentration. The subtle narrowing of distributions suggests more homogeneous structures towards higher polymer concentrations.

Number of contacts

Rather than fixing a distance to find neighbours as in the calculation of number of neighbours, the number of contacts measures how many particles are directly in contact with the reference particle. Thanks to the fluorescence technique employed in our system, interdroplet contacts are able to be detected because contacts have higher fluorescent intensity than droplets in the confocal image. Using tracking method of interdroplet contacts, as described in section 2.6, the size and position of each contact is determined. Next we are able to find out if two droplets are in contact based on the positions of all droplets and contacts, further we can measure the number of contacts. The distributions of contacts of three gels are plotted in Fig. 5.9. The peaks of the two samples with lower polymer concentrations are both at 7, while the peak decreases to 6 for the highest polymer concentration. The contact numbers are all smaller than the corresponding number of neighbours as expected.

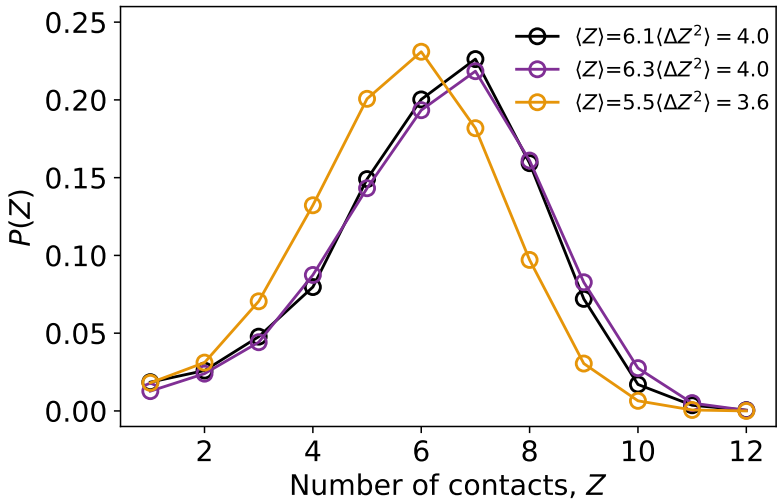

Fig. 5.9 The distribution of number of contacts of three colloid-polymer mixtures, with polymer volume fraction ϕ_p of 0.8 (black), 1.2 (purple) and 2.0 (yellow).

The average number of contacts $\langle Z \rangle$ for all samples are around 6, indicating isostaticity and rigidity developed in the system. The continuous drop of the average number of contacts $\langle Z \rangle$ and variance $\langle \Delta Z^2 \rangle$ are in consistent with the trend found in the number of neighbours, which confirm the fact that gel structures become looser packed and more homogeneous as being deeper quenched.

Topological cluster classification

Based on particle positions, local structures are identified in three gel samples by using the topological cluster classification (TCC) algorithm, as described in section 1.4.2. The TCC results are presented in Fig. 5.10, m shows the the number of particles that are contained in a local structure. The most populated cluster is tetrahedra ($m = 4$) which accounts for more than 80% for all samples. The structure accounting for the second largest population is triangular bipyramid with $m = 5$, around 70% particles are identified forming this structure. Local structures with $m = 7$ and 8 rank for the next largest population for about 20 to 35%. The structure with $m = 7$ is pentagonal bipyramid, the red particle in eight-membered structure is an additional particle from the structure of $m = 7$. Larger clusters are less populated, especially the structure with $m = 10$ which is called defective icosahedron, with three particles missing from an icosahedron. Only 5% defective icosahedron are found in all gels. The majority local structures are three and fivefold symmetries, only about 15% are found with fourfold symmetry.

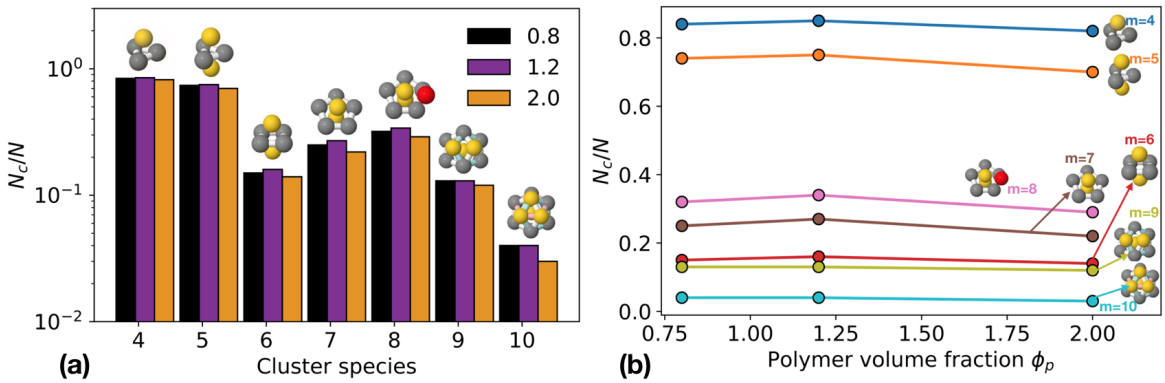

Fig. 5.10 Topological cluster classification analysis of of three colloid-polymer mixtures. (a) Populations of clusters with number of particles $m = 4$ to 10 in the three colloid-polymer mixtures. (b) The same data is plotted to visualise the change of cluster populations as polymer concentration increases.

As polymer concentration increases from $\phi_p = 0.8$ to 1.2, the population of local structures identified rises up first and then drops to lower population at $\phi_p = 2.0$. The reduction of local structures is compatible with the decrease of number of neighbours and number of contacts.

From structural analysis, we find there is decreasing of number neighbours, contacts and local clusters as polymer concentration increases. We infer that gels are more dynamically arrested as deeper quenched, structures have less time to rearrange to lower energy state, so that structures are more similar to the structure of liquid and more loosely packed.

5.3.3 Contact forces and stress fields

From confocal images of particle contacts, we tracked the positions of contacts. From these coordinates, we are able to compute interdroplet forces and further calculate the stress field and determine force chains for each colloid-polymer mixture. Contact forces measurements in this thesis are conducted only on the compressive force between droplets, tensile forces are not accessible using this experimental technique.

Probability distribution of contact forces

Different from granular systems, thermal energy plays an important role in colloid-polymer mixtures. In colloidal emulsions, droplets are dispersed in a liquid medium, therefore emulsions are considered frictionless, droplets interact with each other only through normal forces (no tangential frictional forces). Without participation of non-absorbing polymers and at low colloid volume fraction, emulsion droplets do not deform and no contacts can be observed under a confocal microscope. The addition of non-absorbing polymers induces effective attractions between droplets which results in repulsive interdroplet forces, higher fluorescent intensity is thus shown at contact points where droplets are under compression. The deformation can also be induced by applying external forces to the system, such as centrifuging and shearing the emulsions[3].

In the presence of non-absorbing polymers, unbalanced osmotic pressure pushes droplets together, inducing an effective attraction between droplets. [...] The deformation is small with respect to the droplet surface area, therefore the Laplace pressure of the droplet is considered unchanged during the deformation. All the energy from the compression is presumed to be stored as elastic energy in the deformation area. does the elasticity of the droplet (material/silicone oil) play a role in determining the force?

Although droplets deform under compression, the deformation is small with respect to the droplet surface area, therefore the Laplace pressure can be considered unchanged during the deformation. All the energy from the compression is presumed to be stored as elastic energy in the deformation area, at microscopic level, the interdroplet forces between two droplets with radii of R_1 and R_2 can be described by Princen force law[2]:

$$f = \frac{\sigma}{\tilde{R}} A \tag{5.1}$$

where A is the deformation area at contact, $\tilde{R}$ is the geometrical mean radius of the two undeformed droplets, $\tilde{R} = R_1 R_2/(R_1 + R_2)$, σ is the interfacial tension, which is taken as 9.2 mN/m between silicone oil and water-glycerol mixture, measured by Brujic with a similar system[76]. This force model has been applied to various systems to measure microscopic

forces, such as granular emulsions[76], and liquid droplets labelled with a monolayer of fluorescent nanoparticles or modified cowpea mosaic virus (CPMV)[78].

The number of particles tracked for each gel is 6114, 5387 and 5006, and number of contacts is 18765,16877 and 13796. From tracked contacts we obtain the size of each contact, by counting the number of voxels occupied by a contact. Each contact is allocated to adjacent two particles with radii R_1 and R_2. Using the Princen model described above as the microscopic force model, we calculated interdroplet forces in the system. The average force $\langle f \rangle$ is 5 nN corresponding to an area of 0.85 μm^2. All detected forces are scaled with the average force $\langle f \rangle$, the distribution of scaled forces is shown in Fig. 5.11(a) for three colloid-polymer mixtures. The distribution peaks at $f \approx 1.5\langle f \rangle$ and the maximum force is around 3 times of the average force. The probability of small forces is noticeably high and comparable to the peak value, then there is a subtle drop as the magnitude of forces increases. The high probability of small forces possibly comes from the noise of the system, *i.e.* a few number of residual pixels remained after intensity thresholding during the contact tracking, these pixels which have small area and high intensities may result from the emission overlap of dye molecules when two droplets are very close. However, it is not trivial to identify whether a small contact is a true contact or just noise in the system, therefore it is not certain that the dip at $f \approx 0.5\langle f \rangle$ is true.

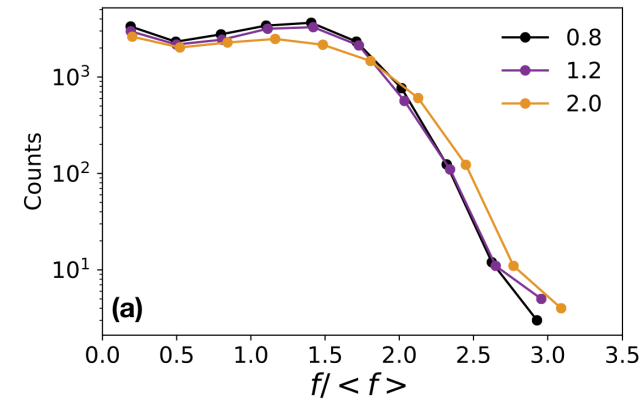

Fig. 5.11 Probability distribution of interdroplet forces f scaled with average force $\langle f \rangle$. (a) Force distribution of three colloid-polymer mixtures. (b-d) Force distribution and Gaussian fitting for each colloid-polymer mixture. The table shows Gaussian fitting parameters.

Without considering the small forces, the scaled force distribution can be fitted with a Gaussian distribution, in the form of

$$P(f/\langle f\rangle) = A \cdot exp[\frac{-(f/\langle f\rangle - \mu)^2}{2\sigma^2}] \tag{5.2}$$

The fitting of each gel sample is shown in Fig. 5.11(b-d), and the fitting parameters for three gels are presented in the table in Fig. 5.11. From Fig. 5.11(a), there is no obvious difference among three gels, except that the one with highest polymer concentration has a broader distribution. It is also indicated by the fitting parameters that value of μ is slightly higher.

Our results of force distribution which follows a Gaussian distribution is distinct from an exponential decay that is often observed in jammed granular matter. One form of the exponential decay is $P(f) \propto f^n exp[-(n+1)f/\langle f\rangle]$ where the coefficient n is of the order 1 and depends on the average number of neighbours[76]. A number of experimental, theory and simulations studies have shown that a plateau or peak at small forces, along with an exponential tail at large forces is the typical feature undergoing jamming transition. The exponential tail indicates the stress transmission in jammed materials is inhomogeneous[76, 134, 135].

However Gaussian distributions of scaled forces are also found in several cases. In one experimental system of athermal emulsions[76], the force distribution first shows a Gaussian distribution when the droplets are under creaming, *i.e.* the external force is only gravity. As the emulsions are centrifuged with increasing gravitational forces, at the order of several thousand g, exponential decay starts to show up, the system bears pressure around 4.4 Pa. However, as the centrifugation force keeps increasing, when the pressure is at the level of 5.5 Pa, the force distribution becomes Gaussian again. In molecular dynamics simulations of compressed emulsions, a deviation at large forces from exponential distributions is discovered as pressure increases for a polydisperse system, this deviation becomes Gaussian-like in a monodisperse system [76].

Molecular dynamics simulations on a binary supercooled liquid with LJR12 (purely repulsive Lennard-Jones potential) for a number a temperatures, from above the glass transition temperature T_g to below T_g were performed by O'Hern *et al*[4]. At high temperatures, $P(f/\langle f\rangle)$ decays exponentially. As cooling the system, a peak starts to show up in the distribution and the slop of the tail increases. Further dropping the temperature, the peak shifts to the right towards$\langle f\rangle$, and the shape of distribution behaves more like Gaussian rather than exponential[4].

In their simulations of supercooled liquids near glass and jamming transitions, as long as the interaction between particles are sufficiently hard, the distribution is not sensitive

to the form of potentials. The distribution peaks around the average force value means the majority of forces are at similar magnitudes, therefore forces in different directions are roughly balanced on a particle, leading to the formation of force chains. The forces at the peak correspond to separations near the first shell of the reference particles, *i.e.* the first peak of $g(r)$, they are among the slowest to relax. They also argue that the emergence of a peak in $P(f/\langle f\rangle)$ is a signature of the development of a yield stress. A percolated force chain or enough particles participating in forces chains assures stress transmission through the system, therefore the system behaves like a solid which has a yield stress[4].

Their simulations suggest that the peak in force distributions indicates the emergence of yield stress in the system and the system becomes 'solid'. This is in agreement of our force distribution results for the case of gels which are normally considered as 'semi-solid' materials. The peak also implies force chains developed in the system and we will also confirm the finding of force chains in colloidal gels in section 5.3.3.

Stresses and local pressures

The stress tensor, also known as force moment tensor, for each particle is calculated using equation 2.8 in section 5.3.3. For a given particle, we need to know the positions of particles that are in contact with the reference particle, and the positions and sizes of the corresponding contact area.

From each stress tensor, three eigenvalues are obtained which correspond to three principal stresses in different directions. Since droplets are deformed due to compression, the most compressive stress of a particle is the minor principal stress, *i.e.* the most negative value among the three eigenvalues. The trace of a stress tensor which is the sum of the three principal stresses yields the quantitative pressure measurement on a particle. The distributions of the most compressive stress and particle pressure are presented in Fig. 5.12 and Fig. 5.13 respectively. The negative values in the most compressive stress indicate the interdroplet forces are experiencing repulsions from contacting particles.

Different from the distribution of $P(f/\langle f\rangle)$ which is Gaussian-like, the shapes of distributions of the most compressive stress and pressure are more similar to exponentials.The dip at small forces also disappear in the stress distributions. The range of the distribution is up to 4 times of the peak value which is wider compared with that of the force distribution. This implies a wider range of stresses in the system than the range of forces. From Fig. 5.12 and Fig. 5.13 we cannot identify difference among the three state points.

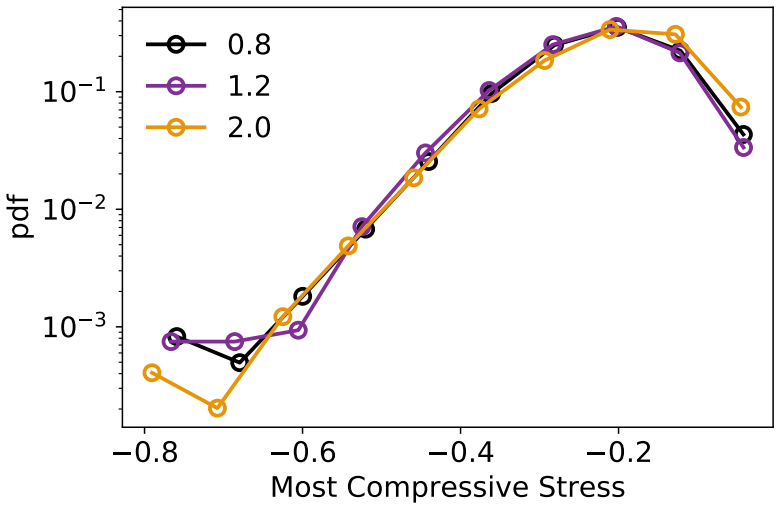

Fig. 5.12 Probability distribution of the most compressive stress in colloid-polymer mixtures.

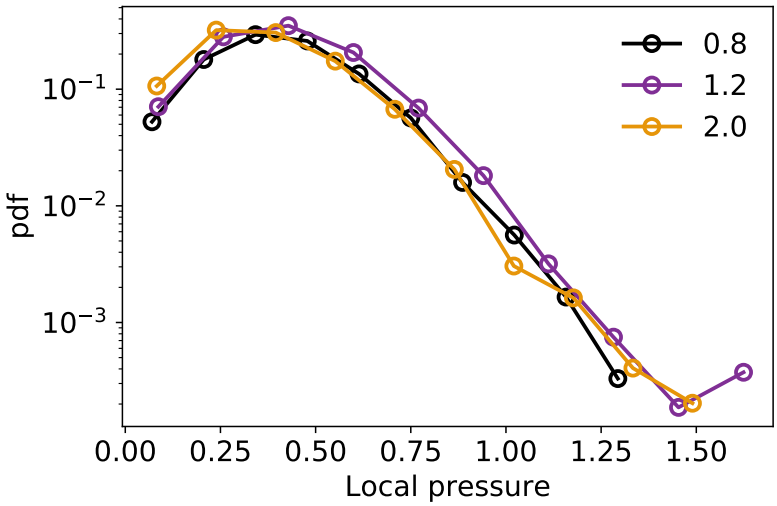

Fig. 5.13 Probability distribution function of local pressures in colloid-polymer mixtures.

Force chains

Following the method described in section 2.7.1, we detected force chains in all three colloid-polymer mixtures, based on the most compressive stress on each particle. Particles participate in force chains are rendered in Fig. 5.14 while other particles which do not form force chains are not shown. Force chains are where contact forces strongly localised and are the main stress carrier in the system. Each particle in a force chain often has two major load bearing contacts which are roughly balanced.

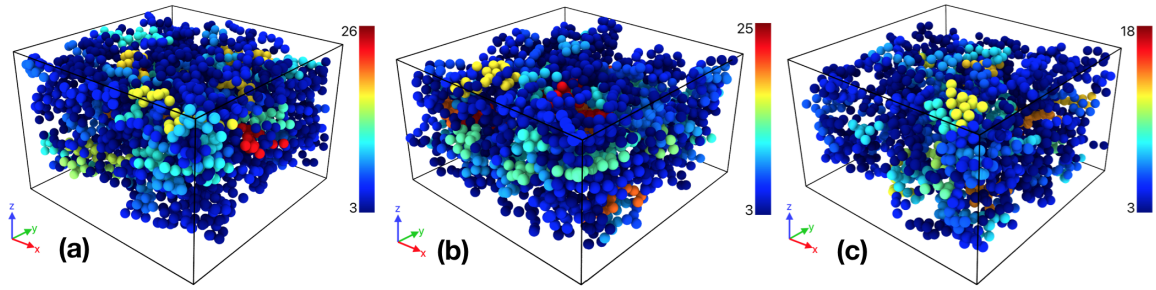

Fig. 5.14 Rendering of force chains detected in three colloid-polymer mixtures with polymer volume fraction ϕ_p, (a) 0.8, (b) 1.2 and (c) 2.0. Colourbars indicate lengths of force chains measured in terms of the number of particles, particles labelled in red imply they participate in long chains, while blue color is short chains.

In the rendering pictures, the direction of gravity is upwards, therefore droplets in the box have the tendency to move downwards. From the colourmap we can see that most force chains are rendered in dark blue which means they are only in short force chains, with chain length less than 10 particle diameters. Only a few long chains are found and they are located close to the centre of the samples. This can be better viewed in Fig. 5.15 where force chains are shown having length at least 8 particle diameter. It is also evident that in the gel sample with highest polymer concentration (Fig. 5.15(c)), there fewer force chains detected and also they are shorter compared with the other two samples.

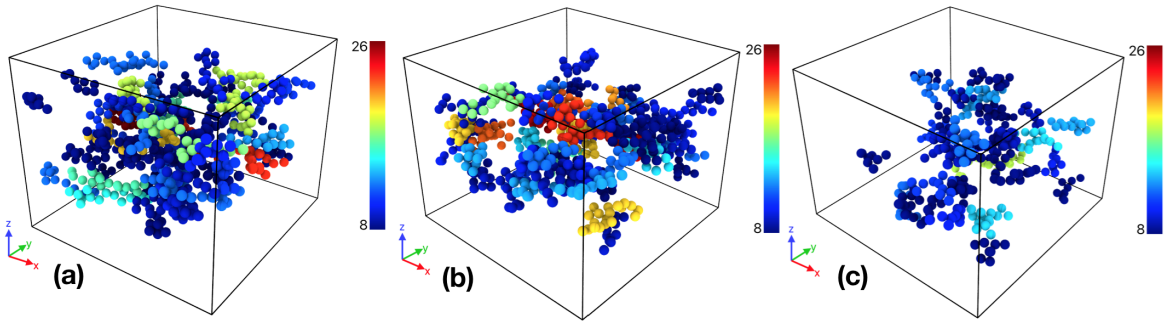

Fig. 5.15 Rendering of force chains with length at least 8 particle diameter in three colloid-polymer mixtures, with polymer volume fraction ϕ_p, (a) 0.8, (b) 1.2 and (c) 2.0.

The probability distribution of length of force chains of three colloid-polymer mixtures is plotted in Fig. 5.16. The distributions all decay exponentially for three gels. The longest force chain detected is 26, 25 and 18 particle diameters as polymer increases, therefore the distribution of the highest polymer concentration decays fastest among the three samples. It is obvious that no percolating force chain is found in any of the gels, but the gel itself is a percolating network. This is again distinct to many scenarios in jammed granular systems,

where percolating force networks are detected to transmit stresses through the system and maintain the mechanical stability[5, 150].

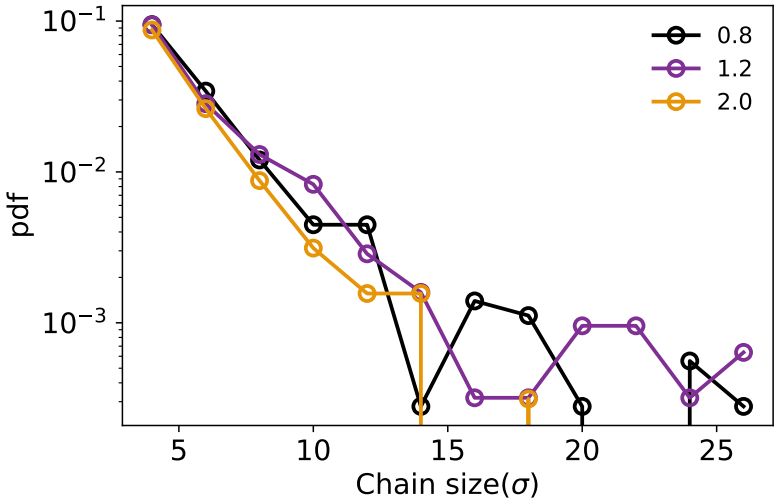

Fig. 5.16 Probability distribution function of length of force chains. The length is characterised in terms of the number of particle diameters.

The number of particles in each sample is 6055, 5346 and 4937, particles at edges which are less than a particle diameter to the box are not taken into account. The number of particles participating in force chains in each sample is 2707, 2435 and 1818, and this results in percentages of 45%, 46% and 37%.

At the highest polymer concentration, there are fewer particles forming force chains, the longest chain is also the shortest among three samples. We would expect with higher attraction strength, particles are experiencing higher pressures, thus the magnitudes of forces are also larger with more contacts. However, the structure of the deep quenched gel is more dynamical arrested and similar to liquid structures, along with a slightly lower colloid volume fraction, there is less neighbours and local clusters in the deep quenched gel. This in turn reduces number of contacts and therefore fewer particles will assemble in force chains.

5.3.4 Correlations of structures with contact forces

After resolving the structural and mechanical properties separately, we also perform analysis on examining the correlations of local structures (TCC clusters) with stress fields and force chains in these gels.

TCC and stresses

From Fig. 5.13 we know the statistics of stress distribution in each colloid-polymer mixture. However this is the result which represents the average of the ensemble thus cannot present local behaviours in the sample. We further investigate the role played by local structures in stress distributions by only plotting the local pressure distributions in each species of clusters, from m= 4 to m= 9, in the gel sample with the lowest polymer concentration ϕ_p = 0.8. The plot is shown in Fig. 5.17. It is clear that all curves share the same peak value, decay exponentially but with different exponents. As the size of cluster increases, from m= 4 to m= 9, the tails decay slower indicating a higher percentage of strong stresses carried by particles in large clusters, so that large clusters are the main load bearing components in the gel.

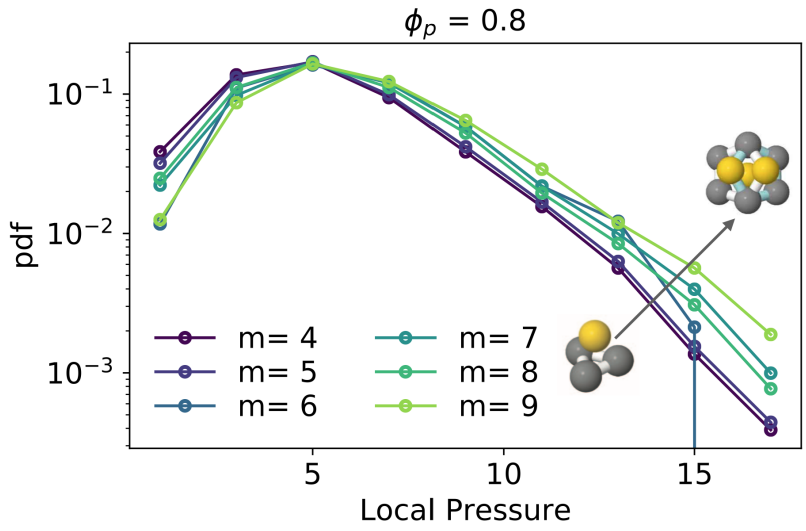

Fig. 5.17 In the colloid-polymer mixture with ϕ_p = 0.8, the probability distributions of local pressure of particles that form different minimum energy clusters from m= 4 to m= 9.

Having a primary assumption of the roles played by different clusters in terms of carrying stresses, we further examined how does it vary with attraction strengths in colloid-polymer mixtures. Hence in each subplot in Fig. 5.18, we find particles that participate in a certain minimum energy cluster, for each colloid-polymer mixture, and plot the local pressure distributions in these particles.

From Fig. 5.18 (a) and (b) we can see that particles participating in small clusters such as m = 4 and 5, the local pressure distributions have similar shapes to that of the average distribution as shown in Fig. 5.13. The distributions all peak at a small value and decay exponentially. The significant similarity is due to the fact that m = 4 and 5 account for the largest population of local structures, their behaviours dominate the total behaviour of the sample.

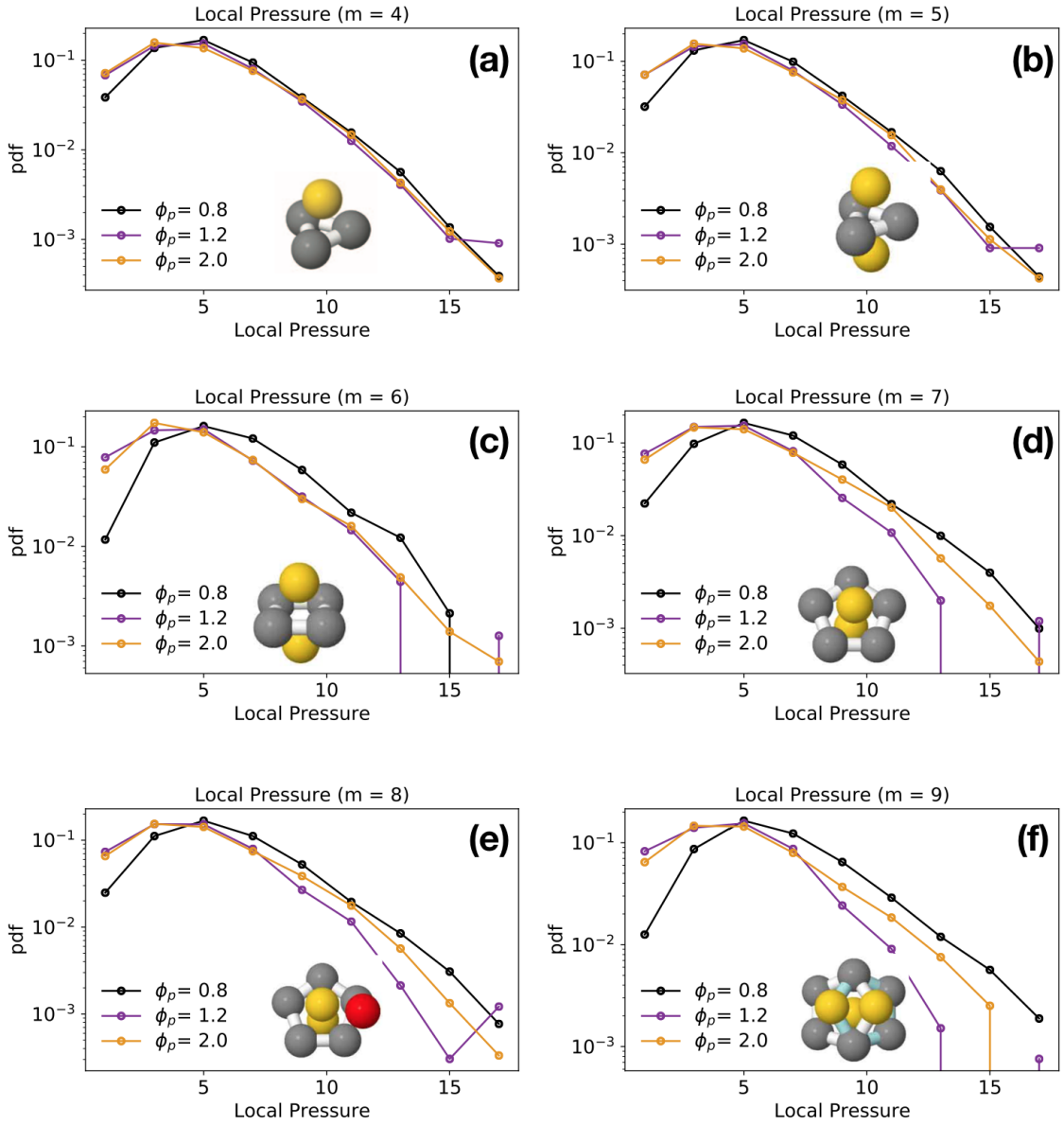

Fig. 5.18 Probability distributions of local pressure of particles that participate in a particular local structure with (a) $m = 4$, (b) $m = 5$, (c) $m = 6$, (d) $m = 7$, (e) $m = 8$, (f) $m = 9$ particles. Each subplot is for a specific cluster in three colloid-polymer mixtures.

When looking at the behaviours of larger clusters, with $m = 6$ to $m = 9$, as presented in Fig. 5.18 (c) - (f), we find there is increasing deviation of distributions for different polymer concentrations as the size of the cluster grows. Two gels with higher polymer concentrations peak at a lower local pressure compared with the one with lowest polymer concentration. The decay of the distribution at large values becomes faster as increasing polymers. The faster

decays and narrower distributions indicate that stresses are located more homogeneously in particles which form large clusters.

In three gels with different attraction strength, stresses stored in small clusters are comparable. In comparison, as polymer concentration in gels increases, stresses are distributed more homogeneously among large clusters. This may imply that stresses in large clusters relax or transmit quickly in the gel with the most attraction strength, or the more homogeneous distribution originates from the fact that slightly fewer local structures are identified with higher polymer concentrations, as stated in section 5.3.2.

We infer that large clusters are the load bearing components in the system. As polymer increases, we find that there are fewer large clusters, so that the number large force carriers decreases. Because there are not sufficient large clusters to carry large forces in the sample with high polymer concentration, resulting in a faster decay in stress distribution and a more homogeneous stress distribution.

TCC in force chains

In the previous section, we discussed the correlations between TCC clusters and stresses in particles. Since particles bearing high stresses have the ability to transmit stresses and form force chains, we also conduct the analysis of the correlations between local structures and force chains.

In Fig. 5.19 (a), the bar plot shows the percentage of number of particles that participate in local minimum energy clusters which are detected by the TCC algorithm. The values of bars on the left are calculated by dividing the number particles forming each type of cluster N_C by the total number of particles N^{all}. This part of the plot shows the same result as partially indicated in Fig. 5.10: small clusters with $m = 4$ and 5 account for most of the local structures. In the same plot, bars with hatched markers on the right, take account of only particles and clusters located inside force chains. The number of particles forming force chains and clusters is N_C^{Chain} while the number particles only participating in force chains is N^{Chain}. There are less than 50% particles found in forces chains (discussed in section 5.3.3). The percentage of particles forming local structures and also participate in chains increases of all cluster species, as can be seen from Fig. 5.19 (a) that bars with hatched markers all have larger values than the bars with the same color. Since particles in force chains are high stress carriers, a higher percentage of clusters in force chains means local structures play a significant role in transmitting stresses and carrying stresses in the system. This is not surprising because these local structures are minimum energy clusters and they are therefore locally rigid clusters. It is their geometrical properties and interaction potential that determine they should be large stress carriers and have higher chance forming force chains.

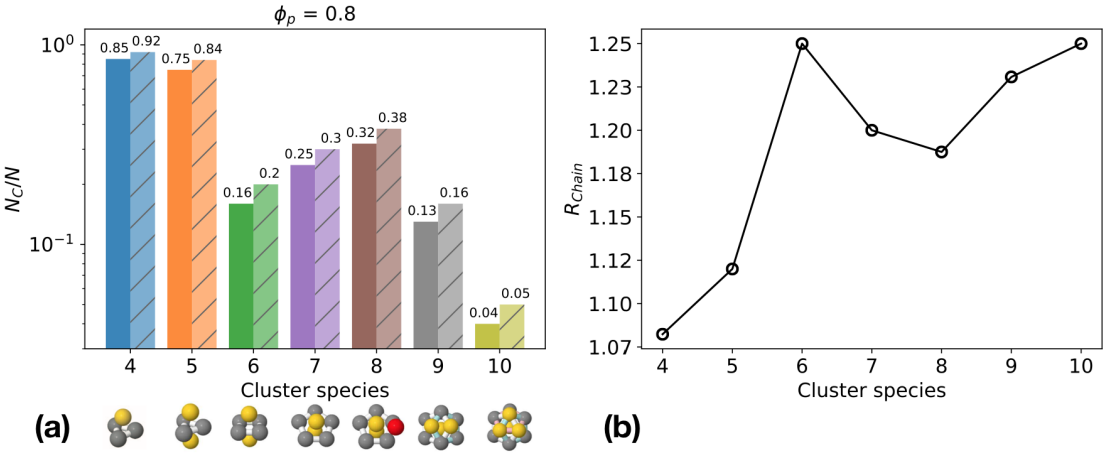

Fig. 5.19 (a) Bar plot of TCC cluster population in the colloid-polymer mixture of $\phi_p = 0.8$ and cluster population of particles forming force chains. (b) The ratio R_{Chain} of TCC cluster population of particles forming force chains to the population of total particles, for each cluster species from $m = 4$ to $m = 10$.

We further quantify how much the number of local structures for each species increases. We use the value of R_{Chain}, which is defined as $\frac{N_C^{Chain}/N^{Chain}}{N_C/N^{all}}$, and R_{Chain} is plotted for each cluster in Fig. 5.19 (b). We see a general increasing trend for R_{Chain} as the size of local structure increases. This may due to the fact that the percentage of large clusters is relatively low for both conditions: particles participate in force chains or not. The increase becomes more obvious when the original value is small. Alternatively, a higher increase in large clusters means they are more likely to participate in force chains or carry large stresses compared with small clusters. In this section we only show the data for colloid-polymer mixture at $\phi_p = 0.8$, the results of the other two samples with $\phi_p = 1.2$ and 2.0 are comparable.

5.3.5 Summary

By using a fluorescence technique with a solvatochromic dye, we measured normal forces between droplets in colloidal gels. We reported analysis of three colloid-polymer mixtures with various polymer concentrations, *i.e.* various attraction strengths. All colloid-polymer mixtures are quenched below the gelation temperature. We obtained particle and contact positions by performing particle tracking on real-space 3D confocal images. Based on these coordinates, we examined the structural and mechanical behaviours of three gels at microscopic level, what we found are listed below.

We scaled the distribution of interdroplet forces is scaled with the average force $\langle f \rangle$, which is around 5 nN. The scaled distribution has a dip at $0.5\langle f \rangle$, peaks at a value around

$1.5\langle f \rangle$ and then decays following a Gaussian distribution. This type of distribution is found in jammed system with relatively higher external pressures, while at lower pressures the force distribution decays exponentially.

The shape of the scaled distribution does not significantly vary with the change of polymer concentrations. It only becomes broader at the highest polymer concentration, indicating a subtle increase in the heterogeneity of force distribution. There is no difference identified for the distributions of the most compressive stress and stress trace of the three colloidal gels. They are unimodal and decay exponentially, they also have a wider range compared with that of the force distribution.

The subtle difference in force and stress distributions originate from their similar structural properties. We found the pair correlation function $g(r)$ of the three state points are almost identical, but both the number of neighbours N and contact number Z decrease slightly with increasing polymer concentrations. This also leads to a decrease in the number of local structures identified.

Stresses are transmitted through force chains. We do not find percolating force chains in any colloid-polymer mixture although the gel network itself is percolated spatially. The longest chain has a length of 26 particles in the sample of the least quenched gel. The distribution of lengths of force chains also decays exponentially.

Finally we investigated the correlation between local structures and stresses. We found the stress distribution in each species of local structure decays slower as the size of cluster increases, meaning that large clusters are carrying relatively large stresses. The percentage of number of clusters identified in force chains is also higher than the fraction in the whole system, showing that local structures play an important role in stress transmissions.

Chapter 6

Contact Forces Measurements of A Creaming Colloidal gel

6.1 Introduction

In a colloid-polymer mixture, a transient gel is obtained when the non-absorbing polymer concentration is sufficiently high so that the colloid-rich phase formed by spinodal decomposition becomes space-spanning networks (detailed descriptions in section 1.3). Although a colloidal gel attains a finite shear modulus and thus makes it possible to support its own weight under gravity, the timescale for a gel being stable is often finite and varies for different conditions of gels[151].

There are two types of settling behaviours. At low and intermediate polymer concentration above the gel boundary, gels undergo delayed sedimentation or delayed collapse, which contains two distinctive two-stage time-dependent settling processes. The defining characteristic of this behaviour is the presence of a delay time τ_d during which little or no settling is observed, the gel can resist compaction. When the gel age t_w is greater than the delay time, a sudden onset of a rapid sedimentation happens and we can also say the gel collapses.

At high enough polymer concentration, a creeping sedimentation behaviour was found, and rapid collapse was no longer observed. In creeping sedimentation, the structural integrity does not change in a dramatic way like the one in delayed collapse, structures are compressed in a more or less homogeneous fashion, without clear local disruptions to the network structures[152]. The sample dimensions are also important, collapse only happens when the sample sizes are larger than some characteristic size intrinsic to the gel[152–155].

Both settling behaviours are mechanical instability of gels, especially in the case of the sudden collapse, there is no indication before the gel fails. This significantly limits the shelf life of many formulation products of colloidal gels such as pesticides, and it is challenging to correctly predict the delay time before collapsing. It is therefore crucial to understand the mechanism of gel collapse which provides information to build stronger colloidal gel networks and increase the shelf life of commercial products. A number of studies have been carried out to study gel collapse, techniques that are most commonly used are time lapse imaging, confocal scanning laser microscopy which can reveal gel structures at both bulk and microscopic levels, while rheometers are employed to probe the rheological properties of gels.

6.1.1 Gel collapse phenomenon

In a colloid-polymer mixture, during the process of gel collapse, the height h of the interface between the gel and supernatant normalised by the height of the sample cell h_0 is plotted in Fig. 6.1 (b)[153]. During the initial delay time or lag period (I), there is no change of the interface height, the gel fulfils the whole sample cell homogeneously. This shows the gel can support its own weight and is a mechanically stable solid, but only for a limited time period τ_d. When the waiting time is longer than τ_d, the gel network yields and a clear interface starts showing up, as shown in Fig. 6.1 (a). The interface velocity v increases smoothly as the gel collapses (the slope of the interface profile increases in Fig. 6.1 (b)) and the gel shrinks more rapidly. The collapse stage (II) ends when liquid-gas phase separation is almost completed and the interface reaches the final equilibrium plateau. After the collapse period, the gel falls into the final consolidation stage (III), the sedimenting velocity drops dramatically as the gel continues to slowly compress like a solid under its own weight[153].

Rheological measurements of colloid-polymer mixtures with long-range attractions have shown some elasticity in the gel at short time scales during the lag stage, the elastic modulus then decays to zero at long times which means the gels becomes liquid-like after collapsing[156].

6.1.2 Microstructure during gel collapse

Using confocal microscopy, Teece *et al*[156] found gel network structures are coarsening under gravity, as shown in Fig. 6.2. The characteristic domain size $R_c(t)$, which is calculated using the expression, $R_c(t) = \pi/\langle q(t)\rangle$ where $q(t)$ is the structure factor, stays constant at short times *i.e.* during the delay time. When the gel starts to collapse, the domain size grows with a power law scaling, $R_c(t) \sim t^{\theta}$. The exponent θ strongly depends on the quench depth,

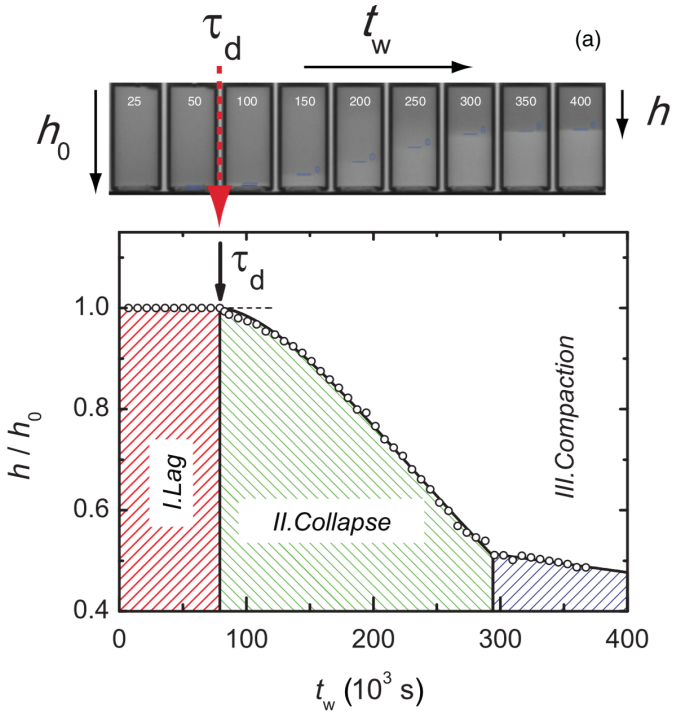

Fig. 6.1 Sudden collapse of a gel. (a) Time-lapse images of a colloid-polymer mixture as a function of the time after preparation. The mixture has colloid volume fraction $\phi = 0.21$, and polymer concentration $c_p/c_p^* = 3.6$. The time elapsed t_w is labelled on each image in units of 10^3s. The height of sample cell also the initial height h_0 of the sample is 40 mm. The red arrow indicates at characteristic delay time τ_d, the network starts to collapse. The solid line shows the interface between the colloid-rich (upper) and polymer-rich (lower) phases. (b) The normalised height h/h_0 of the gel as a function of the elapsed time which shows three characteristic settling stages of gel sudden collapse[153].

it decreases with higher polymer concentration, which means gels coarsen slower when deeper quenched. The point when the gel starts to collapse is also when anisotropy emerges in the system, gravity stretches the characteristic domains along the gravitational z-direction, as can be seen from images at 4200 s and 7200 s in Fig. 6.2.

In the study by Starrs *et al*[152] using dark-field microscopy and a non-intrusive ultrasonic technique, they found during the delay time, the particle density remained constant and homogeneous throughout almost the whole height of the sample. Some macroscopic features are discovered during this period, such as channelling and streamer formation. These features only cause local breaking of the gel but do not trigger immediate large-scale collapse suggesting that the gel can initially support such local macroscopic restructuring.

During the settling process, they argue that the formation of 'channels' provides routes for solvent to travel upwards to the surface of the gel. The flowing solvent can tear free particles from edges of networks and carry these particles to the top of the gel. This in turn widens the

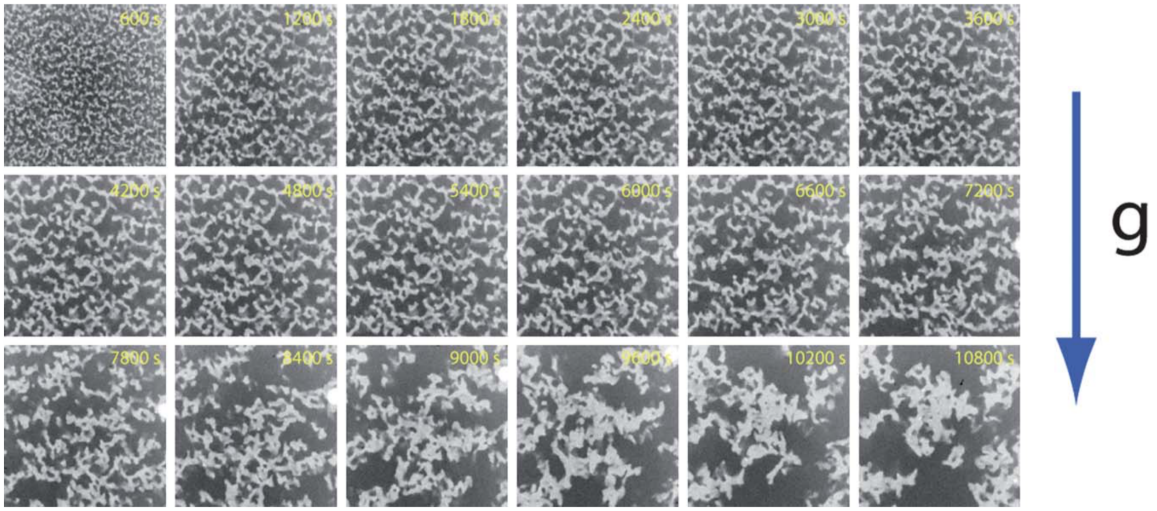

Fig. 6.2 Confocal images of coarsening and collapse of a gel formed in a colloid-polymer mixture with $\phi = 0.2$ and $c_p/c_p^* = 1.98$. All images are in yz directions, with gravity pointing downwards. Numbers on images are the observing time from the moment the mixture was prepared, the size of each image is $146 \times 146 \mu$m [156].

channel and increases solvent flow. The gel structure is able to tolerate such macroscopic disturbances for only a finite period of time. They discovered that gel always breaks from the top of the cell, which might due to the upward of flowing solvent destabilise the gel structure at the top. It is the formation of streamer-like features and rapid propagation of these streams that triggers large-scale flow and circulation which results in the gel collapse[152].

They also claim that above a characteristic lengthscale of the gel, the properties including the delay time do not depend on the initial height and width of the sample. If smaller than this size, gel is sensitive to the system size. Above this lengthscale, stresses are not transmitted in the gel network, the gel settled at a terminal velocity. By contrast, if stresses are transmitted through the whole gel network and cell walls, the gel might be supported by the walls and leading to size-dependent properties[157].

6.1.3 Microscopic model of collapse

Being able to predict the delay time of a colloidal gel helps take full advantage of the gel before it fails. However, the delay time varies from minutes to months, many factors will affect the delay time such as the range and strength of the attractive potential, the particle volume fraction, the size of particles, the density mismatch, external shear stresses, and also the dimensions of the sample cell[158].

In the study of gel collapse of emulsion-polymer mixtures by Bartlett *et al*[153], they discovered that the delay time τ_d strongly depends on the attraction strength and found expo-

nential relationship with the polymer concentration, $\tau_d \sim exp(c_p/c_p^*)$ when other parameters are fixed.

A microscopic model was proposed in order to connect the kinetics of bond-breaking to gel collapse[158]. During the ageing process, bonds between particles dissociate and associate continuously due to thermal fluctuations and external stresses such as gravity. The rate K_D of breaking of a gel strand is independent on time whereas the rate of association K_A decreases approximately linearly with waiting time t_w, $K_A(t_w) = K_A^0 - \alpha t_w$, where K_A^0 is the association rate when the gel is just prepared. The delay time τ_d is determined by the time-scale at which the rate of strand association becomes comparable to the rate of strand dissociation which means $K_D \approx K_A$. The application of a small perturbation force f, the activation energy for bond dissociation is increased by a factor of $f \cdot \Delta$, where Δ is the range of the attractive potential. They found the dissociation rate becomes

$$K_D(f) = K_D(0)exp(-\frac{f}{f_{th}}) \tag{6.1}$$

where $f_{th} = k_B T/\Delta$ is the force for a bond to rupture by thermal energy, and $K_D(0)$ is the dissociation rate without external forces[159].

Without external forces, the delay time $\tau_d(0) = (K_A^0 - K_D(0))/\alpha$. When the external force is weak ($f << f_{th}$), τ_d remains close to $\tau_d(0)$[158]. As the force f increases, the dissociation rate $K_D(f)$ decreases (calculated from equation 6.1), the delay time τ_d will therefore increases. If the force f is much larger than f_{th}, $K_D(0) = 0$ and τ_d reaches at its maximum value $\tau_d = K_A^0/\alpha$. When the waiting time $t_w = \tau_d$, any dissociation event will cause the gel to collapse immediately. From the microscopic model, they conclude that collapse is triggered when the rate of strand association K_A, which is a decreasing function of time, decreases to a value comparable to the fixed rate of strand dissociation K_D. Consequently, a catastrophic loss of connectivity is ultimately responsible for delayed collapse. However, how forces are propagated through the gel via each particle is unclear, and it has strong relation with bond formation and dissociation[158].

All studies of gel collapse bring out the point that finding out the force and stress transmissions provide further information for understanding the mechanism of gel collapse. In this chapter, we present the study of contact force distributions and structures of one colloid-polymer mixture which is quenched below the gelation temperature. We show the evolution of structural and mechanical properties of the colloid-polymer mixture during the process of creaming under gravity which is an opposite response of sedimentation. Our study gives the first analysis of the mechanical response of colloidal gels at microscopic

level and therefore it is instructive for understanding gel failure process and designing robust formulation products of gels.

6.2 Experimental methods

The preparation of the colloid-polymer presented in this chapter is the same as described in section 5.2. We select the gel sample with the highest polymer concentration described in Chapter 5, which is 1.89 gL^{-1} corresponding to polymer volume fraction ϕ_p of 2.0. The density of synthesized PDMS oil droplets is approximately 0.97 g cm^{-3}, and the refractive index matched aqueous phase which is a mixture of 51 wt% water and 49 wt% glycerol has density of 1.26 g cm^{-3}. Therefore the density mismatch between two phases $\Delta\rho$ is 0.29 g cm^{-3}.

The characterisation of gels with confocal microscopy is also using the same parameters, except the measurements were taken for a longer time. The gel was observed under confocal microscope 5 min after a gentle mixing on a roller bank, this time window corresponds to 16 τ_B. Each confocal 3D stack has dimensions of 512 $\times$ 512 $\times$ 451 (xyz) pixels. The time of taking one 3D stack is approximately 19 min, with Line Averaging of 32 and scanning two channels in a sequence by frame fashion. Since there is no waiting time between two time frames, the time interval Δt for two time frames is 60 τ_B.

6.3 Results and discussion

6.3.1 Structural analysis

We investigate structural evolutions of the colloid-polymer mixture undergoing a creaming process, by looking at their pair correlation functions, distributions of coordination numbers and number of contacts, and populations of topological cluster classification (TCC) clusters.

Density profile

Confocal images of gel contacts at different times during the creaming process are shown in Fig. 6.3. These images are in *yz* plane, vertical direction represents the direction of gravity. Since the density of silicone oil is less than that of water and glycerol mixture, oil droplets will cream as we can see from 6.3 that droplet networks are moving up.

The first image t_0 is taken at 19 τ_B, t_n = 19 τ_B + n $\cdot$ 60 τ_B. The inhomogeneous distribution of droplets in frame t_0 is due to droplet creaming, during the waiting time of sample cell drying and confocal microscope setup. Droplets cream relatively to the top of the sample

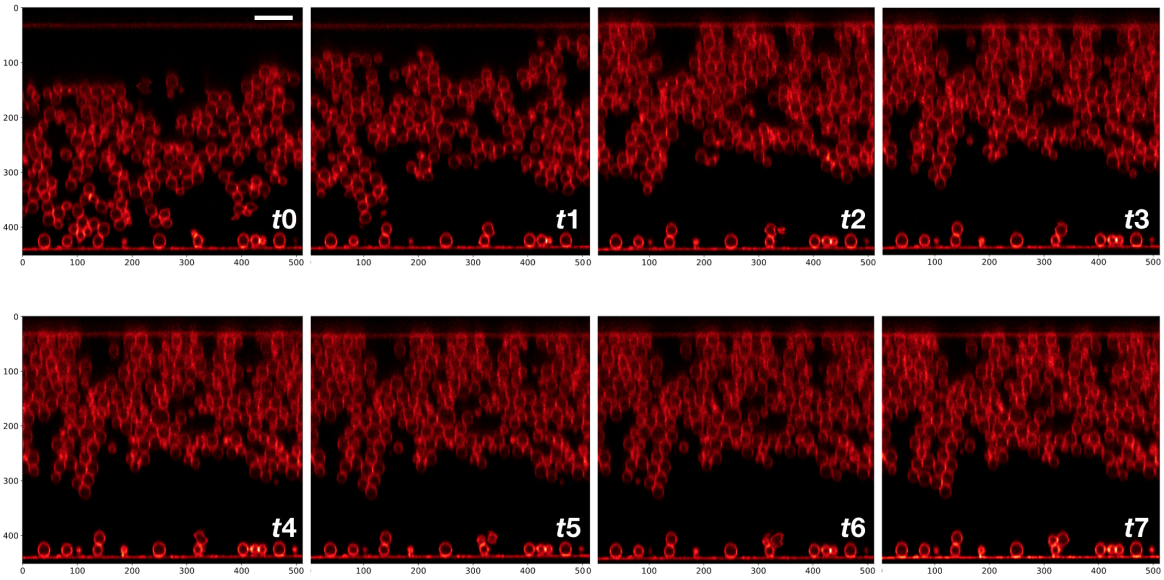

Fig. 6.3 Confocal images in yz directions of gel contacts under creaming, the height of the sample cell is 58 μm which is about 18 droplet diameters. The time frame t_0 is at 19 τ_B after gel preparation, during this time, the gel already starts creaming. The lens in the microscope is inverted, therefore the creamed gel appear at the bottom after inverting the sample cell, causing the gap at the top of the sample cell at t_0. The time interval between two time frames is about 19 min (60 τ_B), so t_n = 19 τ_B + n · 60 τ_B. Scale bar is 10 μm, numbers on the axes represent index of pixels.

cell, at $t_0 = 19\tau_B$. When placed on the microscope sample stage, the sample cell is flipped upside down, because the microscope we employed is inverted. Droplets are therefore near the bottom of the sample cell as shown in the first frame in Fig. 6.3 We show here 8 different time frames from t_0 to t_7, it is clear that the gel only has limited change in structures from t_3. Therefore in this chapter we will only present analysis of time frames at t_0, t_1, t_2 and t_5.

We performed particle tracking on confocal images of all time series, based on the coordinates, the density profiles of three time frames are plotted in Fig. 6.4. The density profile of a gel is the plot of local particle volume fraction at different height (z axis) of the sample. With the height of the sample cell being H, the top of the sample cell has z/H = 0 whereas at the bottom $z/H = 1$. From t_0 to t_5, droplets cream gradually to the top of the cell due to the density mismatch with the aqueous phase. At t_5, droplets only occupy 60% volume of the cell, with local volume fraction around $\phi_c^{local} = 0.45$ while the global volume fraction of the sample is $\phi_c = 0.23$.

Pair correlation function

The pair correlation functions $g(r)$ of the gel are plotted in Fig. 6.5 for these 4 time frames explained in the previous section. As the gel is undergoing creaming, we can see that the

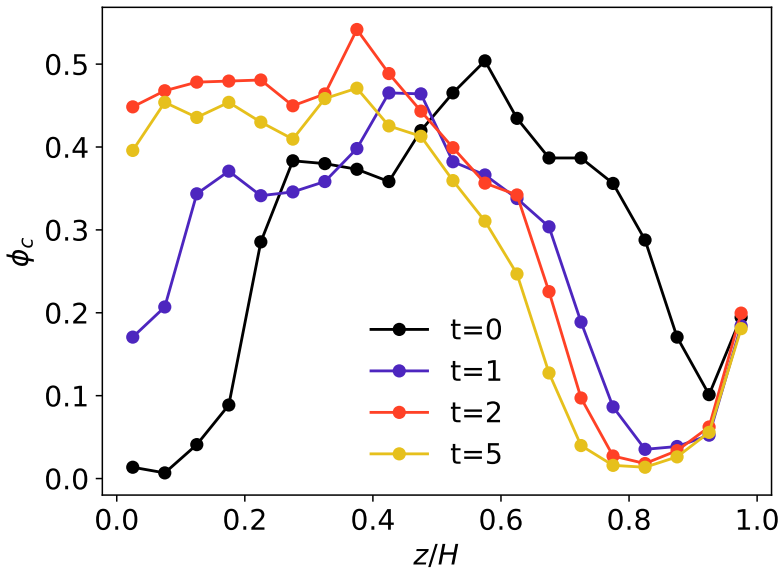

Fig. 6.4 Density profile of the gel in z direction during creaming. The height of the sample cell is H, at the top of the sample cell, $z/H = 0$ whereas at the bottom $z/H = 1$.

height of the first peak decreases slightly, the position of the first dip and second peak shift to the right. A pronounced first peak is the sign of a gel structure. The decrease of the first peak implies that structural features of networks are vanishing in the system, it is less likely to find a neighbouring particle within the first shell. It is also possible that at later times, the increase of local packing fraction makes particle tracking more difficult. There are more particles that are not tracked and further resulting in the decrease of the first peak.

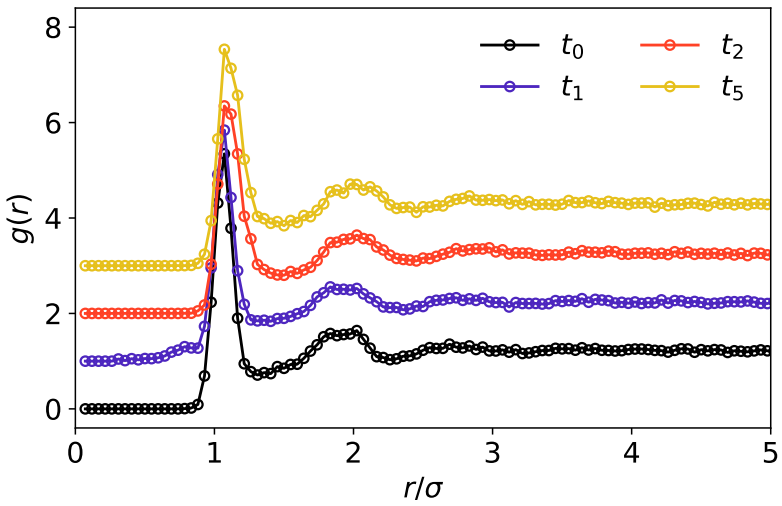

Fig. 6.5 Pair correlation functions $g(r)s$ of the gel during creaming.

Number of neighbours and contacts

The distributions of number of neighbours are shown in Fig. 6.6. The peak value of the distribution increases from N_{peak} =7 at t_0 and t_1 to N_{peak} =8 at t_2 and t_5. The variance of all distributions $\langle \Delta N^2 \rangle$ stay around 6, the skewness becomes more negative as the waiting time increases, this means at later times a large fraction of particles are having more neighbours than early times. The increase of neighbours might due to the increase of local packing fraction during creaming, which can be seen from the confocal images and density profile (Fig. 6.3 and Fig. 6.4). However all these subtle changes do not alter the average number of neighbours $\langle N \rangle$ over the time period of creaming, $\langle N \rangle$ = 7 for all time frames.

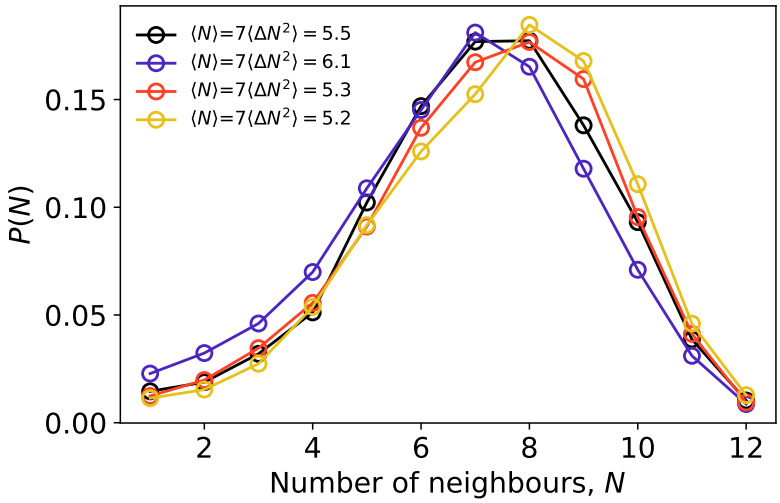

Fig. 6.6 Distributions of number of neighbours of the gel during creaming. Distributions at different time frames: t_0 (black), t_1 (blue), t_2 (orange), and t_5 (yellow).

Similar to the distributions of number of neighbours, there is no obvious variations in the distribution of number of contacts during gel creaming, as plotted in Fig. 6.7. The average contact number $\langle Z \rangle$ and the peak value of the distributions are both 6. This is the number required for a system to be in isostatic mechanical equilibrium in 3 dimensions[160]. The shape of the distributions also does not alter with time. The variance of the distribution $\langle \Delta Z^2 \rangle$ stays between 4.0 and 5.3, without noticeable skewness.

The steady distributions of both number of neighbours and contacts indicate that although the absolute positions of gel particles are shifted upwards under creaming, the global structure of the gel does not evolve significantly.

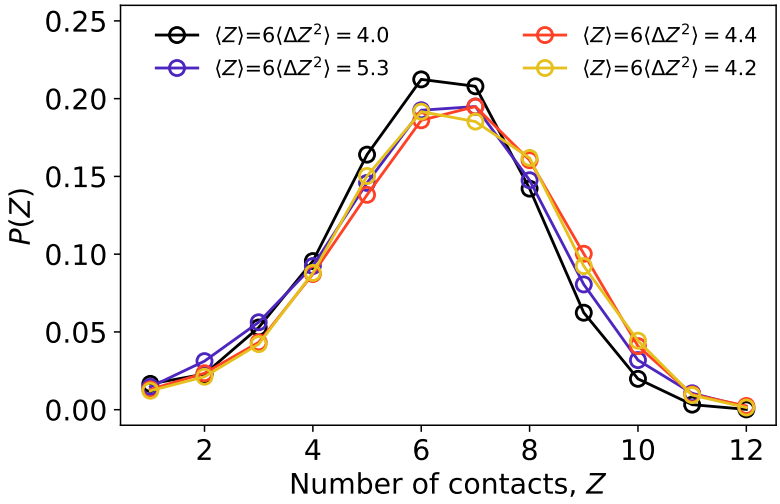

Fig. 6.7 Distributions of contact numbers of the gel during creaming. Distributions at different time frames: t_0 (black), t_1 (blue), t_2 (orange), and t_5 (yellow).

Topological cluster classification

To further investigate the structural change over time, we plotted populations of TCC clusters detected in each time frame, as shown in Fig. 6.8. From Fig. 6.8(a) we can see the majority of local structures identified are small clusters, with number of particles $m = 4$ and 5. These two populations account for about 80% of the total number of particles in the gel. The low population of cluster with $m = 6$ which has fourfold symmetry, indicates the system is far from crystallising. Because local structures with fourfold symmetries are the basic building blocks for crystal structures such as BCC or FCC. The largest cluster with $m = 10$ which is a defective icosahedron has the lowest population. Large clusters such as defective icosahedra are more likely to be identified in systems with higher volume fractions such as colloidal glasses or supercooled liquids.

From the plot of the change of cluster populations as a function of time (Fig. 6.8(b)), we do not see significant change overtime, only a slight decrease at time t_1 in all species of local structures. This is surprising because from the confocal images of gel creaming in Fig.6.3, the gel structure evolves over time, especially for the first 3 time frames. The steady populations of local structures over time might indicate that under gravity, gel particles move up cooperatively and at similar speed. Although they all shift upwards, local structures are maintained the same. This shows indeed gel is only creaming, without other non-affine movements.

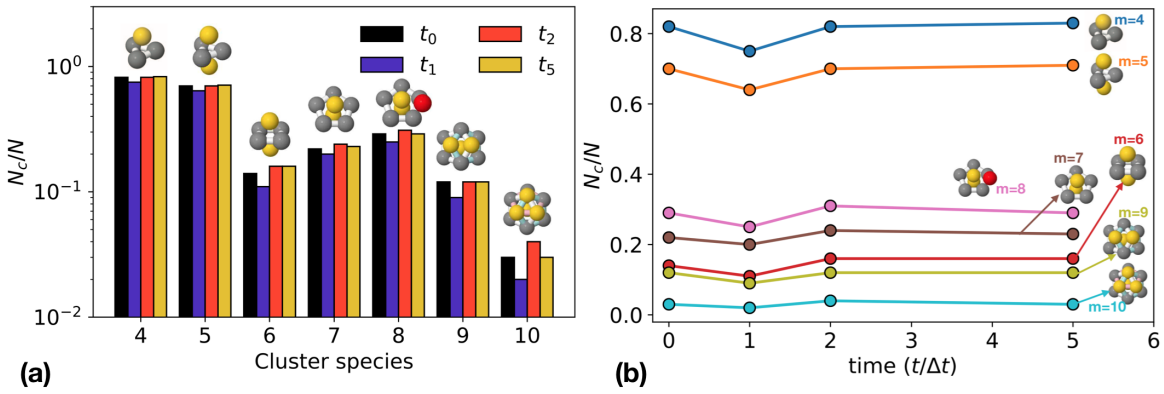

Fig. 6.8 (a) Bar plot of TCC populations against cluster species (with number of particles $m = 4$ to 10) at different time frames during gel creaming. (b) The same data are plotted as a function of time, to visualise the change of cluster populations over time, at time t_0,t_1,t_2, and t_5.

6.3.2 Contact forces and stress fields

Based on coordinates and sizes of interparticle contacts in confocal images, we calculate contact forces and stress fields for each time frame of the gel which is settling under gravity. The method of calculating contact forces is described in section 5.3.3.

Distributions of contact forces

The distributions of scaled contact forces over time are plotted in Fig. 6.9. The value of forces f is the number of pixels of tracked contact area, all plots are scaled with the average value of forces $\langle f \rangle$. In Fig. 6.9(a), the distributions for all time frames have plateaux at $f/\langle f \rangle = 1$ to 2, then decay at large forces, with a maximum range of about 5 times of the average force $\langle f \rangle$. From t_0 to t_1, the decay becomes faster; after t_1 the force distribution starts to decay more slowly again. This slower decay results in an increase of the range of force magnitude and also a wider plateau at small forces.

As discussed in section 5.3.3, the simulation study performed by O'Hern *et al*[4] showed that the emergency of a peak or plateau in the probability distribution of contact forces indicates a yield stress is developed in the system. We find plateaux for all distributions of gels with various polymer concentrations (described in section 5.3.3), this is plausible for gels which are viscoelastic materials. This also agrees with early times in Fig. 6.9(a), however the plateau starts to disappearing at later times. The flattening of distributions can also be proved by the fittings of all distributions. We fit each curve with a Gaussian distribution using the format of equation 5.2, fitted curves for each time frame is shown in Fig. 6.9(b) - (e). The fitting parameters are listed in Table. 6.1. We can see the parameter σ is small at t_0 and t_1, and increases to larger values at later times. This increase of variances of force

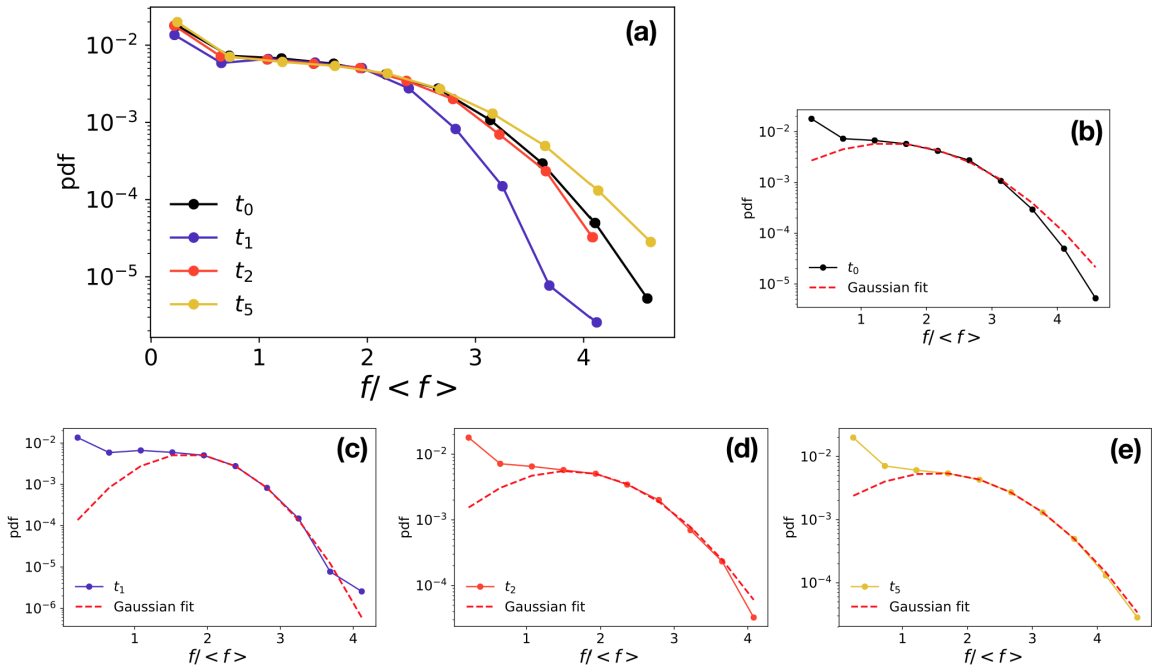

Fig. 6.9 Contact force distributions scaled with the average contact force $\langle f \rangle$ over all time series (a). Force distributions and Gaussian fittings for time frame (b) t_0, (c) t_1, (d) t_2, and (e) t_5.

distributions shows slower decays and less pronounced plateaux are emerging over the period of gel creaming.

Table 6.1 Gaussian fitting parameters for distributions of contact forces

	A	μ	σ
t_0	0.005	1.422	0.742
t_1	0.005	1.732	0.558
t_2	0.006	1.558	0.838
t_5	0.005	1.504	0.975

We can then infer that the disappearing of the plateau indicates that the external stress is already larger than the yield stress and the system is losing solidity or elasticity. At time t_5, after creaming to the top of the sample cell, the gel becomes more liquid-like, this agrees well with the drop of the first peak in $g(r)s$. At time t_1, the force distribution decays fastest, while the other three time frames decay with more similar rates, with the final time frame t_5 being the slowest.

The outlier time t_1 has a relatively low first peak of $g(r)$, this implies the effective stickiness in this time frame is less compared with other time frames. At the same volume fraction, less sticky spheres result in fewer neighbours and therefore fewer TCC structures. This is more clear in the Fig. 6.8(a) that populations of all TCC structures at time t_1 are

lower than others. Since these clusters are locally rigid structures, they are potential force carriers. The reduction in local structure populations results in fewer load bearing particles and possibly much fewer particles carrying large forces, and this would possibly be the reason for a fast and Gaussian force decay.

Distributions of local pressures

The local pressure P_{loc} distributions of the four time series are presented in Fig. 6.10. All distributions have a smooth peak at small values of stresses, and then decay exponentially. The decay becomes faster as the waiting time increases as we can see from curves of t_0, t_2 and t_5, while t_1 is the outlier which decays the slowest. For all of the curves, the high probability at very low values is absent which is distinctive to the peak in the distribution of contact forces.

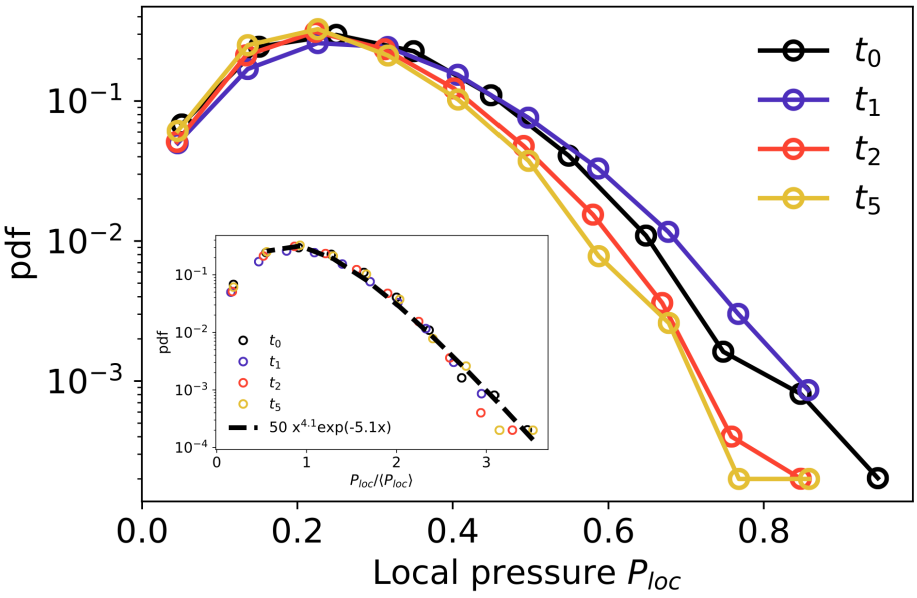

Fig. 6.10 Local pressure P_{loc} distributions of the gel over the period of creaming, for 4 time frames t_0, t_1, t_2, and t_5. Inset is the local pressure P_{loc} distribution scaled with the average local pressure $\langle P_{loc}\rangle$for each time frame.

The inset figure in Fig. 6.10 plots the distribution of scaled local pressure P_{loc} with its average value $\langle P_{loc}\rangle$, so that the scaled distributions peak at $P_{loc}/\langle P_{loc}\rangle = 1$. The scaled distributions collapse to a single curve, except for a subtle difference at the tail. The largest pressure in a particle is 3 times higher than the average pressure $\langle P_{loc}\rangle$. We fit the scaled distributions with an exponential format $pdf = Ax^n exp[-(n+1)x/\langle x\rangle]$. The fitting result is presented in the inset figure, with fitting parameters $A = 50$ and $n = 4.1$.

Force chains

From the stress tensor $\sigma_{ij} = \frac{1}{V}\sum_{c=1}^{N^c} \boldsymbol{f}_i^c \boldsymbol{r}_j^c$ of each particle we obtain the minor principal stress which is the most compressive stress of a particle. Based on these stresses we detect force chains in each time frame and plot distributions of length of force chains in Fig. 6.11. The distributions all follow exponential decays, the largest chain in each time frame comprises 13, 18 16 and 19 particles. The number of particles tracked in each time frame is 4937, 4736, 5000 and 5009, and the number of particles forming force chains is 1645, 1425, 1777 and 1878. We find that the fractions of particles that participate in force transmissions are 0.34, 0.30, 0.36, 0.37.

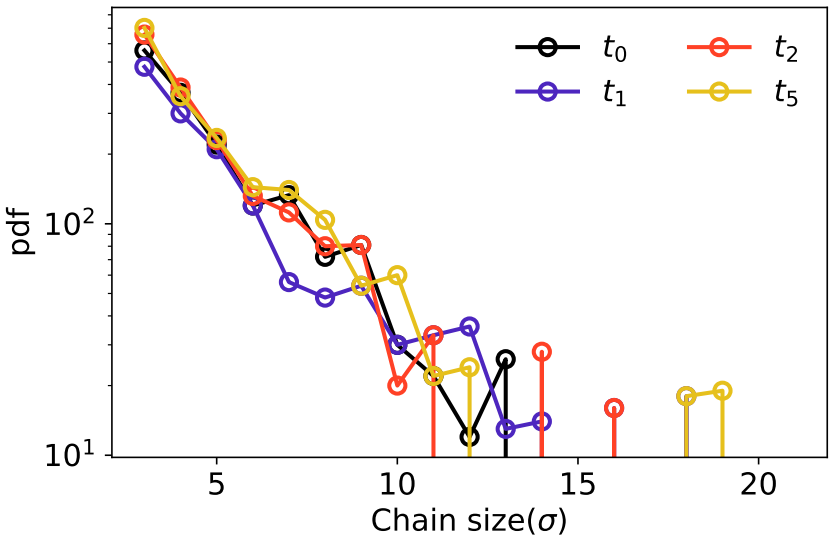

Fig. 6.11 Length of force chain distributions of the gel over the period of creaming, for 4 time frames t_0, t_1, t_2, and t_5. The length is characterised by counting the number of particles that make up the force chain.

We can notice that at time t_1, the percentage of particles participating in force chains is the lowest, however we can still find long force chain in this time frame with 18 particles. For other time frames, as we wait longer for the gel sample, there is an increasing of fraction of particles forming force chains, and the final time frame t_5 has the longest force chain. We think the longer force chain and higher fraction of particles forming force chains at t_5 is due to the increase of local packing fraction. A configuration with higher volume fraction and more neighbours would provide more chances for a compressive stress to be transmitted to the next particle, since the direction of compressive stress and the position vector between two contacting particles should be collinear to some degree. Although the final time frame has the longest force chain, we are unsure the magnitude of stresses transmitted through

the force chain. It would be interesting to examine the correlations between the size and magnitude of force chains.

6.3.3 Correlations of structures with contact forces

In order to investigate if local structures are affecting contact forces and stresses in the gel, force and local pressure distributions are plotted for each type of cluster, and we also compare the change of TCC cluster population for particles whether forming force chains or not.

TCC and stresses

In order to investigate the correlations between local structures and local pressures of particles, we plot the local pressure distributions for particles that participate in different TCC clusters for all time frames, as presented in Fig. 6.12. This figure shows that the distribution shapes for clusters with number of particles $m = 4$ to 9 are similar to the shape of the overall local pressure distribution.

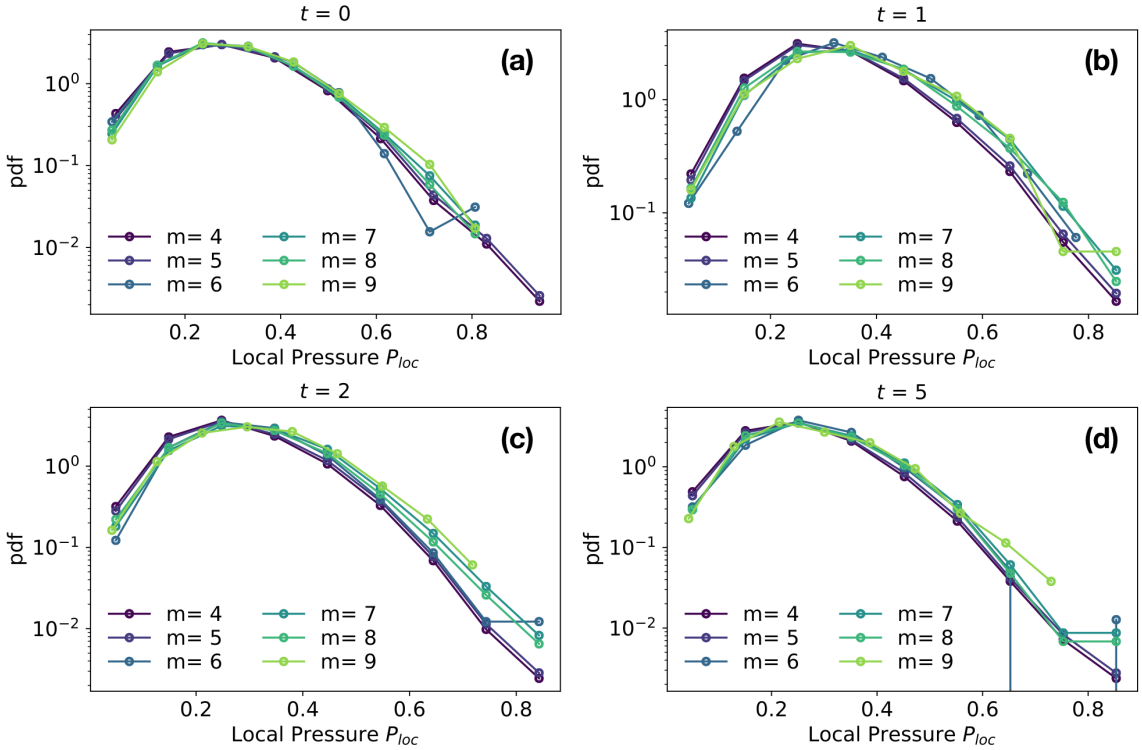

Fig. 6.12 Local pressure P_{loc} distributions of particles that form different TCC clusters with number of particles $m = 4$ to 9. The coupled distributions are plotted for 4 time frames (a) t_0, (b) t_1, (c) t_2, and (d) t_5.

There is no difference between different cluster species for the local pressure distributions at time t_0 and t_5, as can be seen from Fig. 6.12 (a) and (d). By comparison, at time t_1 and t_2, the pressure distribution decays faster in particles forming small clusters than those forming large clusters. The slower decay of large clusters implies that there is a higher percentage of particles bearing large stress (a higher probability at the tail), whereas it is difficult to find particles forming small clusters that are under large stresses.

From Fig. 6.12 we find that at time t_1 and t_2, particles in large local structures are more likely to carry large stresses, however we find there is no difference of pressure distributions for different clusters in time t_0 and t_5. At timet_0 and t_5, the gel sample is close to either side of the wall of sample cell, whereas at time t_1 and t_2 the main background is liquid solvent. This is an obvious distinction between these two different scenarios in pressure distribution, however we are not sure if the wall is making the difference.

We also plot the evolution of pressure distributions during creaming for particles that form different TCC clusters, as shown in Fig. 6.13. This figure can be considered as a decomposition of Fig. 6.10 to the local pressure distribution of each local structure with number of particles $m = 4$ to 9. Comparing these two figures, we find they have very similar shapes and trends. With time t_1 being the outlier, while the other distributions decay faster as the waiting time increases.

TCC in force chains

We further explore the role of local structures in the formation of force chains. The bar plot (Fig. 6.14 (a)) shows populations of different TCC clusters, with number of particles $m = 4$ to 9, of all particles in the gel sample, N_C^{all}/N^{all}, and only particles forming force chains (bars with hatch markers) N_C^{Chain}/N^{Chain} at time t_0. The results are similar for other time frames. We find increases of populations for all types of clusters, which means there is a higher percentage of TCC populations in particles that are forming force chains. This demonstrates that the TCC local structures are indeed bearing more stresses and responsible for stress transmissions in the system.

We also quantify the increase of populations by plotting the ratio R_{Chain} in Fig. 6.14 (b). This quantity measures the degree of population growth and is calculated as $\frac{N_C^{Chain}/N^{Chain}}{N_C/N^{all}}$. From the figure we can see the trend of an increase of R_{Chain} with growing cluster sizes. There is a more evident increase in populations of large clusters. In order to form force chains, particles need to carry large enough stress and also there are a good selection of neighbours that any of them is aligning with the stress vector. Large TCC clusters are locally rigid and intrinsically assumed to bear stresses, also constructed with a relatively large number of

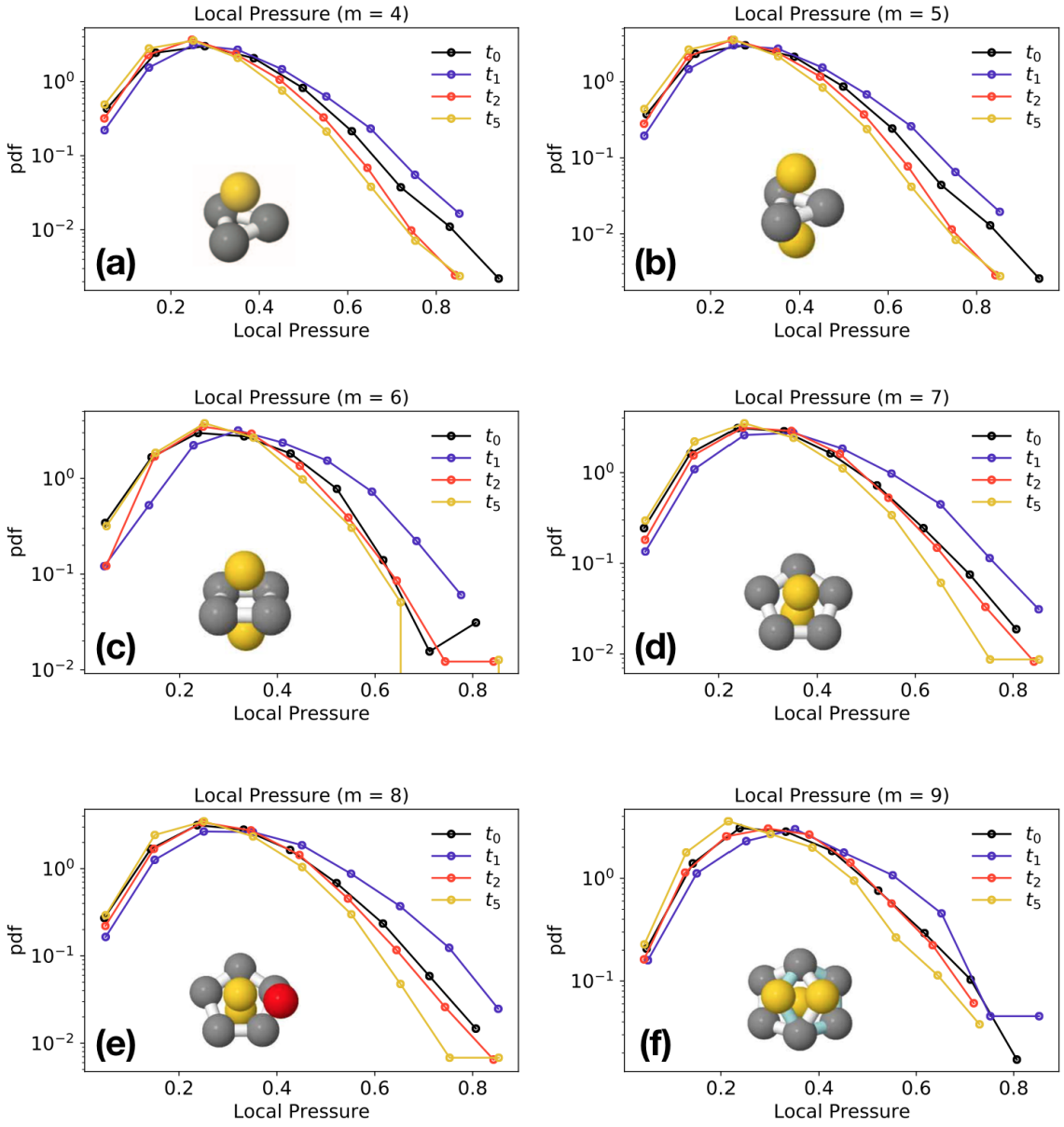

Fig. 6.13 Time evolutions of local pressure P_{loc} distributions of particles that form TCC clusters with number of particles (a) $m = 4$, (b) $m = 5$, (c) $m = 6$, (d) $m = 7$, (e) $m = 8$, and (f) $m = 9$.

particles, *e.g* $m = 8$, 9, and 10, there are more neighbours and higher chances for the central reference particles to transmit the stress to the next neighbour, *i.e.* forming part of a force chain.

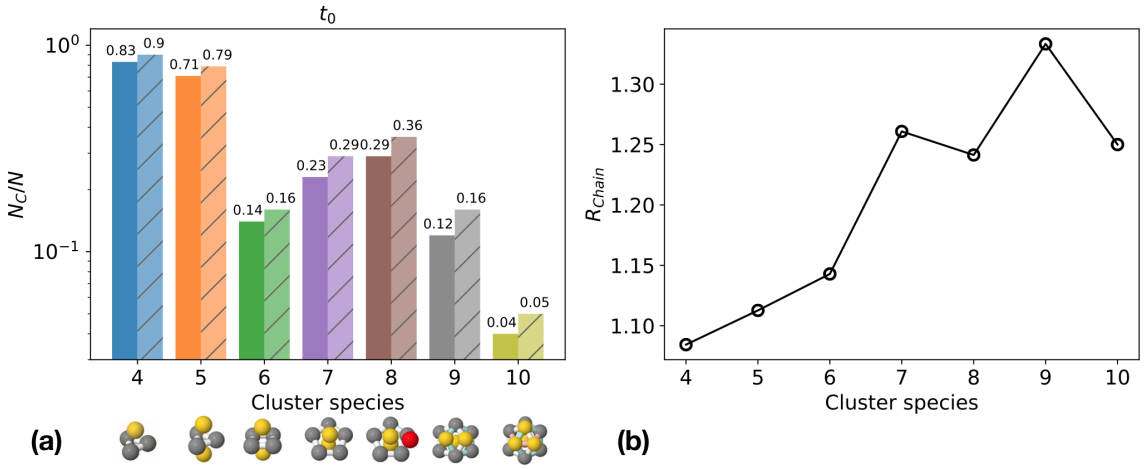

Fig. 6.14 Comparison of TCC cluster populations in all gel particles and only particles forming force chains. (a) Bar plot of populations of TCC clusters with particles participating force chains or not. Bars with hatched markers are particles forming force chains. (b) Plot of R_{Chain} against different species of local structures with number of particles $m = 4$ to 9.

6.4 Summary

A colloid-polymer mixture with colloid volume fraction $\phi_c = 0.23$, is quenched below the effective temperature for gelation, and it creams to the top of the sample cell within our observation time window, due to the density mismatch between PDMS oil droplets and aqueous phases. We selected four time frames which represent different stages in z direction during the gel creaming process. It creams to the topof the sample cell in about 320 τ_B. We characterised the process using confocal microscopy, by tracking particle and contact positions, we are able to resolve structural changes and contact force distributions during gel settling. Surprisingly, although the gel travels all the way crossing the sample height to the top, there is no significant change of either structures and force distributions.

A subtle increase is found in the peak in the distribution number of neighbours $P(N)$, this might be due to the increase of local particle volume fraction when the gel only occupies the top part of the sample cell. However, the other structural properties like pair correlation function $g(r)$, number of contacts Z, and topological cluster classification (TCC) local structures remain almost identical for all time frames. The consistent gel structures confirm the settling behaviour we observed is more likely to be a creeping sedimentation rather than gel collapse.

The distributions of contact forces are fitted with Gaussian distributions, while the distribution of local pressure decays exponentially. Except for the outlier of time frame t_1, the distributions of contact forces broaden as gel creams further, the peak also becomes less

pronounced. In the simulation study of supercooled Lennard-Jones liquids by O'Hern *et al*[4], they show that the emergence of the peak in the contact force distribution indicates the development of solidity and a yield stress in the system. It is conveniently to infer that the disappearing in turn indicates the loss of solidity and the system returns to liquid-like, and this is similar to what we find at the end of gel creaming. It would be interesting to check the force distribution at even longer time frame, when the gel structure completely disappeared, becomes a dense colloidal liquid.

The length of the longest force chains and the fraction of particles participating in force chains also increase with time. The longest force chain increases from 13 to 19 particle diameters. and he fraction of particles participating in force chains rises from 0.34 to 0.37. Force chains are not percolated for all time frames. Non-percolated force chains might be accounted for the gel being not mechanically stable and creaming under gravity.

Similar to the finding in previous chapter, particles that participate in force chains have higher percentage forming local structures. This means local structures do play a role in assembling into force chains, and particles forming local structures carry more stresses than those free particles.

The subtle changes in force and stress arrangements are closely related to the consistent gel structures during settling. The experiment can be improved by increasing the size of sample cell, so that a minimum sample height is satisfied for gels to collapse. During collapse, gel structure will change markedly and thus provides the opportunity for diverse scenarios of force distributions and transmissions. After the delay time, collapse happens rapidly, thus a shorter time interval for 3D confocal stack images is required in order to be able to capture all structural and microscopic force changes during the rapid collapse. Smaller particles or solvent with better density matching property will reduce the creaming rate, thus are useful for studying gel collapse.

Another interesting piece of work can be done is to shear colloidal gels. The application of an external shear force is anisotropic which is intrinsically different from gravity. The magnitude and frequency are easily adjusted by controlling shear cells. Investigating the response of colloidal gels to external shear forces with regard to structures and microscopic contact forces is intriguing and fundamental to explore mechanical properties of gels.

Chapter 7

Contact Forces in Dense Colloidal Emulsions

7.1 Introduction

As the material falls out of equilibrium, when its structural relaxation time τ_α exceeds the observation time, it becomes dynamically trapped and forms a glass. There are several competing theories of glassy behaviour. The predictions of one such theory, the random first-order transition (RFOT) scenario[161], are illustrated in Fig. 7.1. For high volume fractions, $\phi > \phi_g$, the system supports multiple amorphous solid states, so that ϕ_g corresponds to a glass transition. In the state close to ϕ_g, colloidal particles are not in contact with each other, and thermal fluctuations mean that they are in constant motion. However, on further compression, the particles come into contact and the system becomes jammed. If the energy scale ε associated with contact forces exceeds k_BT, thermal forces are no longer strong enough break the contacts, and particle motion becomes almost completely arrested - the system approaches the athermal (granular) limit ($k_BT/\varepsilon \to 0$).

A recent study carried out by Dinkgreve *et al*[162] has found strikingly similar non-Newtonian flow behaviour of athermal jamming and thermal glass suspensions. They demonstrated that the yield-stress flow curves of thermal and athermal systems can be scaled onto one universal curve, using the Laplace pressure as stress scale for athermal systems and the osmotic pressure for the thermal systems. The same power-law exponents were found for the glass and jamming effects. When below the jamming volume fraction at $\phi < \phi_J$, they do not find a new Newtonian regime of diverging viscosity at high shear rates which should develop if the jamming and glass transitions are sufficiently separated[163].

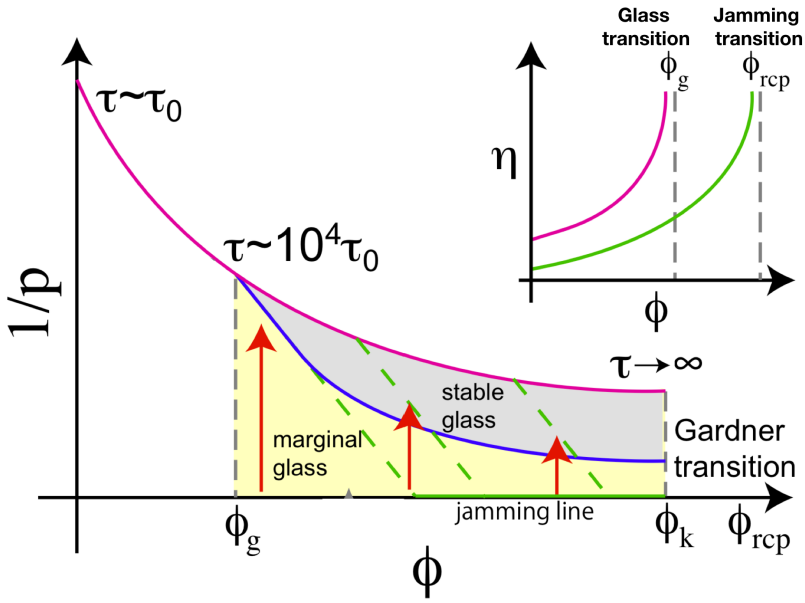

Fig. 7.1 Hard spheres at high density. Inverse pressure $1/p$ is plotted against volume fraction ϕ. The gray and yellow regions indicate the regime where the (meta)basin structure is present, either as a simple stable glass or as a marginal fractal glass with a fractal free energy landscape. The left-most boundary of the glass region is the threshold line (dark blue). The "J-line" of jammed packings is found along pressure $p = \infty$, which always falls within the marginal phase (green line). An adiabatically slow compression from the stable glass should leave the equilibrium liquid line and eventually reach the J-line, while remaining within the white region. As indicated by the green dashed lines $\phi_g \approx 0.59$ is the glass transition where the system falls out of equilibrium on the experimental timescale. $\phi_k < \phi_{rcp}$ is the Kauzmann transition where a transition to an "ideal glass" (whose structural relaxation time would diverge) may occur. At this point the system would occupy a sub-extensive number of states. It is thought to be less than that of random close packing (RCP)[7].

The glass-to-jamming crossover is still under research and not unified. The RFOT theory predicts that the thermal glass state and the athermal jammed one are separated by a transition, this was first proposed by Gardner in the context of spin glasses[164], ss shown in Fig. 7.1. The energy landscape of the liquid phase is a single smooth basin, due to the unbroken replica symmetry of an ergodic phase, as shown in Fig. 7.2 (a). In the stable glass phase, this replica symmetry is broken and the landscape becomes many smooth basins which are separated by free energy barriers inhibiting one glass passing to another, as shown in Fig. 7.2 (b). However, within each individual basin, there is till replica symmetry. In the marginal Gardner glass phase, the replica symmetry is infinitely broken so that each basin splits into an hierarchical arrangement of marginally stable sub-basins[7, 165].

This transition is accompanied by a rich set of phenomena, including the breakdown of linear elastic response to mechanical load. In experiments, this should be signalled by strong sample-to-sample fluctuations of the (macroscopic) stress and strain, related to avalanches or

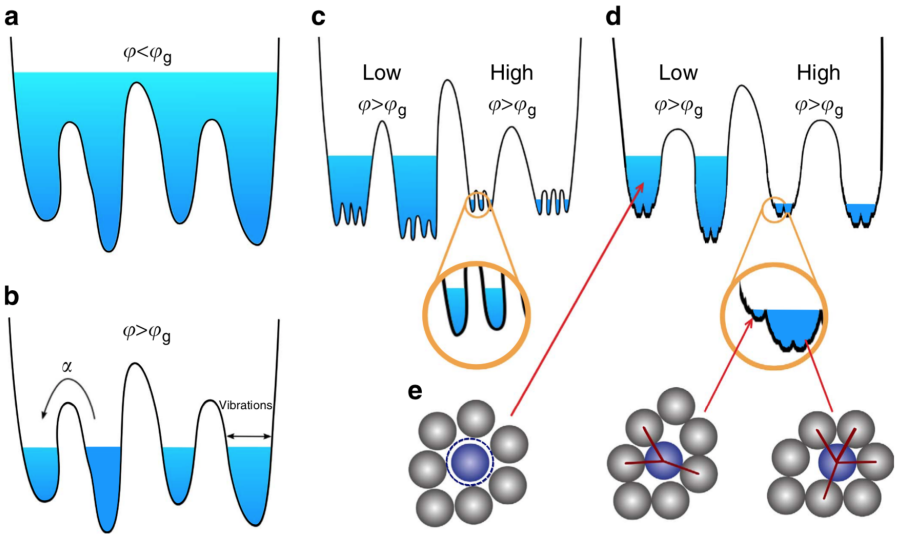

Fig. 7.2 Schematic illustrations of free energy landscpe of (a) the liquid state at volume fraction $\phi < \phi_g$. At $\phi > \phi_g$ basins in the energy landscape (b) divide fractally into sub-bains (c) and sub-sub-basins (d) representing marginally mechanically stable states close to a jamming transition. The very bottom of each of these sub-basins correponds to a given realisation of the force network (red lines), but the identification of the force contacts remains undetermined before the fractal regime is reached (dashed line)[7].

correlated plastic events, and contrary to the familiar situation of a deterministic constitutive relationship. Some familiar phenomena appear in computer simulations of quasistatic shear[166], and in granular systems[167], but it is not known whether these predictions are valid for thermal systems with dimension $d = 3$.

The identification of the force-bearing neighbours at jamming is a unique characterisation of the state, the emergence of force-bearing neighbours highly depends on the landscape structure, as indicated in Fig. 7.2 (e). In the scenario of simple basins, force-bearing neighbours at jamming should be completely determined instantly on moving from the equilibrium liquid; in the sub-basin scenario, that determination should only occur once the system is sufficiently deep in the glass so that transitions between sub-basins are fully suppressed; in the fractal basins, on the contrary, the contacts are determined gradually as approaching jamming[7].

At intermediate pressure, between the Gardner transition and jamming, force chains within the system are quasi-permanent, which are unable to relax. Between the Gardner transition and the glass transition, the system has higher thermal energy that force chains dissipate[7]. So far this has only been discovered in numerical simulations, there is no experimental identification of force-bearing neighbours and force chains in glassy materials. Our emulsion system acts as an excellent experimental model system for this purpose. First

of all emulsions are slightly deformable, so that we can reach high volume fractions beyond the jamming point which is around the random close packing (RCP) of 0.64. This would be difficult to be achieved in other colloidal particle systems such as PMMA or silica particles. Secondly the ability of visualising interparticle contacts in our emulsion systems enable us to determine force-bearing neighbours and force chains in colloidal glasses, and this was previously inaccessible to thermal systems.

7.2 Experimental methods

Emulsion droplets used in this chapter are prepared using the chemical synthesis method described in section 2.1, which is the same as chapter 5 and chapter 6. The prehydrolysing time of DMDES is 15 hours and the growth time is 96 hours after mixing prehydrolysed DMDES, deionised water and ammonium hydroxide. This yields droplets with mean diameter of 3.1μm, measured from confocal images. This method can produce droplets with polydispersity less than 8%, by fractionating the dilute emulsions a few times (normally three times) after dialysis. However since we aim to prepare colloidal glasses, we do need some polydispersity in the system. We thus only fractionate the dialysed emulsions once to remove residual oil at the top surface of the emulsion, there are still a few large droplets remained in the final emulsion.

The volume fraction of emulsions after dialysis is approximately 1%. The emulsion is left under gravity to cream and concentrate due to the density mismatch between PDMS and water. After about a week, the bottom of the emulsion becomes transparent, only a thin layer of creamed droplets is on the top of the emulsion. The creamed droplets are transferred from the 250 mL glass bottle to an eppendorf, Nile Red dye is added for fluorescent labelling. Glycerol is added drop by drop to index match the droplets, until the emulsion becomes transparent with a pink colour. The concentrated and index matched emulsion has 2 mM SDBS surfactant for droplet stabilisation and 10 mM potassium chloride to screen charges on droplets surfaces.

When the emulsion does not cream further under gravity, we imaged the creamed part under confocal microscopy, and found the volume fraction of the concentrated part is less than 0.55 which is far from the generally accepted value for random close packing (0.64). To further increase the volume fraction and be able to prepare colloidal glasses, external stresses were applied to the emulsion by centrifuging it at various speeds. Three dense emulsion samples are presented in this chapter, one sample is subjected only to gravity, the other two are centrifuged for 30 min at speed of 1000 rpm and 2000 rpm respectively.

After centrifugation, the top dense part of emulsion is taken out from the eppendorf using a spatula. The dense emulsion is placed in a 25 μL gene frame and sealed with a glass cover slip. The sample is then observed under confocal microscope within 5 min after the centrifugation, the characterisation setup is the same as described in section 5.2.2. Each 3D stack has dimension of 512 $\times$ 512 $\times$ 512 pixels, with pixel size of 150 nm so that the length in each dimension is 76.85μm. Confocal images of 2D *xy* slices of three dense samples are shown in Fig 7.3.

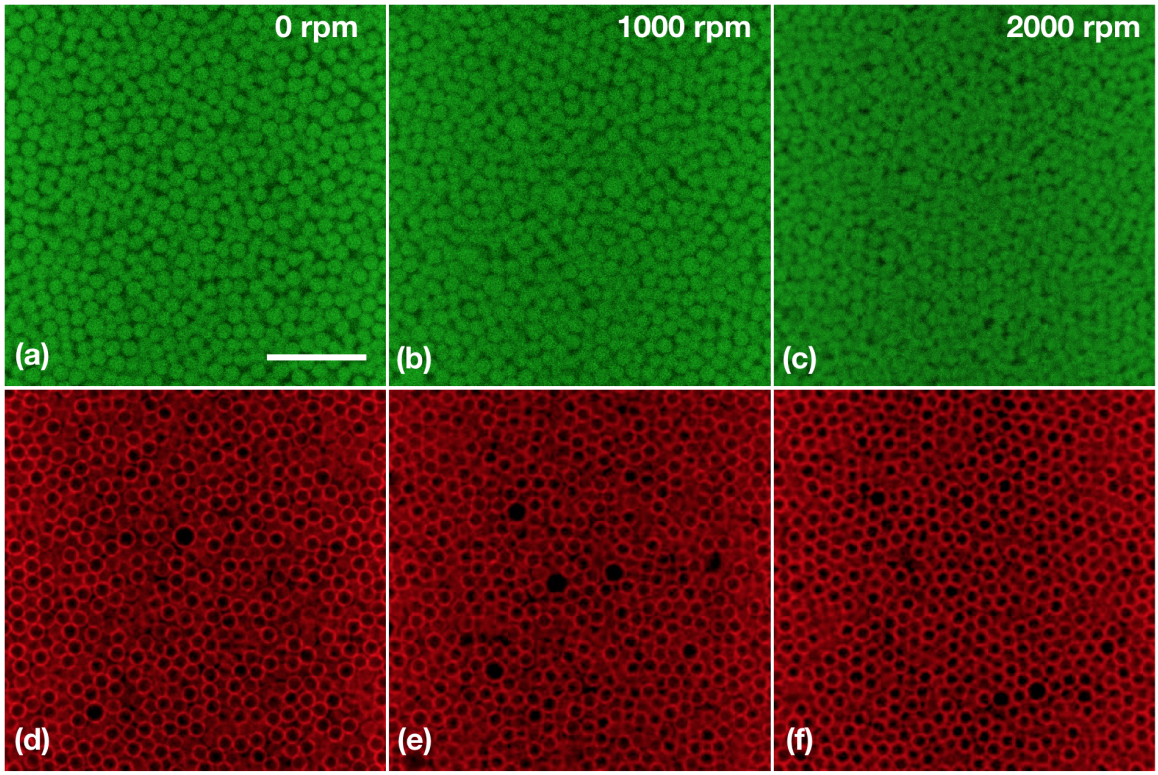

Fig. 7.3 Confocal images of three dense emulsions. (a-c) Confocal images with detection wavelengths of 520 nm - 575 nm, showing particles in dense emulsions under gravity, centrifugation of 1000 rpm and 2000 rpm respectively. (d-f) Confocal images with detection wavelengths of 585 nm - 640 nm showing interparticle contacts under certain external forces. Scale bar represents 20 μm.

7.3 Results and discussion

Similar to chapter 5 and chapter 6, we performed structural analysis and contact force measurements on these three dense emulsions.

7.3.1 Structural measurements

Using colloids tracking method, we find 14783, 14557 and 15996 particle coordinates in each sample. By removing particles at edges of image boxes, and considering new boxes with dimensions of $(x-\sigma)\times(y-\sigma)\times(z-\sigma)$, where σ is the mean particle diameter, we find the volume fraction of each sample is $\phi = 0.55$, 0.54 and 0.60. This is surprising because the emulsion that is centrifuged at speed of 1000 rpm for 30 min has a lower volume fraction than the emulsion which is only creamed under gravity. We would expect that a larger external force applies higher pressure to the system and therefore leads to higher volume fraction.

One possible explanation is that stresses induced when centrifuging at 1000 rpm is not significantly higher than the gravitational stress, the resulted volume fraction are comparable. During imaging under confocal microscope, emulsions keep creaming and have a density gradient along z direction. These two image stacks might be taken at different value of z axis, the sample only with the gravitational stress is possibly taken in a denser region. Otherwise it is possible that the timescale of 30 min is not long enough to generate a homogeneous dense emulsion in the eppendorf, there is also a gradient with the top being denser. However we might take the relatively lower part of the dense emulsion for imaging, which has volume fraction comparable to the creamed emulsion.

In the following context we will present results on the order of the value of volume fraction rather than the magnitude of external forces.

Pair correlation function

Using the positions of particle centres, we plot the pair correlation functions $g(r)s$ of three dense emulsions in Fig. 7.4. Due to high volume fractions, these three emulsions can be considered as supercooled liquids, especially the highest one with $\phi = 0.60$ is above the glass transition volume fraction $\phi_g = 0.58$, we would expect this emulsion is dynamically arrested and has properties similar to a colloidal glass.

Compared with $g(r)s$ of gels in chapter 5 and 6, the height of the first peak is less pronounced in dense emulsions, because no attractive potential is presented. There is also emergence of small peaks at distances of $r/\sigma = 3$ and 4, indicating longer correlations of particle positions in dense emulsions. The emulsion with highest volume fraction $\phi = 0.60$ has a more noticeable peak at $r/\sigma = 4$ than the other two emulsions. From the confocal images in Fig. 7.3 we can see some local ordering in small regions in emulsions, which means crystal is forming in these dense emulsions, however $g(r)s$ do not show any indication of crystallisation in the system.

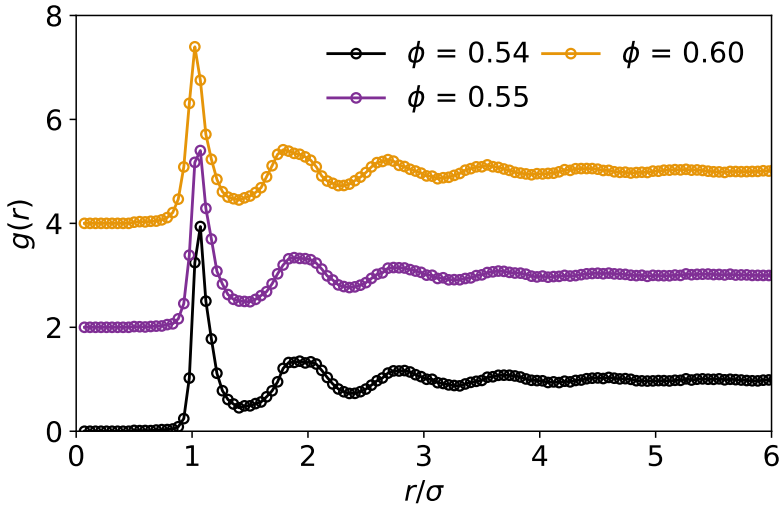

Fig. 7.4 Pair correlation functions $g(r)s$ of dense colloidal emulsions with volume fraction of ϕ = 0.54, 0.55 and 0.60.

Number of neighbours and contacts

Distributions of number of neighbours $P(N)$ and contacts $P(Z)$ in these dense emulsions are plotted in Fig. 7.5 and Fig. 7.6. Since two of the emulsions have very similar volume fraction, the distributions of these two samples are almost identical. Both have 11 nearest neighbour particles and 9 contacting particles as mean values. As the volume fraction ϕ increases to 0.60, the mean number of neighbours $\langle N \rangle$ rises to 12. The distributions of neighbours are strongly negatively skewed, with a long tail at small number of neighbours, and peak approximately at 12 for all samples. In the emulsion with the highest volume fraction, there are more particles that have neighbours more than the peak value, the distribution slightly shifts to the right so that the mean number also increases.

The average number of contacts $\langle Z \rangle$ of these three samples is the same and stays at 9, which is far above the minimal number of contacts for rigidity[4]. Considering that all volume fractions are below ϕ_g, particles should not be in contact for a long time because of the thermal motion. Both number of neighbours and contacts are higher than expected, this might due to the low accuracy of the estimation of volume fractions. The volume fraction cannot be directly calculated after centrifugation, because unlike rigid colloids such as silica particles, the volume fraction of emulsions can go beyond the volume fraction of RCP (0.64). Depending on the conditions of centrifugation, the volume fraction of emulsions varies. Hence we determine the sample volume fraction from the information of particle tracking. As described in section 2.5, the average diameter of droplets is estimated by comparing with the first peak of $g(r)$. By multiplying the volume of each particle with the number of particles

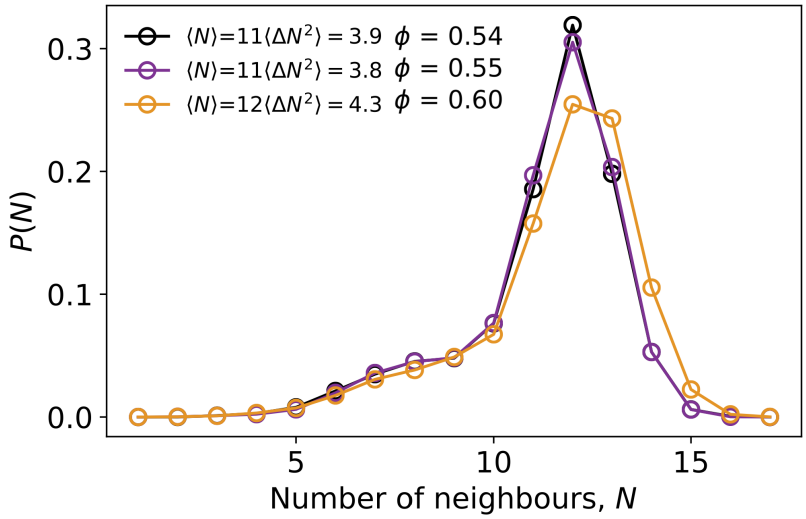

Fig. 7.5 Distributions of number of neighbours of dense emulsions with volume fraction $\phi = 0.54$ (black), 0.55 (purple) and 0.60 (yellow).

tracked, we can calculate the volume fraction. However, this method highly depends on the accuracy of particle tracking. Inevitably there is tracking error, particles that are not tracked will result in decrease of particle volume fraction. Therefore a more accurate approach of measuring the volume fraction of dense emulsions is desired to unveil the actual physical state of colloidal suspensions.

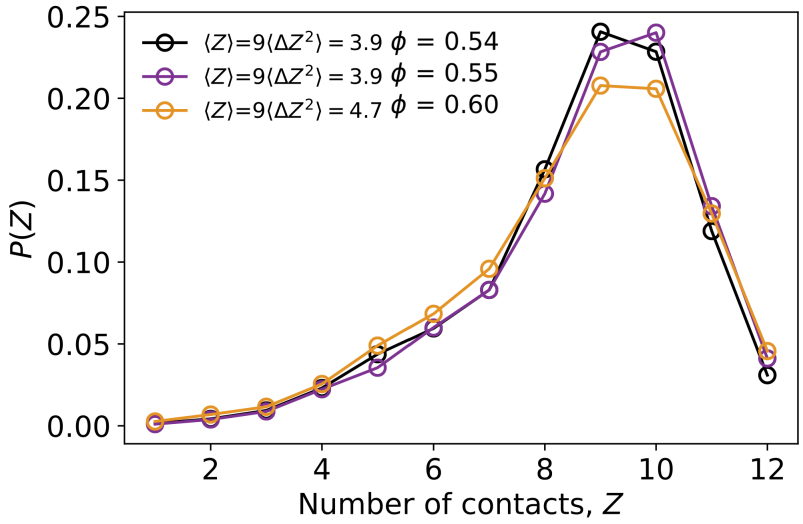

Fig. 7.6 Distributions of number of contacts of dense emulsions with volume fraction $\phi = 0.54$ (black), 0.55 (purple) and 0.60 (yellow).

Although the average contact number is the same, the distribution of the emulsion with the highest volume fraction shows lower probability around the peak value, and higher probability

at small values. As the volume fraction increases, the number of neighbours increases while the number of contacts remains the same or even slightly decreases. We are still unsure about why the number of contacts Z decreases with higher external centrifugational force and higher particle volume fraction.

Topological cluster classification

Since the pair correlation function $g(r)$ only shows the averaged bulk structural properties of these emulsions, the TCC analysis is performed to resolve local structures, the populations of clusters with different sizes are presented in Fig. 7.7. Compared with local structures in colloidal gels (5.10) which have particle volume fraction around 0.25, in dense emulsions we find larger clusters with number of particles $m > 10$. The populations of all types of clusters increase markedly, for instance there are more than 95% particles can form cluster of tetrahedra with $m = 5$, the population of cluster with number of particle $m = 9$ also rises from less than 15% to about 70%.

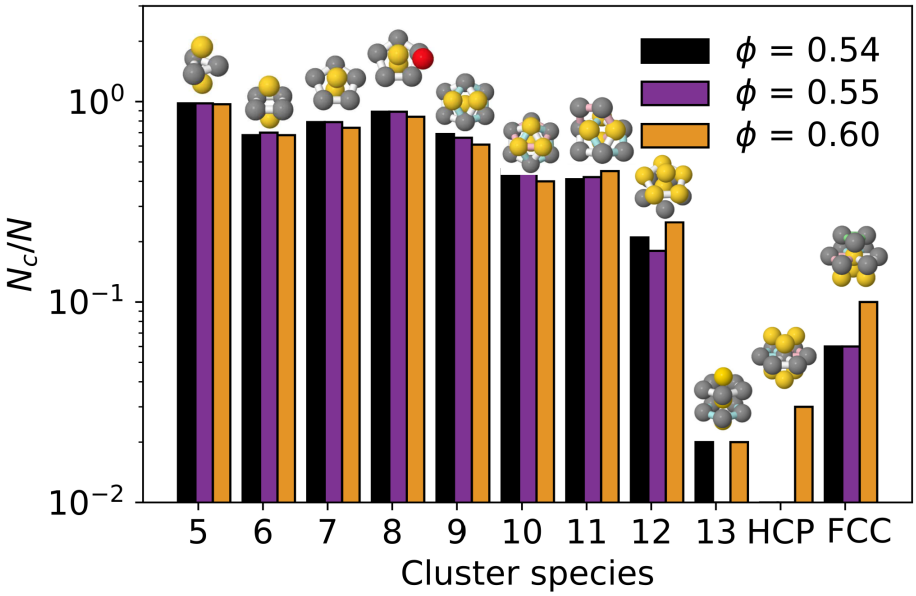

Fig. 7.7 (a) Populations of TCC local structures against cluster species (with number of particles m = 4 to 10) for dense emulsions with volume fractions of ϕ = 0.54, 0.55 and 0.60.

Within the three dense emulsions, there is no obvious difference between the two emulsions with lower volume fractions of ϕ = 0.54 and 0.55 in TCC populations. As for the densest emulsion with ϕ = 0.60, the populations of small and medium sized clusters with m = 5 - 10 decrease slightly, whereas populations of large clusters increase for $m > 10$. The crystalline cluster of hexagonal close-packed (HCP) is only presented in the emulsion with ϕ

= 0.60. Another crystalline structure face centred-cubic (FCC) is found in all three emulsions, but its population is highest in the densest emulsion.

The emergence of crystalline structures of HCP and FCC indicates all three emulsions are undergoing crystallisation. But the crystal populations are relatively low compared with other cluster populations, this means there are only small regions are forming crystals while the majority of the samples remain amorphous, as can be seen in the confocal images in Fig.7.3. Since the data presented in this chapter are characterised 5 min after preparation, emulsions are not equilibrated, we would expect crystal sizes will grow for longer waiting time. The emulsions starting to form crystals is attributed to the low polydispersity of droplets. The polydispersity of three samples are about 8%, which is at the limit for forming colloidal glasses . The emulsion is from the same batch of synthesis, the fact that the last sample has formed more crystals is possibly due to the centrifugation. After high speed of centrifugation, the emulsion with some polydispersity is fractionated. Depending on the positions of droplets in the eppendorf, centrifuged droplets have slightly different sizes but all with lower polydispersity.

7.3.2 Contact forces and stress fields

Based on coordinates and sizes of interparticle contacts in confocal images, we calculate contact forces and stress fields for each time frame of the gel which is settling under gravity.

Distributions of contact forces

Contact force distributions of three dense emulsions are shown in Fig. 7.8. The behaviour also shows some distinct features from the force distributions in colloidal gels. From Fig. 7.8 (a) we can see the distributions of emulsions with ϕ = 0.54 and 0.55 have similar shapes, they both have a smooth peak at the value $f/\langle f\rangle$ around 1.5. At large forces, the tail dose not decay to zero following a Gaussian distribution, it reaches a plateau or decays very slowly when forces are larger than $f/\langle f\rangle > 3.5$, this is different from that of colloidal gels. As for the emulsion with the highest volume fraction ϕ = 0.60, the peak almost disappears, the distribution looks like a straight line in the log plot, with a small bump at $f/\langle f\rangle$ around 1.5 and also a flat tail when $f/\langle f\rangle > 4.5$.

We still attempt to fit all curves with Gaussian distributions using the expression of equation 5.2, the fitting result for each curve is shown in Fig. 7.8 (b - d), and the fitting parameters are presented in the table in Fig. 7.8. We can see the fitting agrees well with each curve at range $0.5 < f/\langle f\rangle < 3.5$. The flat tail at large forces and very high probability at small forces cannot be described by a simply Gaussian distribution. The fitting parameters

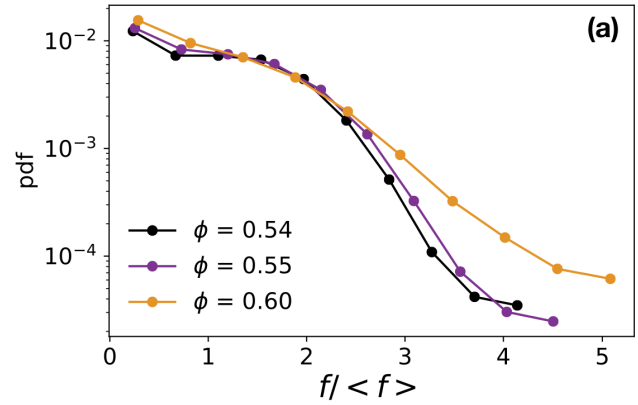

Fitting parameters

ϕ_c	A	μ	σ
0.54	0.007	1.234	0.710
0.55	0.008	1.746	0.781
0.60	0.010	0.313	1.204

Fig. 7.8 (a) Contact force distributions scaled with the average contact force $\langle f \rangle$ in dense emulsions. Force distributions and gaussian fittings for volume fraction ϕ of (b) 0.54, (c) 0.55 and (d) 0.60.

are similar for the two samples with close values of volume fractions, whereas the standard deviation σ of the densest emulsion is significantly higher than the other two, also the mean value μ is much lower. Both features imply the characteristic Gaussian peak is disappearing as the particle volume fraction increases, and the distribution is more close to a exponential decay.

As we mentioned in chapter 5, an exponential distribution of contact forces is an important feature in jammed matter[76, 4]. The densest emulsion has volume fraction $\phi = 0.60$ which is close to the random close packing value of 0.64. We argue that it is because the dense sample is close to jamming that the force distribution shows features similar to exponential distribution. As the supercooled liquid is quenched to lower higher ϕ, it becomes more dynamically arrested, although there are small regions of crystals, with the majority of the sample still being amorphous (glassy) or even close to jammed state, we observe a transition of contact force distributions from Gaussian-like to exponential-like.

Distributions of local pressures

The transition from a Gaussian-like to a slower exponential decay as particle volume fraction increases is more evident in the distributions of local pressures, as shown in Fig. 7.9. The

distribution is also scaled with the average pressure $\langle P_{loc} \rangle$ in each sample. The scaled distributions all peaked at the average local pressure at $P_{loc}/\langle P_{loc} \rangle = 1$.

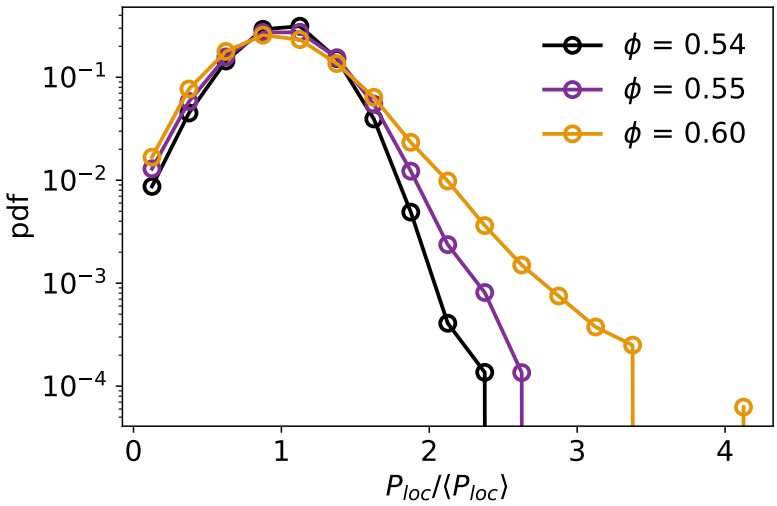

Fig. 7.9 Local pressure P_{loc} distributions dense emulsions with volume fraction $\phi = 0.54$, 0.55 and 0.60.

Local pressures in the emulsion with $\phi = 0.54$ decay as a Gaussian distribution, the largest local pressure is about 2.4 times of the average local pressure $\langle P_{loc} \rangle$. As the volume fraction increases to $\phi = 0.55$, local pressures decay slower, and end at the maximum value of $P_{loc}/\langle P_{loc} \rangle \approx 2.6$. The emulsion with the highest volume fraction follows an exponential decay, and has the largest range of local pressures across the sample. The maximum local pressure is 4 times higher than the average local pressure $\langle P_{loc} \rangle$.

Force chains

The distributions of the size of force chains are shown in Fig. 7.10. Force chains in these three dense emulsions become much longer than those found in colloidal gels. Some force chains span over more than 300 particle diameters whereas force chains in gels are less than 30 particles. The dramatic increase of force chain size is mainly attributed to the increase of number of neighbours and contacts. From the definition of force chains, the most compressive stress of two contacting particles must be collinear to some extent, having one more contacting particle will increase the chance of finding a particle that is collinear with the reference particle.

The percentage of particles participating in force chains for three emulsions is 86%, 89% and 85% respectively. Compared with the low participating ratios in gels, there is a significant increase of number of particles forming force chains. Since there is higher attraction strength

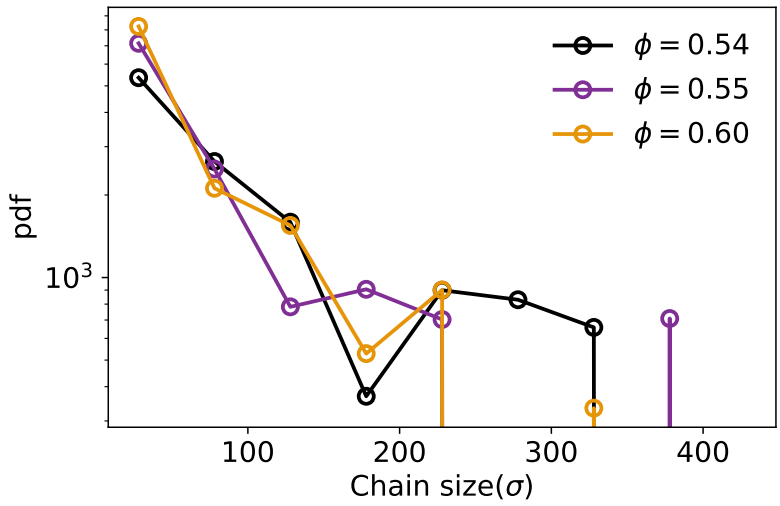

Fig. 7.10 Force chain size distributions of dense emulsions with volume fraction $\phi = 0.54$, 0.55 and 0.60. The threshold angle for determining the collinearity of force chains is 45°, which is the same as the one used in colloidal gels.

in gels while the dense emulsions are purely hard sphere repulsions, therefore the increase of the percentage that particle forming force chains is strongly attributed to the increase of particle volume fraction. Among these dense emulsions, the sample with $\phi = 0.55$ has the largest number of neighbours and number of contacts. Higher numbers of neighbours and contacts result in the increase of size of force chains and the percentages of particles forming force chains.

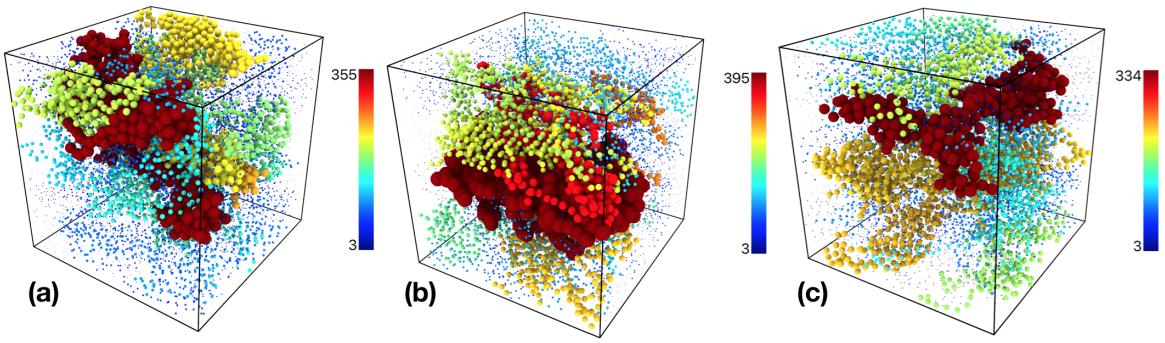

Fig. 7.11 Rendering of force chains in dense emulsions with volume fraction ϕ of (a) 0.54, (b) 0.55 and (c) 0.60. Color indicates the size of force chains, particles in red are in relatively long force chains. The radius of particles are also adjusted to better visualise the spatial distributions of force chains, particles in large chains are shown with bigger radii.

From the spatial distributions of force chains in Fig. 7.11, we can see these force chains are not percolated although their sizes grow markedly compared with those of gels. The

longest force chains which are marked in dark red, in emulsions with volume fraction ϕ = 0.54 and 0.55, stretch over a long distance only in one direction, whereas the long force chain in the emulsion with the highest volume fraction expands both in x and y directions. Non-percolated force chains imply the system which is a mixture of glass and small regions of crystal, is not jammed and mechanically stable, an infinitesimal stress applied can deform the system.

7.3.3 Correlations of structures with contact forces

TCC and stresses

In order to investigate the role of local structures in determining stress distributions in dense emulsions, we plot the stress distributions of particles that are forming various species of TCC clusters in Fig. 7.12. Only two volume fractions are shown because the distributions of the sample with volume fraction ϕ = 0.54 and 0.55 are very similar. The shapes of the scaled local pressure distributions are different for emulsions with different volume fractions, the range of the distribution is wider when the volume fraction is higher, as we already observed in Fig. 7.9. In both plots in Fig. 7.12, as the size of TCC cluster increases, the range of the distribution becomes narrower, therefore the tail at large pressures of the overall distribution is dominant by small clusters. Notably in Fig. 7.12 (a), the distribution becomes more Gaussian-like as the size of cluster increases. This is more clearly observed in Fig. 7.13 which shows the comparison of local pressure distributions of different volume fractions for each type of cluster.

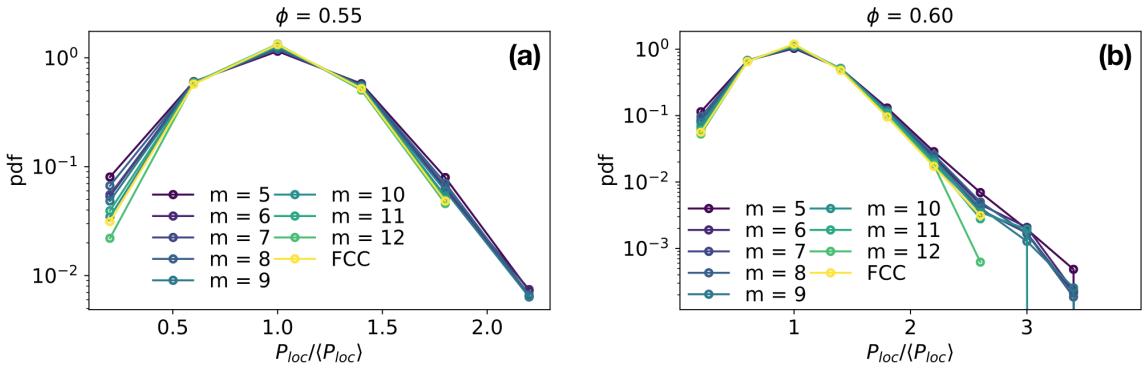

Fig. 7.12 Local pressure P_{loc} distributions of particles that form different TCC clusters with number of particles m = 6 to 12 and FCC cluster in emulsion with volume fraction ϕ of (a) 0.55 and (b) 0.60.

The distributions of particles forming $m = 13$ cluster and HCP are not presented in Fig. 7.13, because these clusters are absent in some of the samples with low volume fraction. From Fig. 7.13 we can see the shape of distributions of small clusters are very similar to

that of the bulk samples, as the size of cluster increases, the range of distribution becomes narrower as the size of cluster increases, decays faster and becomes more Gaussian-like. The similar behaviours of small clusters and the overall property are attributed to the high population of small clusters which is more than 80% for $m < 10$.

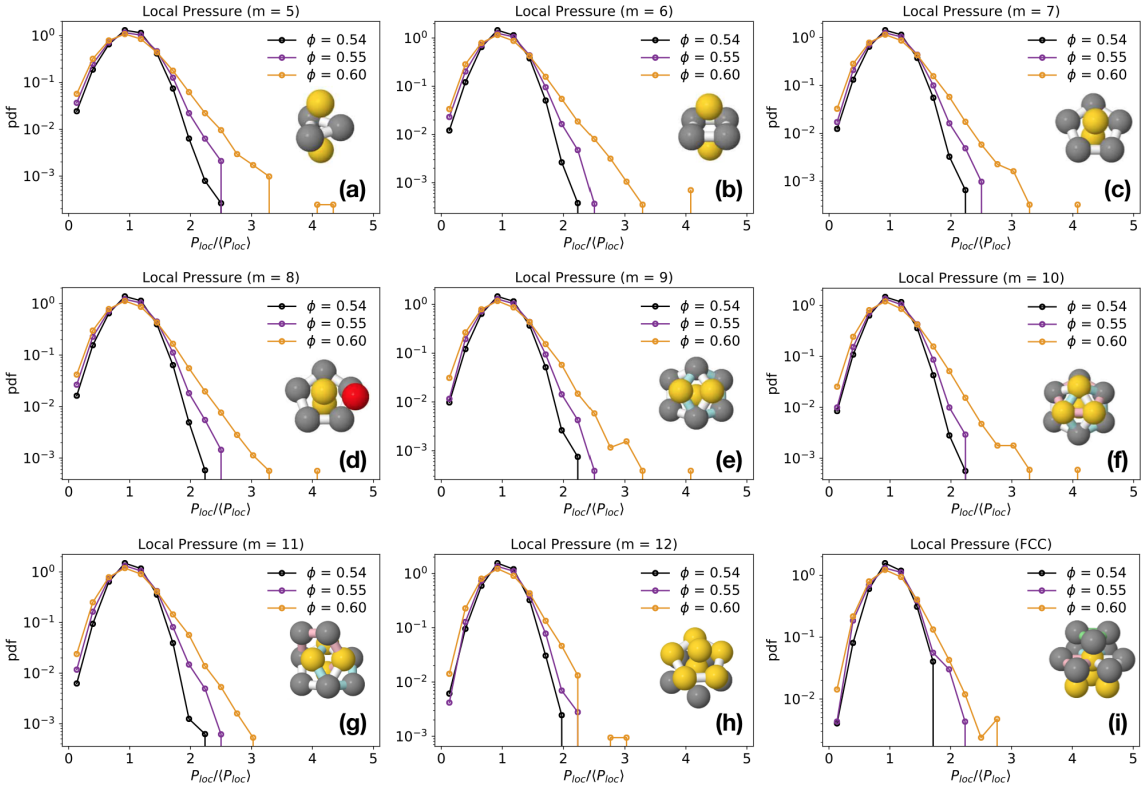

Fig. 7.13 Local pressure distributions of particles in TCC cluster with number of particles (a) $m = 5$, (b) $m = 6$, (c) $m = 7$, (d) $m = 8$, (e) $m = 9$, (f) $m = 10$, (g) $m = 11$, (h) $m = 12$ and (i) FCC cluster.

TCC in force chains

We compare the fractions of clusters in the whole emulsion N_C^{all}/N^{all} and only in particles that participate in force chains N_C^{Chain}/N^{Chain} (hatch markers) in Fig. 7.14. From the bar plot, we can observe only a subtle increase for most of clusters in all emulsions. From figures of R_{Chain} against each cluster species in Fig. 7.14 (left), we can see the increase of large clusters such as $m = 12$ and FCC is more pronounced in emulsions with volume fraction of $\phi = 0.54$ and 0.60. By comparison in the emulsion with volume fraction $\phi = 0.55$, there is only slight change for all species of clusters. All these figures indicate that TCC local structures play an limited role in force chains and stress transmissions in these three dense emulsions.

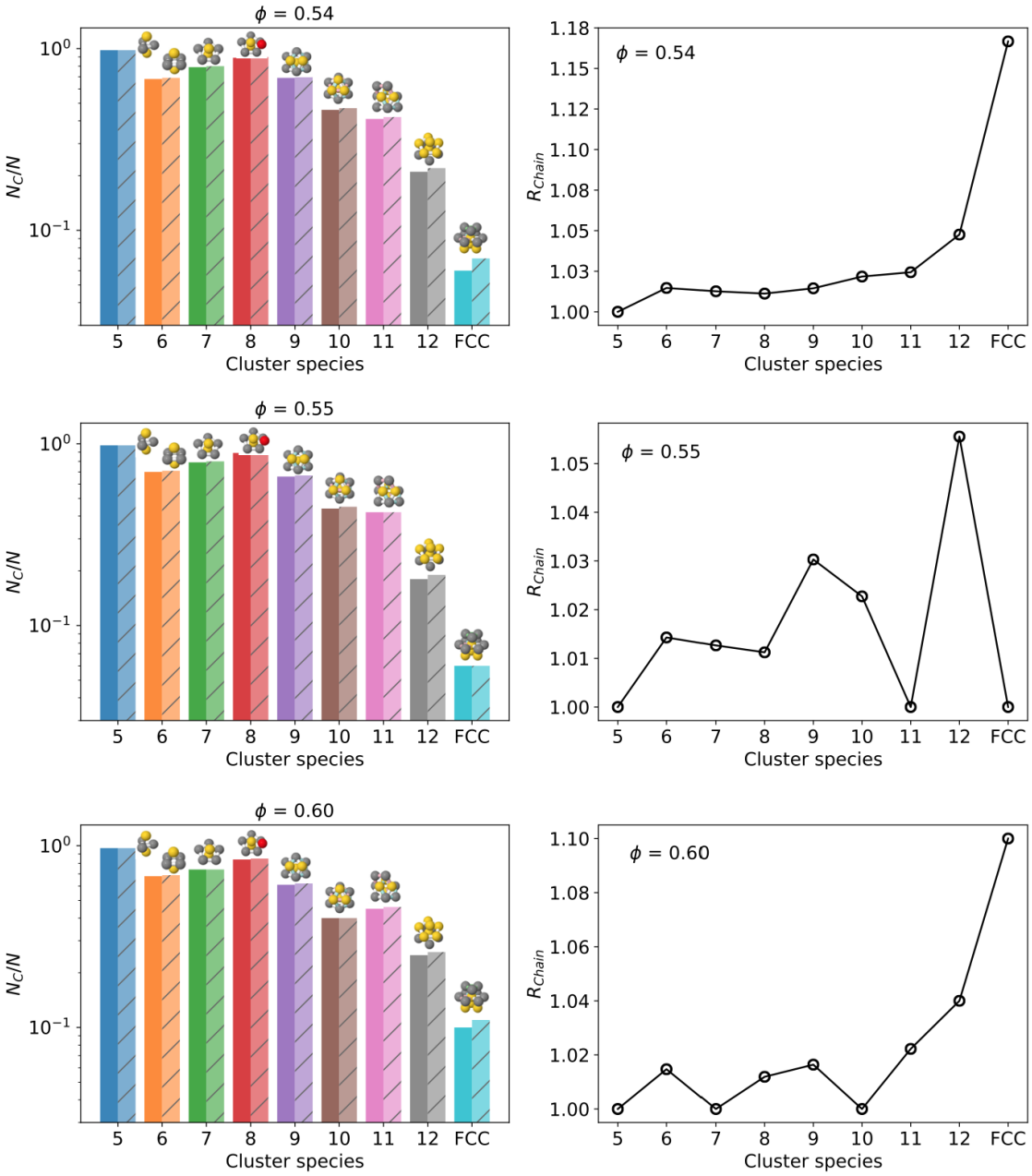

Fig. 7.14 Comparison of TCC cluster populations in all particles and only particles forming force chains. (Left) Bar plot of populations of TCC clusters with particles participating force chains or not. Bars with hatched markers are particles forming force chains. (Right) Plot of R_{Chain} against different species of local structures with number of particles $m = 5$ to 12 and TCC structure.

7.4 Summary

In this chapter, we prepared three dense emulsions with volume fractions ϕ of 0.54, 0.55 and 0.60, with the aim to identify force-bearing particles and force chains in colloidal glasses

supercooled to different extent. However, we found small crystalline regions in all three dense emulsions while other parts being amorphous. The one with highest volume fraction $\phi = 0.60$ has highest population crystalline structures, HCP is found in this dense sample, while only FCC is found in the other two samples.

The pair correlation function $g(r)$s indicate all these emulsions have high volume fractions. The average number of neighbours $\langle N \rangle$ increases from 11 to 12 whereas the average number of contacts $\langle Z \rangle$ is 9 and is the same for all samples. This number is much higher than the isostatic contact number 6 for mechanical stability. The slight decrease of number of contacts in the emulsion with higher volume fraction is still not clear.

The topological cluster classification results show a very subtle decrease in the population of small clusters (with number of particle $m < 10$) as increasing the emulsion volume fraction. On the contrary, the population of large clusters with $m > 10$ grows slightly, and also more crystalline structures both HCP and FCC are found. The overall populations are much higher than those found in colloidal gels.

The shape of the distribution of contact forces of the emulsion with lower volume fraction $\phi = 0.54$ is more Gaussian-like, as the volume fraction increases, the range of distribution widens, and the shape becomes close to an exponential. This is by no means close to the prediction of a power law scaling of force network when approaching jamming[7].

Force chains stretching over more than 300 particle diameters are detected, the fraction of particles forming force chains is much higher than that in colloidal gels. Distributions of size of force chains decay exponentially for all emulsions, the longest force chain identified is 395 particle diameters in the emulsion with volume fraction of $\phi = 0.55$. However, there is still no percolating force chain observed in any sample, they are not mechanically rigid, which is contradictory to the fact they have number of contacts $\langle Z \rangle$much larger than 6.

The shape of the distribution of local pressure has similar trend of contact force distributions. The local pressure distribution of small clusters has similar shape to that of the bulk emulsion, which means the overall behaviours are dominated by small clusters. This is possibly due to the high population of small clusters. As the size of cluster increases, the distributions of local pressures become more Gaussian-like.

The comparison of the TCC populations in all particles and only in particles participating force chains in dense emulsions shows only very subtle increase when particles are forming force chains. This indicates local structures play limited roles in organising particles into force chains and stress transmissions.

Overall, we did not obtain glassy states near the potential Gardner transition, so that we cannot identify their force networks and realise the goal of testing the existence of Gardner transition experimentally. However we have achieved the first experimental work on resolving

interparticle contact forces and networks in dense thermal systems. The experiment can be improved by introducing polydispersity to the system to form purely amorphous states, and produce more samples in the range between the glass and jamming transition. Smaller droplets are desired so that we can also study the dynamics of these glassy states.

Chapter 8

Conclusions

The aim of this thesis has been experimentally measuring contact forces and stress fields in thermal systems which are the microscopic origins of mechanical properties of soft materials, and relate forces with structural properties such as the local packing.

First we demonstrate methods of producing monodisperse oil-in-water colloidal droplets by using microfluidic devices. In chapter 3, we are able to obtain colloidal droplets by reducing the channel size to the value that is comparable to the desired droplet size, the size of junction we employed is from 3 to 8 μm. In chapter 4 we take a different approach. We use a novel opposed-flow geometry, a jet as thin as a micron is formed in a 50 μm channel due to flow focusing, this thin jet further breaks up into sub-micron oil droplets in the outlet channel.

In the next three chapters 5 - 7, colloidal gels and glasses are prepared using the monodisperse colloidal emulsions. We show results of local structure and contact force measurements in colloidal gels with various attraction strength, one colloidal gel creaming under gravity, and dense emulsions with three different volume fractions.

8.1 Colloidal droplet generation using microfluidic devices

The application of NOA microfluidic devices provides robust hydrophilic surfaces, and avoids problematic surface coating for channels with a few micrometers. This enables us to generate monodisperse silicone oil in water colloidal droplets. Droplet size is influenced by the viscosity ratio and flow rate ratio of the two phases. We are also able to collect a decent amount droplets to study the local structural behaviours of dense emulsions.

By tuning close to a second order (continuous) transition in an opposed-flow geometry PDMS microfluidic device, we can reduce the droplet size by almost an order of magnitude compared with the dimension of the device. With the jet radius following power-law scaling,

tunable continuously, we are able to produce monodisperse droplets down to sub-micron levels.

In agreement with previous results, we find that the smallest jet size is limited by transition to a dripping state. In the opposed flow geometry, on the other hand, dripping is suppressed, and the smallest jet size of about 1 μm appears to be limited only by our ability to adjust parameters close to a second order transition.

Of primary interest would be a thorough investigation of the effect of angle on the droplet generation behaviour, as well investigating whether the same effect is suitable for the production of bubbles, a useful system with many biomedicine applications [1].

8.2 Contact forces and local structures in thermal systems

Combining the super-resolution microscopy (STED) with a solvatochromic dye (Nile Red), we are able to visualise interdroplet contact area in real space at individual particle level in colloidal systems. These contacts are proportional to interdroplet forces according to the Princen force model[2]. By tracking the coordinates and sizes of both droplets and contacts, we can calculate contact forces, and further we can find the distributions of contact forcs, stress field for each individual particle, force chains and relate all these properties with their local structures determined by the algorithm of topological cluster classification (TCC).

8.2.1 Colloidal gels

In chapter 5 we examine structures and contact forces for three colloid-polymer mixtures with various attraction strength. This is realised by changing non-absorbing polymer concentrations, the volume fraction of polymers ϕ_p are 0.8, 1.2 and 2.0 respectively. All colloid-polymer mixtures are all quenched below the gelation temperature.

We find the magnitude of the average force for three gels is the same, around 5 nN. The force distribution scaled by the average force $P(f/\langle f\rangle)$ peaks at a value around $1.5\langle f\rangle$ and then decays following a Gaussian distribution. This different from an exponential decay at large forces, which is typically found in jammed granular matter[3, 4]. The shape of the scaled distribution is not significantly varied among the change of polymer concentrations. It only becomes broader at the highest polymer concentration, indicating a subtle increase in the heterogeneity of force distribution. There is no difference identified for the distributions of the most compressive stress and stress trace of the three colloidal gels. They are unimodal and decay exponentially, they also have a wider range compared with that of the force distribution.

The subtle difference in force and stress distributions originate from their similar structural properties. We found the pair correlation function $g(r)$ of the three state points are almost identical, but both the coordination number N and contact number Z decrease slightly with increasing polymer concentrations. This also leads to a decrease in the number of local structures identified.

We do not find percolated force chains in any of the colloidal gel, the longest chain stretch over 26 particle diameters. The distribution of lengths of force chains also decays exponentially. For a elastic material we would expect there is percolated force chains so that stress can transmit through the material and support some stresses. However, the contact forces we measured in this thesis are only compressive forces (the repulsion part of the interaction potential), particles under tension are not considered. Identifying a percolated force chain only with compressive forces in colloidal gels appears impractical.

Finally we investigated the correlation between local structures and stresses. We found the stress distribution in each species of local structure decays slower as the size of cluster increases, meaning that large clusters are carrying relatively large stresses. The percentage of number of clusters identified in force chains is also higher than the fraction in the whole system, showing that local structures play an import role in stress transmission.

8.2.2 Gel settling under gravity

The colloidal gel with polymer volume fraction $\phi_p = 0.8$ is observed for much longer time in order to investigate the evolutions of structures and forces of gel settling under gravity. Surprisingly, although the gel travels all the way crossing the sample height to the top in about $320\tau_B$, there is no significant change of either structures and force distributions.

A subtle increase is found in the peak in the distribution number of neighbours $P(N)$, this might be due to the increase of local particle volume fraction when the gel only occupies the top part of the sample cell. However, the other structural properties like pair correlation function $g(r)$, number of contacts Z, and TCC local structures remain almost identical for all time frames. The consistent gel structures confirm the settling behaviour we observed is more likely to be a creeping sedimentation rather than gel collapse.

The distributions of contact forces are fitted with Gaussian distributions, while the distribution of local pressure decays exponentially. Except for the outlier of time frame t_1, the distributions of contact forces broaden as gel creams further, the peak also becomes less pronounced. In the simulation study by O'Hern *et al*, they showed that the emergence of the peak in the contact force distribution indicates the development of solidity and a yield stress in the system[4]. It is conveniently to infer that the disappearing in turn indicates the loss of solidity and the system returns to liquid-like, and this is similar to what we find at the end

of gel creaming. It would be interesting to check the force distribution at even longer time frame, when the gel structure completely disappeared, becomes a dense colloidal liquid.

8.2.3 Dense emulsions

In chapter 7, three dense emulsions with volume fractions ϕ of 0.54, 0.55 and 0.60 were investigated, with the aim to identify force-bearing particles and force chains in colloidal glasses supercooled to different extent. However, we found small crystalline regions in all three dense emulsions while other parts being amorphous. The one with highest volume fraction $\phi = 0.60$ has highest population crystalline structures, HCP is found in this dense sample, while only FCC is found in the other two samples.

The topological cluster classification results show a very subtle decrease in the population of small clusters (with number of particle $m < 10$) as increasing the emulsion volume fraction. On the contrary, the population of large clusters with $m > 10$ grows slightly, and also more crystalline structures both HCP and FCC are found. The overall populations are much higher than those found in colloidal gels.

The shape of the distribution of contact forces of the emulsion with lower volume fraction $\phi = 0.54$ is more Gaussian-like. As the volume fraction increases, the range of distribution widens, and the shape becomes close to an exponential, similar to experimental measurements of contact forces using photoelastic disks[5, 6]. But this is by no means close to the prediction of a power law scaling of force network when approaching jamming as described in the theoretical work[7].

Force chains in dense emulsions are much bigger than those in colloidal gels. Distributions of size of force chains decay exponentially for all emulsions, the longest force chain identified is 395 particle diameters in the emulsion with volume fraction of $\phi = 0.55$. However, there is still no percolating force chain observed in any sample, they are not mechanically rigid, which is contradictory to the fact they have number of contacts $\langle Z \rangle = 9$ which is much larger than 6.

The shape of the distribution of local pressure has similar trend of contact force distributions. The local pressure distribution of small clusters has similar shape to that of the bulk emulsion, which means the overall behaviours are dominated by small clusters. This is possibly due to the high population of small clusters. As the size of cluster increases, the distributions of local pressures become more Gaussian-like.

The comparison of the TCC populations in all particles and only in particles participating force chains in dense emulsions shows only very subtle increase when particles are forming force chains. This indicates local structures play limited roles in organising particles into force chains and stress transmissions.

Overall, we fail to obtain glassy states near the potential Gardner transition, so that we cannot identify their force networks and realise the goal of testing the existence of Gardner transition experimentally. However we have achieved the first experimental work on resolving interparticle contact forces and networks in dense thermal systems. This presents the possibility to experimental investigate the Gardner transition with precisely quenched colloidal glasses.

8.3 Further work

The results of interdroplet force measurements presented in this thesis are based on assumption that the fluorescent dye intensity increases as two droplets are in contact, the size of the high intensity area represents contact area and then determines the magnitude of the contact force. So far, however, there is still no experimental work that can prove the validity of this method. Therefore, a comparison with other force measurement approaches will be useful in order to give evidence of the reliability of the fluorescence method, and also provides some work frames to quantify the sensitivity of our method.

Optical tweezers are optical micromanipulators that use a highly focused laser beam to optically trap dielectric particles. They have been widely used to probe microscopic forces for various systems, *e.g.* colloidal suspensions or emulsions[168–170]. In the force measurement of a pair of droplets A and B, droplet A is always fixed by the optical trap during the measurements, at the beginning the other droplet B is trapped at a distance that is not too far away from the stationary droplet A. Droplet B is then stepped toward droplet A until droplet A is displaced from the centre of the trap. When droplet B is retracted back, droplet A will come back to its original optically trapped position. During this movement cycle, the positions of both droplet are recorded for each time frame. The interdroplet force between these two droplets can be calculated using Hooke's law, $F = kx$, where k is the trap strength and x is the droplet displacement. The trap strength is determined by observing the variance of the Brownian fluctuations of the trapped droplet over a certain time period, $k = k_B T / < \Delta^2 >$, where $k_B T$ is thermal energy, $< \Delta^2 >$ is the variance of Brownian fluctuations. A force-separation curve is then calculated for a given pair of droplets. In each emulsion with different salt concentration, the force-separation curves can be fit with DLVO theory, which describes the force between charged surfaces[170]. The well fitted force-separation curves demonstrate that the measurement of interdroplet forces by using optical tweezers is plausible. Therefore, performing an force measurement experiment with optical tweezers on a pair of droplets in our system is beneficial for our study and can be considered as a calibration for our force analysis.

In this thesis, we do not observe gel collapse which is often relevant for formulation industrial applications. The settling experiment can be improved by increasing the size of sample cell, so that a minimum sample height is satisfied for gels to collapse. During collapse, gel structure will change markedly and thus provides the opportunity for diverse scenarios of force distributions and transmissions. After the delay time, collapse happens rapidly, thus a shorter time interval for 3D confocal stack images is required in order to be able to capture all structural and microscopic force changes during the rapid collapse. Smaller particles or solvent with better density matching property will reduce the creaming rate, thus are useful for studying gel collapse.

Another interesting piece of work is to shear colloidal gels. The application of an external shear force is anisotropic which is intrinsically different from gravity. The magnitude and frequency are easily adjusted by controlling shear cells. Investigating the response of colloidal gels to external shear forces with regard to structures and microscopic contact forces is intriguing and fundamental to explore mechanical properties of gels.

As for the colloidal glass experiment, it can be improved by introducing polydispersity to the system to form purely amorphous states, and produce more samples in the range between the glass and jamming transition. Smaller droplets are desired so that we can also study the dynamics of these glassy states.

References

[1] Kanaka Hettiarachchi and Abraham P. Lee. Polymer-lipid microbubbles for biosensing and the formation of porous structures. *Journal of Colloid and Interface Science*, 344(2):521–527, 2010.

[2] H M Princen. Rheology of foams and highly concentrated emulsions I. Elastic properties and yield stress of a cylindrical model system. *Journal of Colloid and Interface Science*, 91(1):160–175, 1983.

[3] Jasna Brujic, Sam F Edwards, Dmitri V Grinev, Ian Hopkinson, Djordje Brujic, and Hernán a Makse. 3D bulk measurements of the force distribution in a compressed emulsion system. *Faraday discussions*, 123(3):207–220, 2003.

[4] Corey S. O'Hern, Stephen A. Langer, Andrea J. Liu, and Sidney R. Nagel. Force distributions near jamming and glass transitions. *Physical Review Letters*, 86(1):111–114, 2001.

[5] Jie Zhang, T. S. Majmudar, M. Sperl, and R. P. Behringer. Jamming for a 2D granular material. *Soft Matter*, 6(13):2982–2991, 2010.

[6] K. W. Desmond, P. J. Young, D. Chen, and E. R. Weeks. Experimental study of forces between quasi-two-dimensional emulsion droplets near jamming. *Soft Matter*, 9(12):3424–3436, 2013.

[7] Patrick Charbonneau, Jorge Kurchan, Giorgio Parisi, Pierfrancesco Urbani, and Francesco Zamponi. Fractal free energy landscapes in structural glasses. *Nature Communications*, 5:1–6, 2014.

[8] Gary L. Hunter and Eric R. Weeks. The physics of the colloidal glass transition. *Reports on Progress in Physics*, 75(6):1–30, 2012.

[9] Richard A. L. Jones. *Soft Condensed Matter*. Oxford Univesity Press, 2002.

[10] C. P. Royall, W. C. K. Poon, and E. R. Weeks. In search of colloidal hard spheres. *Soft Matter*, 9(1):17–27, 2013.

[11] Clifford P. Brangwynne, Christian R. Eckmann, David S. Courson, Agata Rybarska, Carsten Hoege, Jöbin Gharakhani, Frank Jülicher, and Anthony A. Hyman. Germline P granules are liquid droplets that localize by controlled dissolution/condensation. *Science*, 324(5935):1729–1732, 2009.

[12] Yongdae Shin and Clifford P. Brangwynne. Liquid phase condensation in cell physiology and disease. *Science*, 357(6357), 2017.

[13] J D Bernal. The Bakerian Lecture, 1962 The structure of liquids. *Proceedings of the Royal Society of London. Series A. Mathematical and Physical Sciences*, 280(1382):299–322, 1964.

[14] P. N. Pusey and W. van Megen. Phase behaviour of concentrated suspensions of nearly colloidal spheres. *Nature*, 320(27):340–342, 1986.

[15] C. A Angell. Structural Instability and Relaxation in Liquid and Glassy Phases Near The Fragile Liquid Limit. *Journal of Non-Crystalline Solids*, 102(1-3):205–221, 1988.

[16] C. Patrick Royall and Stephen R. Williams. The role of local structure in dynamical arrest. *Physics Reports*, 560:1–75, 2015.

[17] Gerold Adam and Julian H. Gibbs. On the temperature dependence of cooperative relaxation properties in glass-forming liquids. *The Journal of Chemical Physics*, 43(1):139–146, 1965.

[18] Martin Goldstein. Viscous liquids and the glass transition: A potential energy barrier picture. *The Journal of Chemical Physics*, 51(9):3728–3739, 1969.

[19] T. R Kirkpatrick and D. Thirumalai. Scaling concepts for the dynamics of viscous liquids near an ideal glassy state. *Physical Review A*, 40(2):1045–1054, 1989.

[20] Daniel Kivelson, Steven A. Kivelson, Xiaolin Zhao, Zohar Nussinov, and Gilles Tarjus. A thermodynamic theory of supercooled liquids. *Physica A: Statistical Mechanics and its Applications*, 219(1-2):27–38, 1995.

[21] G. Tarjus, S. A. Kivelson, Z. Nussinov, and P. Viot. The frustration-based approach of supercooled liquids and the glass transition: A review and critical assessment. *Journal of Physics Condensed Matter*, 17(50), 2005.

[22] David Chandler and Juan P. Garrahan. Dynamics on the Way to Forming Glass: Bubbles in Space-Time. *Annual Review of Physical Chemistry*, 61(1):191–217, 2010.

[23] Emanuela Zaccarelli. Colloidal gels: equilibrium and non-equilibrium routes. *Journal of Physics: Condensed Matter*, 19(32):323101, 2007.

[24] Paul J. Flory. Molecular Size Distribution in Three Dimensional Polymers. I. Gelation. *Journal of the American Chemical Society*, 63(11):3083–3090, 1941.

[25] Sho Asakura and Fumio Oosawa. On interaction between two bodies immersed in a solution of macromolecules. *The Journal of Chemical Physics*, 22(7):1255–1256, 1954.

[26] B Widom. Some Topics in the Theory of Fluids. 39(2808), 1963.

[27] Alexei Ivlev, Hartmut Löwen, Gregor Morfill, and C. Patrick Royall. *Complex Plasmas and Colloidal Dispersions: Particle-resolved Studies of Classical Liquids and Solids*. World Scientific Publishing Co., Singapore Scientific, 2012.

[28] Wilson C K Poon, Angus D Pirie, and Peter N Pusey. Gelation in Colloid-Polymer Mixtures. *Faraday Discuss*, 101(1):65–76, 1995.

[29] A. V. Vrij. Polymers At Interfaces And The Interactions in Colloidal Dispersions. *Pure and Applied Chemistry*, 48(4):471–483, 1976.

[30] Hendrik N W Lekkerkerker, W C K Poon, Peter N Pusey, A Stroobants, and P B Warren. Phase-Behavior of Colloid Plus Polymer Mixtures. *Europhysics Letters*, 20(6):559–564, 1992.

[31] M H J Hagen, E J Meijer, G. C. A. M Mooij, D Frenkel, and H. N. W Lekkerkerker. Does C60 have a liquid phase ? Enhanced reactivity of fullerene cations containing adjacent pentagons. 365(September):425–426, 1993.

[32] L. A. Girifalco. Molecular properties of fullerene in the gas and solid phases. *The Journal of Physical Chemistry*, 96(2):858–861, 1992.

[33] A. Malins, S. R. Williams, J. Eggers, and C. P. Royall. Identification of structure in condensed matter with the topological cluster classification. *J. Chem. Phys.*, 139(23):234506, 2013.

[34] Jade Taffs and C. Patrick Royall. The role of fivefold symmetry in suppressing crystallization. *Nature Communications*, 7:1–7, 2016.

[35] Nicholas Wood, John Russo, Francesco Turci, and C. Patrick Royall. Coupling of sedimentation and liquid structure: Influence on hard sphere nucleation. *Journal of Chemical Physics*, 149(20), 2018.

[36] Rattachai Pinchaipat, Matteo Campo, Francesco Turci, James E. Hallett, Thomas Speck, and C. Patrick Royall. Experimental Evidence for a Structural-Dynamical Transition in Trajectory Space. *Physical Review Letters*, 119(2):1–5, 2017.

[37] James E. Hallett, Francesco Turci, and C. Patrick Royall. Local structure in deeply supercooled liquids exhibits growing lengthscales and dynamical correlations. *Nature Communications*, 9(1), 2018.

[38] Tharwat F. Tadros. *Emulsion Formation and Stability*. John Wiley & Sons, Ltd, 2013.

[39] J. Bibette. Depletion interactions and fractionated crystallization for polydisperse emulsion purification. *Journal of Colloid and Interface Science*, 147(2):474–478, 1991.

[40] Ashleigh B Theberge, Fabienne Courtois, Yolanda Schaerli, Martin Fischlechner, Chris Abell, Florian Hollfelder, and Wilhelm TS Huck. Microdroplets in microfluidics: an evolving platform for discoveries in chemistry and biology. *Angew. Chem. Int. Ed.*, 49(34):5846–5868, 2010.

[41] C. Martino and Andrew J. deMello. Droplet-based microfluidics for artificial cell generation : a brief review. *Interface Focus*, 6:20160011, 2016.

[42] David J Beebe, Glennys A Mensing, and Glenn M Walker. Physics and applications of microfluidics in biology. *Annu. Rev. Biomed. Eng.*, 4:261–286, 2002.

[43] Mira T. Guo, Assaf Rotem, John A. Heyman, and David A. Weitz. Droplet microfluidics for high-throughput biological assays. *Lab Chip*, 12(12):2146, 2012.

[44] Changqing Yi, Cheuk Wing Li, Shenglin Ji, and Mengsu Yang. Microfluidics technology for manipulation and analysis of biological cells. *Anal. Chim. Acta*, 560(1-2):1–23, 2006.

[45] Emmanuel Delamarche, David Juncker, and Heinz Schmid. Microfluidics for processing surfaces and miniaturizing biological assays. *Adv. Mater.*, 17(24):2911–2933, 2005.

[46] Max Meissner, Jun Dong, Jens Eggers, Annela M. Seddon, and C. Patrick Royall. Oil-in-water microfluidics on the colloidal scale: new routes to self-assembly and glassy packings. *Soft Matter*, 13:788–794, 2017.

[47] Nicolas Champagne, Romain Vasseur, Adrien Montourcy, and Denis Bartolo. Traffic jams and intermittent flows in microfluidic networks. *Phys. Rev. Lett.*, 105(4):044502, 2010.

[48] Todd M Squires and Stephen R Quake. Microfluidics: Fluid physics at the nanoliter scale. *Reviews of modern physics*, 77(3):977, 2005.

[49] A. M. Gañán-Calvo and J. M. Gordillo. Perfectly monodisperse microbubbling by capillary flow focusing. *Phys. Rev. Lett.*, 87(27 Pt 1):274501, 2001.

[50] S. L. Anna, N. Bontoux, and H. A. Stone. Formation of dispersions using "flow focusing" in microchannels. *Appl. Phys. Lett.*, 82(3):364–366, 2003.

[51] Todd Thorsen, Richard W. Roberts, Frances H. Arnold, and Stephen R. Quake. Dynamic pattern formation in a vesicle-generating microfluidic device. *Physical Review Letters*, 86(18):4163–4166, 2001.

[52] J K Nunes, S S H Tsai, J Wan, and H A Stone. Dripping and jetting in microfluidic multiphase flows applied to particle. *J. Phys. D: Appl. Phys.*, 46(114002):1–20, 2013.

[53] P. Garstecki, H. A. Stone, and G. M. Whitesides. Mechanism for Flow-Rate Controlled Breakup in Confined Geometries: A Route to Monodisperse Emulsions. *Phys. Rev. Lett.*, 94(16):164501, 2005.

[54] Zhihong Nie, MinsSeok Seo, Shengqing Xu, Patrick C Lewis, Michelle Mok, Eugenia Kumacheva, George M Whitesides, Piotr Garstecki, and Howard A Stone. Emulsification in a microfluidic flow-focusing device : effect of the viscosities of the liquids. *Microfluid Nanofluid*, 5:585–594, 2008.

[55] Andrew S Utada, Alberto Fernandez-Nieves, Howard A Stone, and David A Weitz. Dripping to jetting transitions in coflowing liquid streams. *Phys. Rev. Lett.*, 99(9):094502, 2007.

[56] DR Link, Shelley L Anna, DA Weitz, and HA Stone. Geometrically mediated breakup of drops in microfluidic devices. *Phys. Rev. Lett.*, 92(5):054503, 2004.

[57] Takasi Nisisako, Toru Torii, and Toshiro Higuchi. Droplet formation in a microchannel network. *Lab Chip*, 2(1):24–26, 2002.

[58] Takasi Nisisako, Shingo Okushima, and Toru Torii. Controlled formulation of monodisperse double emulsions in a multiple-phase microfluidic system. *Soft Matter*, 1(1):23–27, 2005.

[59] Martin F Haase and Jasna Brujic. Tailoring of high-order multiple emulsions by the liquid–liquid phase separation of ternary mixtures. *Angew. Chem. Int. Ed.*, 53(44):11793–11797, 2014.

[60] Céline Cohen, R. Giles, V. Sergeyeva, N. Mittal, P. Tabeling, D. Zerrouki, J. Baudry, J. Bibette, and N. Bremond. Parallelised production of fine and calibrated emulsions by coupling flow-focusing technique and partial wetting phenomenon. *Microfluid Nanofluidics*, 17:959–966, 2014.

[61] David Bardin, Thomas D Martz, Paul S Sheeran, Roger Shih, A Dayton, and Abraham P Lee. High-speed, clinical-scale microfluidic generation fo stable phase-change droplets for gas embolotherapy. *Lab on a chip*, 11:3990–3998, 2011.

[62] W. A. C. Bauer, J. Kotar, P. Cicuta, R. T. Woodward, J. V. M. Weaver, and W. T. S. Huck. Microfluidic production of monodisperse functional o/w droplets and study of their reversible pH dependent aggregation behavior. *Soft Matter*, 7(9):4214–4220, 2011.

[63] Jerry M Chen, Ming-che Kuo, and Chien-po Liu. Control of Droplet Generation in Flow-Focusing Microfluidic Device with a Converging-Diverging Nozzle-Shaped Section. *Japanese Journal of Applied Physics*, 50:107301, 2011.

[64] A. J. Acero, N. Rebollo-Muñoz, J. M. Montanero, A. M. Gañán-Calvo, and E. J. Vega. A new flow focusing technique to produce very thin jets. *Journal of Micromechanics and Microengineering*, 23(6), 2013.

[65] Woong Chan Jeong, Jong Min Lim, Jae Hoon Choi, Jong Hoon Kim, You Jin Lee, Seung Hyun Kim, Gaehang Lee, Jong Duk Kim, Gi Ra Yi, and Seung Man Yang. Controlled generation of submicron emulsion droplets via highly stable tip-streaming mode in microfluidic devices. *Lab Chip*, 12(8):1446–1453, 2012.

[66] Lingling Shui, Albert Van Den Berg, and Jan C T Eijkel. Scalable attoliter monodisperse droplet formation using multiphase nano-microfluidics. *Microfluid Nanofluid*, 11:87–92, 2011.

[67] Alfonso M. Gañán-Calvo, Román González-Prieto, Pascual Riesco-Chueca, Miguel A. Herrada, and María Flores-Mosquera. Focusing capillary jets close to the continuum limit. *Nat. Phys.*, 3(10):737–742, 2007.

[68] Yung Chieh Tan and Abraham Phillip Lee. Microfluidic separation of satellite droplets as the basis of a monodispersed micron and submicron emulsification system. *Lab on a Chip*, 5(10):1178–1183, 2005.

[69] Timothy Mark Obey and Brian Vincent. Novel Monodisperse "Silicone Oil" /Water Emulsions. *Journal of Colloid and Interface Science*, 163:454–463, 1994.

[70] W E R N E R Stober and Arthur Fink. Controlled Growth of Monodisperse Silica Spheres in the Micron Size Range. *Journal of Colloid and Interface Science*, 26:62–69, 1968.

[71] Syed Waqar Hussain Shah, Bushra Naseem, Wajid Rehman, Nadia Bashir, and Syed Sakhawat Shah. Investigation of 1-alkanols in organised solutions. *Bulletin of the Chemical Society of Ethiopia*, 25(3):469–474, 2011.

[72] Hiroshi Yoshida, Kensaku Ito, and Norio Ise. Localized ordered structure in polymer latex suspensions as studied by a confocal laser scanning microscope. *Physical Review B*, 44(1):435–438, 1991.

[73] Stefan W. Hell and Jan Wichmann. Breaking the diffraction resolution limit by stimulated emission: stimulated-emission-depletion fluorescence microscopy. *Optics Letters*, 19(11):780, 1994.

[74] Stefan W Hell. Far-Field Optical Nanoscopy. *Science*, 316(5828):1153–1158, 2007.

[75] Chantal Esther C.E Carpentier. *Three-dimensional visualization Three-dimensional visualization of contact of contact networks in granular material*. PhD thesis, University of Amsterdam, 2013.

[76] Jasna Brujic. *Experimental Study of Stress Transmission Through Particulate Matter*. Phd, Cambridge University, 2004.

[77] Richard Plenderleith, Thomas Swift, and Stephen Rimmer. Highly-branched poly(N-isopropyl acrylamide)s with core–shell morphology below the lower critical solution temperature. *RSC Adv.*, 4(92):50932–50937, 2014.

[78] J Zhou. Measurement of Forces Inside a Three-Dimensional Pile of Frictionless Droplets. *Science*, 1631(2006):1631–1634, 2006.

[79] Tomislav Suhina, Bart Weber, Chantal E. Carpentier, Kinga Lorincz, Peter Schall, Daniel Bonn, and Albert M. Brouwer. Fluorescence microscopy visualization of contacts between objects. *Angewandte Chemie - International Edition*, 54(12):3688–3691, 2015.

[80] Jissy Jose, Alfons Van Blaaderen, and Arnout Imhof. Random three-dimensional jammed packings of elastic shells acting as force sensors. *Physical Review E*, 93(6):1–14, 2016.

[81] M. Leocmach and H. Tanaka. A novel particle tracking method with individual particle size measurement and its application to ordering in glassy hard sphere colloids. *Soft Matter*, 9(5):1447–1457, 2013.

[82] John. C Crocker and David. G Grier. Methods of Digital Video Microscopy for Colloidal Studies. *Journal of Colloid and Interface Science*, 310(179):298–310, 1996.

[83] John Forrester, Richard Greaves, Howard Noble, and Richard Taylor. Modeling Social-Ecological Problems in. 19(6):73–82, 2014.

[84] Nobuyuki Otsu. A Threshold Selection Method from Gray-Level Histograms. *IEEE TRANSACTIONS ON SYSTEMS*, 9(1):62–66, 1979.

[85] J. F. Peters, M. Muthuswamy, J. Wibowo, and A. Tordesillas. Characterization of force chains in granular material. *Physical Review E - Statistical, Nonlinear, and Soft Matter Physics*, 72(4):1–8, 2005.

[86] R. J. Hunter. *Foundations of colloid science.* Oxford University Press, 2001.

[87] A. J. Liu and S. R. Nagel. The jamming transition and the marginally jammed solid. *Annu. Rev. Cond. Matt. Phys.*, 1:347–369, 2010.

[88] T. G. Mason, J. Bibette, and D. A. Weitz. Elasticity of compressed emulsions. *Phys. Rev. Lett.*, 75(10):2051–2054, 1995.

[89] L. Feng, L.-L.a Pontani, R. Dreyfus, P. Chaikin, and J. Brujic. Specificity, flexibility and valence of DNA bonds guide emulsion architecture. *Soft Matter*, 9(41):9816, 2013.

[90] S. J. Van Der Meulen and M. E. Leunissen. Solid colloids with surface-mobile DNA linkers. *J. Am. Chem. Soc.*, 135(40):15129–15134, 2013.

[91] C. Zhang, C. B. O'Donovan, E. I. Corwin, F. Cardinaux, T. G. Mason, M. E. Mabius, and F. Scheffold. Structure of marginally jammed polydisperse packings of frictionless spheres. *Phys. Rev. E*, 91(3):1–6, 2015.

[92] C. Wibowo and K. M. Ng. Product-oriented process synthesis and development: Creams and pastes. *AIChE Journal*, 47(12):2746–2767, 2001.

[93] J. Ubbink. Soft matter approaches to structured foods: from "cook-and-look" to rational food design? *Faraday Disc.*, 158:9, 2012.

[94] J. Eastoe, M. H. Hatzopoulos, and R. Tabor. Microemulsions. In *Encyclopedia of Colloid and Interface Science*, pages 688–729. Springer Berlin Heidelberg, 2013.

[95] H. A. Stone and S. Kim. Microfluidics: basic issues, applications, and challenges. *AIChE Journal*, 47(6):1250–1254, 2001.

[96] A. Wysocki, C. P. Royall, R. G. Winkler, G. Gompper, H. Tanaka, A. Van Blaaderen, and H. Löwen. Direct observation of hydrodynamic instabilities in driven non-uniform colloidal dispersions. *Soft Matter*, 5(7):4, 2008.

[97] A. M. Gañán-Calvo and J. M. Gordillo. Perfectly monodisperse microbubbling by capillary flow focusing. *Phys. Rev. Lett.*, 87(27 Pt 1):274501, 2001.

[98] J. C. McDonald and G. M. Whitesides. Poly (dimethylsiloxane) as a Material for Fabricating Microfluidic Devices. *Acc. Chem. Res*, 35(7):491–499, 2002.

[99] H. Makamba, J. H. Kim, K. Lim, N. Park, and J. H. Hahn. Surface modification of poly(dimethylsiloxane) microchannels. *Electrophoresis*, 24(21):3607–3619, 2003.

[100] D. Bodas and C. Khan-Malek. Hydrophilization and hydrophobic recovery of PDMS by oxygen plasma and chemical treatment—An SEM investigation. *Sensors and Actuators B: Chemical*, 123(1):368–373, 2007.

[101] Wolfgang-Andreas C Bauer, Martin Fischlechner, Chris Abell, and Wilhelm T S Huck. Hydrophilic PDMS microchannels for high-throughput formation of oil-in-water microdroplets and water-in-oil-in-water double emulsions. *Lab on a chip*, 10(14):1814–1819, 2010.

[102] Ph. Wägli, A. Homsy, and N.F. de Rooij. Norland optical adhesive (NOA81) microchannels with adjustable wetting behavior and high chemical resistance against a range of mid-infrared-transparent organic solvents. *Sensors and Actuators B: Chemical*, 156(2):994–1001, 2011.

[103] S. H. Kim, Y. Yang, M. Kim, S.-W. Nam, K.-M. Lee, N. Y. Lee, Y. S. Kim, and S. Park. Simple Route to Hydrophilic Microfluidic Chip Fabrication Using an Ultraviolet (UV)-Cured Polymer. *Adv. Funct. Mater.*, 17(17):3493–3498, 2007.

[104] D. Bartolo, G. Degré, P. Nghe, and V. Studer. Microfluidic stickers. *Lab on a Chip*, 8(2):274–279, 2008.

[105] Rattachai Pinchaipat. No Titl. Technical report, University of Bristol, 2016.

[106] G.I. Taylor. The formation of emulsions in definable fields of flow. *Proceedings of the Royal Society*, 29(Society, The Royal Society, Royal Sciences, Physical):71, 1934.

[107] R. Suryo and O. A. Basaran. Tip streaming from a liquid drop forming from a tube in a co-flowing outer fluid. *Phys. Fluids*, 18:082102, 2006.

[108] A. M. Gañán-Calvo. Unconditional jetting. *Phys. Rev. E*, 78:026304, 2008.

[109] Wendy W. Zhang. Viscous entrainment from a nozzle: Singular liquid spouts. *Physical Review Letters*, 93(18):2–5, 2004.

[110] E Castro-Hernández, F Campo-Cortés, and José Manuel Gordillo. Slender-body theory for the generation of micrometre-sized emulsions through tip streaming. *J. Fluid Mech.*, 698(2012):423–445, 2012.

[111] S. L. Anna. Droplets and bubbles in microfluidic devices. *Ann. Rev. Fluid Mech.*, 48:285–309, 2016.

[112] J. Eggers and E. Villermaux. Physics of liquid jets. *Rep. Progr. Phys.*, 71:036601, 2008.

[113] Itai Cohen and Sidney R Nagel. Scaling at the selective withdrawal transition through a tube suspended above the fluid surface. *Phys. Rev. Lett.*, 88(7):074501, 2002.

[114] Sarah C. Case and Sidney R. Nagel. Spout states in the selective withdrawal of immiscible fluids through a nozzle suspended above a two-fluid interface. *Phys. Rev. Lett.*, 98(11):114501, 2007.

[115] N. Goldenfeld. *Lectures on phase transitions and the renormalization group*. Addison-Wesley, 1993.

[116] S. J. Haward, R. J. Poole, M. A. Alves, P. J. Oliveira, N. Goldenfeld, and A. Q. Shen. Tricritical spiral vortex instability in cross-slot flow. *Phys. Rev. E*, 93:031101, 2016.

[117] A. M. Gañán-Calvo. Enhanced liquid atomization: from flow-focusing to flow-blurring. *Appl. Phys. Lett.*, 86:214101, 2005.

[118] S. L. Anna and H. C. Mayer. Microscale tipstreaming in a microfluidic flow focusing device. *Phys. Fluids*, 18(12):121512, 2006.

[119] J.-M. Chomaz. Global instabilities in spatially developing flows: non-normality and nonlinearity. *Annu. Rev. Fluid Mech.*, 37:357–392, 2005.

[120] A. S. Utada, A. Fernandez-Nieves, J. M. Gordillo, and D. A. Weitz. Absolute instability of a liquid jet in a coflowing stream. *Phys. Rev. Lett.*, 100:014502, 2008.

[121] G. I. Taylor. Conical free surfaces and fluid interfaces. In H. Görtler, editor, *Proceedings of the 11th International Congress of Applied Mathematics, Munich (Germany)*, pages 790–796. Springer, Heidelberg, 1964.

[122] J. D. Buckmaster. Pointed bubbles in slow viscous flow. *J. Fluid Mech.*, 55:385, 1972.

[123] F. Cruz-Mazo, M. A. Herrada, A. M. Gañán-Calvo, and J. M. Montanero. Global stability of axisymmetric flow focusing. *J. Fluid Mech.*, 832:329–344, 2017.

[124] CN Likos, KA Vaynberg, H. Löwen, and NJ Wagner. Colloidal stabilization by adsorbed gelatin. *Langmuir*, 16(9):4100–4108, 2000.

[125] A. Malins, S. R. Williams, J. Eggers, H. Tanaka, and C. P. Royall. Geometric frustration in small colloidal clusters. *J. Phys.: Condens. Matter*, 21:425103, 2009.

[126] Guangnan Meng, Natalie Arkus, Michael P Brenner, and Vinothan N Manoharan. The free-energy landscape of clusters of attractive hard spheres. *Science*, 327(5965):560–563, 2010.

[127] C. L. Klix, K. Murata, H. Tanaka, S. Williams, A. Malins, and C. P. Royall. Novel kinetic trapping in charged colloidal clusters due to self-induced surface charge organization. *Sci. Rep.*, 3:2072, 2013.

[128] C. Carnero Ruiz, L. Díaz-López, and J. Aguiar. Micellization of sodium dodecyl sulfate in glycerol aqueous mixtures. *J. Dispersion Sci. Technol.*, 29:266–273, 2008.

[129] C. P. Royall. Hunting mermaids in real space: Known knowns, known unknowns and unknown unknowns. *submitted*, 2018.

[130] V. Prasad, V. Trappe, A. D. Dinsmore, P. N. Segre, L. Cipelletti, and D. A. Weitz. Universal features of the fluid to solid transition for attractive colloidal particles. *Faraday Discuss.*, 123:1–12, 2003.

[131] S. Manley, H. M. Wyss, K. Miyazaki, J. C. Conrad, V. Trappe, L. J. Kaufman, D. R. Reichman, and D. A. Weitz. Glasslike Arrest in Spinodal Decomposition as a Route to Colloidal Gelation. *Physical Review Letters*, 95(23):238302, 2005.

[132] S. Griffiths, F. Turci, and C. P. Royall. Local structure of percolating gels at very low volume fractions. *J. Chem. Phys.*, 146:014905, 2017.

[133] J. H Irving and John G Kirkwood. The Statistical Mechanical Theory of Transport Processes. IV. The Equations of Hydrodynamics. *J. Chem. Phys.*, 18(817):817–829, 1950.

[134] Dapeng Bi, Jie Zhang, Bulbul Chakraborty, and R. P. Behringer. Jamming by shear. *Nature*, 480(7377):355–358, 2011.

[135] C. h Liu, Sidney R Nagel, D. A Schecter, S. N Coppersmith, S Majumdar, O Narayan, and T. A Witten. Force fluctuations in bead packs. *Science*, 269(5223):513–515, 1995.

[136] T S Majmudar and R P Behringer. Contact force measurements and stress-induced anisotropy in granular materials. *Nature*, 435(7045):1079–1082, 2005.

[137] Andrea J Liu and Sidney R Nagel. Nonlinear dynamics: Jamming is not just cool any more. *Nature*, 396(6706):21–22, 1998.

[138] Nicolas Brodu, Joshua A. Dijksman, and Robert P. Behringer. Spanning the scales of granular materials through microscopic force imaging. *Nature Communications*, 6:1–6, 2015.

[139] Jasna Brujić, Sam F. Edwards, Ian Hopkinson, and Hernán a. Makse. Measuring the distribution of interdroplet forces in a compressed emulsion system. *Physica A: Statistical Mechanics and its Applications*, 327(3):201–212, 2003.

[140] Maxime Clusel, Eric I Corwin, Alexander O N Siemens, and Jasna Brujić. A 'granocentric' model for random packing of jammed emulsions. *Nature*, 460(July):611–615, 2009.

[141] Ivane Jorjadze, Lea-Laetitia Pontani, and Jasna Brujic. Microscopic Approach to the Nonlinear Elasticity of Compressed Emulsions. *Physical Review Letters*, 110(4):048302, 2013.

[142] Isla Zhang, C. Patrick Royall, Malcolm A. Faers, and Paul Bartlett. Phase separation dynamics in colloid–polymer mixtures: the effect of interaction range. *Soft Matter*, 9:2076, 2013.

[143] Peter R. Sperry, Harold B. Hopfenberg, and Noreen L. Thomas. Flocculation of latex by water-soluble polymers: Experimental confirmation of a nonbridging, nonadsorptive, volume-restriction mechanism. *Journal of Colloid And Interface Science*, 82(1):62–76, 1981.

[144] Ferruccio Palazzesi, Matteo Calvaresi, and Francesco Zerbetto. A molecular dynamics investigation of structure and dynamics of SDS and SDBS micelles. *Soft Matter*, 7(19):9148–9156, 2011.

[145] Sugiura-Preparation of monodispersed solid liqid microsphers using microchannel emulsification technique 2000.

[146] Glycerine Producers' Association. *Physcial Properties of Glycerine and Its Solutions*. New York: Glycerine Producers' Association, 1963.

[147] Alexander Stukowski. Visualization and analysis of atomistic simulation data with OVITO-the Open Visualization Tool. *Modelling and Simulation in Materials Science and Engineering*, 18(015012), 2010.

[148] C. Patrick Royall, Ard A. Louis, and Hajime Tanaka. Measuring colloidal interactions with confocal microscopy. *Journal of Chemical Physics*, 127(044507):1–8, 2007.

[149] Jerome K. Percus and George J. Yevick. Analysis of Classical Statistical Mechanics by Means of Collective Coordinates. *Physical Review*, 110(1):1–13, 1958.

[150] Hernán A. Makse, David L. Johnson, and Lawrence M. Schwartz. Packing of compressible granular materials. *Physical Review Letters*, 84(18):4160–4163, 2000.

[151] M. A. Faers and G. R. Kneebone. Application of rheological measurements for probing the sedimentation of suspension concentrate formulations. *Pesticide Science*, 55(3):312–325, 1999.

[152] L. Starrs, W. C.K. Poon, D. J. Hibberd, and M. M. Robins. Collapse of transient gels in colloid-polymer mixtures. *Journal of Physics Condensed Matter*, 14(10):2485–2505, 2002.

[153] Paul Bartlett, Lisa J. Teece, and Malcolm A. Faers. Sudden collapse of a colloidal gel. *Physical Review E*, 85(2):1–13, 2012.

[154] Sara Jabbari-Farouji, Gerard H. Wegdam, and Daniel Bonn. Gels and glasses in a single system: Evidence for an intricate free-energy landscape of glassy materials. *Physical Review Letters*, 99(6):2–5, 2007.

[155] Azaima Razali, Christopher J. Fullerton, Francesco Turci, James E. Hallett, Robert L. Jack, and C. Patrick Royall. Effects of vertical confinement on gelation and sedimentation of colloids. *Soft Matter*, 13(17):3230–3239, 2017.

[156] Lisa J Teece, Malcolm A Faers, and Paul Bartlett. Ageing and collapse in gels with long-range attractions. *Soft Matter*, 7(4):1341–1351, 2011.

[157] R. M.L. Evans and L. Starrs. Emergence of a stress transmission length-scale in transient gels. *Journal of Physics Condensed Matter*, 14(10):2507–2529, 2002.

[158] Lisa J. Teece, James M. Hart, Kerry Yen Ni Hsu, Stephen Gilligan, Malcolm A. Faers, and Paul Bartlett. Gels under stress: The origins of delayed collapse. *Colloids and Surfaces A: Physicochemical and Engineering Aspects*, 458(1):126–133, 2014.

[159] Stefan B. Lindström, Thomas E. Kodger, Joris Sprakel, and David A. Weitz. Structures, stresses, and fluctuations in the delayed failure of colloidal gels. *Soft Matter*, 8(13):3657–3664, 2012.

[160] Shlomo Alexander and Shlomo Alexander. Alexander-Phys-Rep-1998. *Physics Reports*, 296:65–236, 1998.

[161] Ludovic Berthier and Giulio Biroli. Theoretical perspective on the glass transition and amorphous materials. *Reviews of Modern Physics*, 83(2):587–645, 2011.

[162] M. Dinkgreve, M. A. J. Michels, T. G. Mason, and D. Bonn. Crossover between Athermal Jamming and the Thermal Glass Transition of Suspensions. *Physical Review Letters*, 121(22):228001, 2018.

[163] Atsushi Ikeda, Ludovic Berthier, and Peter Sollich. Unified study of glass and jamming rheology in soft particle systems. *Physical Review Letters*, 109(1):018301, 2012.

[164] E. Gardner. Spin glasses with p-spin interactions. *Nuclear Physics, Section B*, 257:747–765, 1985.

[165] R. C. Dennis and E. I. Corwin. The Jamming Energy Landscape is Hierarchical and Ultrametric.

[166] Chen Liu, Ezequiel E. Ferrero, Francesco Puosi, Jean Louis Barrat, and Kirsten Martens. Driving rate dependence of avalanche statistics and shapes at the yielding transition. *Physical Review Letters*, 116(6):1–5, 2016.

[167] Silke Henkes, Carolina Brito, Olivier Dauchot, and Wim Van Saarloos. Local coulomb versus global failure criterion for granular packings. *Soft Matter*, 6(13):2939–2943, 2010.

[168] A. Ashkin, J. M. Dziedzic, J.E. Bjorkholm, and S. Chu. Observation of a single-beam gradient force optical trap for dielectric particles. *Optics Letters*, 11(5):288–290, 1986.

[169] Ulrich F. Keyser, Bernard N. Koeleman, Stijn van Dorp, Diego Krapf, Ralph M. M. Smeets, Serge G. Lemay, Nynke H. Dekker, and Cees Dekker. Direct force measurements on DNA in a solid-state nanopore. *Nature Physics*, 2(7):473–477, 2006.

[170] Marjorie R. Griffiths, Allan Raudsepp, Kathryn M. McGrath, and Martin A. K. Williams. Measuring the interaction between a pair of emulsion droplets using dual-trap optical tweezers. *RSC Advances*, 6(18):14538–14546, 2016.